

**Ph.D. THESIS
UCB/SEMM-94/19**

**STRUCTURAL ENGINEERING, MECHANICS,
AND MATERIALS**

**GENERATION AND INTERACTION OF
COMPRESSIVE STRESS-INDUCED
MICROCRACKS IN CONCRETE**

by

KAMRAN MOSTASHAR NEMATI

Committee in charge:

Professor Paulo J. M. Monteiro, Chair

Professor Ben C. Gerwick, Jr.

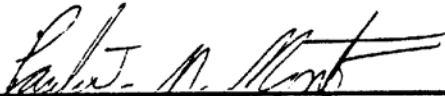
Professor Robert Brady Williamson

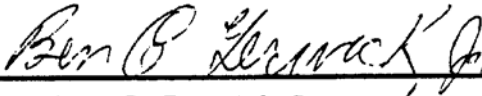
Professor Alice M. Agogino

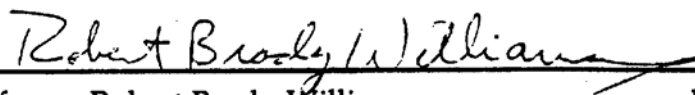
DECEMBER, 1994

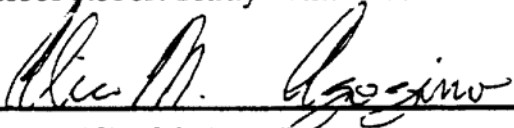
**DEPARTMENT OF CIVIL ENGINEERING
UNIVERSITY OF CALIFORNIA, BERKELEY
BERKELEY, CALIFORNIA**

The dissertation of Kamran Mostashar Nemati is approved:

 12/14/94
Professor Paulo J.M. Monteiro, Chair Date

 12/11/94
Professor Ben C. Gerwick, Jr. Date

 12/10/94
Professor Robert Brady Williamson Date

 12 Dec '94
Professor Alice M. Agogino Date

University of California at Berkeley

1994

**Generation and Interaction of Compressive
Stress-Induced Microcracks in Concrete**

Copyright© (1994)

by

Kamran Mostashar Nemati

ABSTRACT

Generation and Interaction of Compressive Stress-Induced Microcracks in Concrete

by

Kamran Mostashar Nemati

Doctor of Philosophy in Civil Engineering
University of California at Berkeley
Professor Paulo J. M. Monteiro, Chair

This thesis presents the results of experimental and theoretical studies of the micromechanical behavior of concrete under different loading conditions. Cylindrical specimens of normal and high-strength concrete were subjected to testing under uniaxial and confined compression. An alloy with a low melting point was used as a pore fluid. At the stress or strain of interest, this alloy was solidified to preserve the stress-induced microcracks as they exist under load.

Scanning electron microscopy (SEM) was employed to capture images from the cross sections of the concrete specimens. These images were then used to study the generation, orientation, density, length, and branching of the compressive stress-induced microcracks and the effect of confinement on microcrack behavior. The microcracks were generated by a number of different mechanisms and had an orientation that was generally within 15 degrees of the direction of the maximum applied stress. The density, average length, and branching of the microcracks decreased as the confining stress increased. The confining stress showed a pronounced influence on interfacial cracks, also known as transition zone cracks, which occur at the interface of cement paste and aggregate. The amount of interfacial cracking decreased significantly as the confining stress was increased. Stereological analysis which interprets three-dimensional structures by means of two-dimensional sections, was used on the computerized images. Crack orientation, crack surface area, and crack length

were determined stereologically. The resulting stereological measurements indicated that the crack orientation, surface area, and length decreased as the confining stress increased.

Three micromechanical models, the differential scheme, the Mori-Tanaka method, and a crack growth simulation model were used to examine the experimentally obtained data against the theoretically developed micromechanical models. The final modulus of elasticity for the concrete specimens was calculated using the first two models, based on the measured crack densities, which gave an approximation that was very close to the actual measured moduli. The crack growth model was used to generate and propagate microcracks for uniaxial and fully confined cases, and it also revealed behavior similar to that shown in the experimental results.



Paulo J. M. Monteiro
Chairman, Thesis Committee

To my parents

ACKNOWLEDGMENT

During my years of graduate study at Berkeley many people have given me support, guidance, and friendship. Foremost among these is my adviser, Professor Paulo Monteiro. He has shared his great creative and analytical skills with patience, endless encouragement, and generosity. It has been my very good fortune to have had such a conscientious and inspirational adviser.

Much credit also goes to my mentor and exemplar, Professor Ben C. Gerwick, Jr., who inspired me to study concrete. I owe a great deal of my success to Professor Gerwick. I would also like to thank the other members of my research committee, Professors Robert Brady Williamson and Alice M. Agogino for their detailed and thoughtful comments.

I wish to express appreciation to Professor Neville G. W. Cook of the Department of Mining Engineering and Dr. Larry Myer of Lawrence Berkeley Laboratory for their guidance in designing the test apparatus and for advice on experimental procedures. Special thanks goes to Mr. William MacCracken of the Department of Civil Engineering for his insight and ingenuity in conducting experiments.

The hospitality of Dr. Karen Scrivener during my many visits to the Imperial College of Science and Technology in London is greatly appreciated. Dr. Scrivener's advice was extremely valuable and pivotal. I also wish to thank Dr. Stephen Laing for his help in computer programming and for his friendship.

I am grateful to both Professor John Kemeny of the University of Arizona, and Dr. Robert Zimmerman of Lawrence Berkeley Laboratory, for their help with micromechanical modeling of fractures in concrete.

I would like to express my deepest gratitude and appreciation to ICF Kaiser Engineers, Inc. In particular I wish to thank Mr. Michael Jones and Mr. Richard Nunes for their patience, support, and encouragement, as well as for allowing me to maintain full-time employment while completing my graduate work. I could not have finished my doctorate without their support. I would also like to

thank Diane Michelle Williams, Dr. Edgar Becker, Mike Phillips, and Steve Sims for their friendship and encouragement.

The years I have spent in residence at the International House at Berkeley have constituted the best time of my life. I am exceedingly lucky to have made such great friends there as Peter Kennedy, Orla Feely, Jerry Murphy, Cormac Conroy, Bo Petterson, Nathalie Richart, Michel Chalhoub, Catherine Faure, Dariush Mirfendereski, Alison Green, Nils Tarnow, Hamid Savoj, and Yutaka Tanaka.

Finally, I would like to thank my late father and my mother for their constant concern, support, and encouragement throughout my life. There is no better way to express my appreciation than to dedicate this thesis to my parents.

TABLE OF CONTENTS

Abstract	1
Acknowledgments	iv
Table of Contents	vi
List of Figures	x
List of Tables	xvi
Nomenclature	xvii

CHAPTER 1 INTRODUCTION

1.1 Background	1
1.2 Methods of Study of Microcracking	4
1.2.1 Early Methods	5
1.2.2 Proposed Method	8
1.3 Objectives.....	9
1.4 Summary of the Chapters	10

CHAPTER 2 EXPERIMENTAL TECHNIQUE

2.1 Introduction.....	12
2.2 Concrete Specimens	12
2.3 Confinement.....	15

2.4 Test Equipment.....	18
2.4.1 Pedestal.....	18
2.4.2 Vessel.....	19
2.4.3 Piston.....	19
2.4.4 Top Cap.....	20
2.4.5 Heater.....	21
2.5 Wood's Metal.....	21
2.6 Experimental Procedure.....	22
2.7 Experiments Conducted.....	28
2.8 Specimen Preparation.....	29
2.8.1 Cutting.....	29
2.8.2 Polishing.....	30
2.8.3 Specimen Identification.....	31
2.8.4 Preparation for Scanning Electron Microscope (SEM) Analysis.....	32

CHAPTER 3 SCANNING ELECTRON MICROSCOPY, IMAGE ANALYZER, AND STEREOLOGY

3.1 Introduction.....	33
3.2 Scanning Electron Microscopy.....	33
3.3 Image Analyzer.....	35
3.4 Stereology and Concrete.....	37
3.4.1 Introduction.....	37
3.4.2 Basic Measurements.....	37

3.4.2.1	Number of point intersections, P_L	38
3.4.2.2	Surface-to-Volume ratio, S_V	39
3.4.2.3	Length of line per unit area, L_A	41
3.4.3	Degree of Orientation	44
3.4.4	Application of Stereology To Concrete Fracture Mechanics.....	45

CHAPTER 4 OBSERVATION RESULTS AND ANALYSIS OF DATA

4.1	Introduction.....	50
4.2	Characterization of Microcrack Initiation.....	50
4.3	Orientation of Microcracks.....	56
4.4	Microcrack Density Distribution.....	64
4.5	Microcrack Length Distribution.....	72
4.6	Microcrack Branching.....	81
4.7	Interfacial Cracks	83

CHAPTER 5 MICROMECHANICAL MODELS FOR CONCRETE

5.1	Introduction.....	91
5.2	Elastic Modulus Models	91
5.2.1	Differential Scheme.....	92
5.2.2	Mori-Tanaka Model	96
5.3	Crack Growth Simulation Model.....	98
5.3.1	The Maximum Energy Release Rate Criterion, G -Criterion.....	98
5.3.2	Crack growth and Propagation.....	100

5.3.3	Review of Analytical Micromechanical Model	102
5.3.4	Distribution of Microcracks in the Material	102
5.3.5	Parameters Used in the Crack Growth Model	105
5.3.6	Program Overview	108
5.3.7	The Crack Growth Simulation Model Results	110
CHAPTER 6 SUMMARY, CONCLUSION, AND RECOMMENDATIONS		
6.1	Summary of the Work Performed.....	114
6.2	Summary of Findings and Conclusion.....	115
6.3	Recommendations for Future Research	117
REFERENCES.....		119
APPENDICES.....		129
Appendix A:	Experiments Conducted.....	130
Appendix B:	Image Analyzer Computer Programs.....	134
Appendix C:	Test Cell Design.....	155

LIST OF FIGURES

Figure 1.1	Polished section from a concrete specimen.	2
Figure 1.2	Diagrammatic representation of the transition zone and bulk cement paste in concrete.....	3
Figure 2.1	Normal-strength concrete specimens used in the experiments...14	14
Figure 2.2	Pedestal	18
Figure 2.3	Vessel.....	19
Figure 2.4	Piston.....	20
Figure 2.5	top Cap.....	20
Figure 2.6	Wood's metal	21
Figure 2.7	Diagram of the test apparatus	23
Figure 2.8	Heating scheme diagram.....	24
Figure 2.9	Schematic diagram of the test assembly	24
Figure 2.10	Pouring molten metal into the vessel	25
Figure 2.11	Inserting the thermocouple into the top cap	25
Figure 2.12	Placing the heater and the insulation	26
Figure 2.13	Temperature and load control devices.....	26
Figure 2.14	Nitrogen dispensed through a high pressure regulator	27
Figure 2.15	Post-experiment cooling of the cell.....	27
Figure 2.16	Extrusion of concrete specimen.....	28
Figure 2.17	Raising the vessel.....	28

Figure 2.18	Raising the vessel by aircraft cable	28
Figure 2.19	Specimen prior to and after Wood's metal injection	28
Figure 2.20	Axial cut of the concrete cylinder.....	29
Figure 2.21	Lateral cut of the concrete cylinder.....	29
Figure 2.22	Specimen extraction	29
Figure 2.23	A lateral section showing macrocracks filled with metal alloy ...	30
Figure 2.24	Specimen placed on glass and aluminum base for SEM study	30
Figure 2.25	Specimen extraction and numbering scheme.....	31
Figure 3.1	Scanning electron microscope (SEM) and Kontron Image Analyzer.....	35
Figure 3.2	Flow chart for stereological steps.....	36
Figure 3.3	Model of deriving the relationship $S_V = 2P_L$	39
Figure 3.4	Geometry involved in the determination of the probability that random normals lie between θ and $\theta + d\theta$	40
Figure 3.5	Model of deriving the relationship $L_A = (\frac{\pi}{2})P_L$	42
Figure 3.6	Geometry involved in the determination of the probability that elementary segments lie between θ and $\theta + d\theta$	43
Figure 3.7	A SEM backscatter image.....	46
Figure 3.8	Establishing threshold in histogram.....	46
Figure 3.9	Wood's metal identification by establishing threshold levels in histogram	47
Figure 3.10	Crack network.....	47
Figure 3.11	Scrap command	47
Figure 3.12	Binary-thinned image of the crack network in concrete.....	48

Figure 3.13	Array of straight parallel lines.....	49
Figure 4.1	SEM micrographs from the no-load experiment	51
Figure 4.2	SEM micrographs from the partially confined experiment	52
Figure 4.3	SEM micrographs of microcracks propagating from a pore.....	52
Figure 4.3	SEM micrographs of aggregate cracking	53
Figure 4.5	SEM micrographs from the no-load experiment for high-strength concrete specimen.....	54
Figure 4.6	SEM micrographs from the partially confined experiment for high-strength concrete	55
Figure 4.7	Average crack orientation for normal-strength concrete.....	56
Figure 4.8	Average crack orientation for high-strength concrete	57
Figure 4.9	Crack orientation for normal-strength concrete.....	59
Figure 4.10	Crack orientation for high-strength concrete	59
Figure 4.11	Number of intercepts for smoothed cracks	60
Figure 4.12	Number of intercepts for smoothed cracks	60
Figure 4.13	Rose of the number of intersections diagrams for high-strength concrete.....	61
Figure 4.14	Rose of the number of intersections diagrams for normal-strength concrete.....	62
Figure 4.15(a)	SEM micrographs showing crack tips at higher magnification.....	63
Figure 4.15(b)	SEM micrographs showing crack tips at higher magnification.....	64
Figure 4.16	Crack density, Γ , as a function of confinement for normal-strength concrete.....	66
Figure 4.17	Crack density, Γ , as a function of confinement for high-strength concrete.....	66

Figure 4.18	Diagrammatic representation of crack length and crack density at confined and unconfined portions of Experiment #3.....	67
Figure 4.19	Diagrammatic representation of crack length and crack density at confined and unconfined portions of Experiment #4.....	68
Figure 4.20	Number of cracks as a function of confinement for normal-strength concrete.....	68
Figure 4.21	Number of cracks as a function of confinement for high-strength concrete.....	69
Figure 4.22	Percent cracked area as a function of confinement for normal-strength concrete.....	69
Figure 4.23	Percent cracked area as a function of confinement for high-strength concrete.....	70
Figure 4.24	Crack surface area (S_v) as a function of confinement condition for normal-strength concrete	71
Figure 4.25	Crack surface area (S_v) as a function of confinement condition for high-strength concrete	71
Figure 4.26	Crack length as a function of confinement condition for normal-strength concrete	72
Figure 4.27	Crack length as a function of confinement condition for high-strength concrete.....	72
Figure 4.28	Histogram of microcrack length distributions for the no-load experiment of the normal-strength concrete	73
Figure 4.29	Histogram of microcrack length distributions for the uniaxial experiment of the normal-strength concrete	73
Figure 4.30	Histogram of microcrack length distributions for the partially confined (1) experiment of the normal-strength concrete	74
Figure 4.31	Histogram of microcrack length distributions for the partially confined (2) experiment of the normal-strength concrete	74
Figure 4.32	Histogram of microcrack length distributions for the fully confined experiment of the normal-strength concrete.....	75

Figure 4.33	Histogram of microcrack length distributions for the no-load experiment of the high-strength concrete	75
Figure 4.34	Histogram of microcrack length distributions for the uniaxial experiment of the high-strength concrete	76
Figure 4.35	Histogram of microcrack length distributions for the partially confined experiment of the normal-strength concrete.....	76
Figure 4.36	COV of crack length as a function of confinement for normal-strength concrete.....	77
Figure 4.37	COV of crack length as a function of confinement for high-strength concrete.....	78
Figure 4.38	Stress intensity factors due to local tension P and confining stress, σ_3	78
Figure 4.39	Stereological measurement of crack length as a function of confinement condition for normal-strength concrete specimens.....	80
Figure 4.40	Stereological measurement of crack length as a function of confinement condition for high-strength concrete specimens.....	80
Figure 4.41	3-way and 4-way crack branching nodes.....	81
Figure 4.42	Crack branching nodes as a function of confinement for normal-strength concrete	82
Figure 4.43	Crack branching nodes as a function of confinement for high-strength concrete	82
Figure 4.44	The flow chart for interfacial crack identification computer program.....	84
Figure 4.45	Interfacial crack in the normal concrete specimen subjected to uniaxial loading.....	85
Figure 4.46	Scrap with the higher upper limit for the area range.....	86
Figure 4.47	Scrap with the lower upper limit for the area range	86
Figure 4.48	Close the image in Figure 4.47	86

Figure 4.49	Open the image in Figure 4.48.....	86
Figure 4.50	Scrap the image in Figure 4.49.....	87
Figure 4.51	Correlate every pixel which is both in figure 4.46 and 4.50	87
Figure 4.52	Correlating every pixel that is either in Figure 4.46 or 4.49 but not common to them	87
Figure 4.53	Scrap the image in Figure 4.52.....	87
Figure 4.54	Scrap the image in Figure 4.52.....	88
Figure 4.55	Crack smoothing of the image in Figure 4.54.....	88
Figure 4.56	Effect of confinement on interfacial microcracks of normal- strength concrete.....	89
Figure 4.57	Effect of confinement on interfacial microcracks of high- strength concrete.....	90
Figure 5.1	Schematic diagram of an idealized crack.....	93
Figure 5.2	(a) Plate with crack $2a$; (b) Load-displacement diagram	100
Figure 5.3	Computer flow chart for the Du model calculations	102
Figure 5.4	Histogram of entire microcrack length distribution for the no-load experiment on normal-strength concrete	104
Figure 5.5	The random cracks generated in concrete specimen.....	105
Figure 5.6	Concrete specimen boundary input in algorithm.....	108
Figure 5.7	Rectangular boundary	109
Figure 5.8	Crack propagation simulation for uniaxial loading	111
Figure 5.9	Crack propagation simulation for fully confined condition	112

LIST OF TABLES

Table 2.1	Normal-strength concrete mix design	13
Table 2.2	High-strength concrete mix design	13
Table 2.3	Experiments conducted.....	29
Table 3.1	List of basic stereological symbols and their definition	38
Table 4.1	Number, length, and orientation of microcracks	57
Table 4.2	Data from the stereological analysis	58
Table 4.3	Crack density for different loading conditions.....	65
Table 4.4	Coefficient of variation of cracks length.....	77
Table 4.5	Percentage of interfacial cracks.....	89
Table 5.1	Modulus of elasticity obtained from micromechanical Models....	98
Table 5.2	The microcrack lengths used in the Du model	104
Table 5.3	Material properties of concrete specimen	107

NOMENCLATURE

Å	Angstrom
f'_c	Ultimate Strength
FM	Fineness Modulus
GPa	Giga Pascal
K	Coefficient of Permeability
KN	Kilo Newton
lb	Pound
HRWR	High Range Water Reducer
LEFM	Linear Elastic Fracture Mechanics
MPa	Mega Pascal
µm	Micrometer (10^6 m)
MSA	Maximum Size Aggregate
pcf	Pounds per Cubic Feet
pcy	Pounds per Cubic Yard
psi	Pounds per Square inch
RHA	Rice Husk Ash
SEM	Scanning Electron Microscope
yd	Yard

Chapter 1

INTRODUCTION

1.1 BACKGROUND

Concrete is a heterogeneous, multiphase material. On a macroscopic scale, it is a mixture of cement paste, fine aggregates in a range of sizes and shapes, large aggregates in a range of gradations, and various types of void spaces. At the microscopic and submicroscopic levels, concrete is heterogeneous when the paste is observed to be a mixture of different types of crystalline structures, at varying degrees of hydration, which form an amorphous gel. Loss of water to the hydration of cement particles and evaporation, as well as entrained and entrapped air, cause voids to form in the heterogeneous mass. Examination of a cross section of concrete (Figure 1.1) reveals two phases that can be easily distinguished: aggregate particles of varying size and shape, and the binding medium which is composed of an incoherent mass of hydrated cement paste. At the macroscopic level, therefore, concrete may be considered to be a two-phase material, consisting of aggregate particles dispersed in a matrix of cement paste.

At the microscopic level, the complexities of the concrete structure begin to appear. It becomes obvious that the two phases of the structure are neither homogeneously distributed with respect to each other, nor are they themselves homogeneous. The structure of hydrated cement paste in the vicinity of large aggregate particles is usually very different from the structure of bulk paste or mortar in the system. Many aspects of concrete behavior under stress can be explained only when the cement paste-aggregate interface is treated as a third phase of the concrete structure. Therefore, in order to study the structural behavior of concrete, it is most helpful to view this complex mass as a three-phase composite structure: a coherent mortar phase and fine aggregate, bonded to an aggregate phase which is the coarse or large aggregate itself; and the transition zone which represents the interfacial region between the particles of coarse aggregate and the hydrated cement paste. The transition zone which

exists as a thin shell, typically 10 to 50 μm thick around large aggregate, is generally weaker than either of the two main components of concrete, and it therefore imposes a far greater influence on the mechanical behavior of concrete than is reflected by its size.

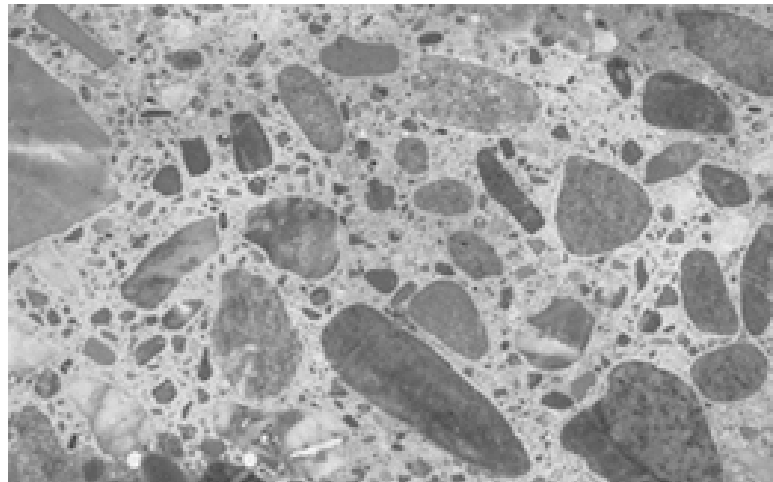


Figure 1.1 Polished section from a concrete specimen

In order to understand the structural characteristics of the transition zone, the sequence of its development is presented here as described by Maso (1980). In freshly compacted concrete, water films form around the large aggregate particles. This would account for the higher water/cement ratio that exists closer to larger aggregate than in the bulk mortar. Next, as in the bulk paste, calcium, sulfate, hydroxyl, and aluminate ions, produced by the dissolution of calcium sulfate and calcium aluminate compounds, combine to form ettringite (C-A-S-H) and calcium hydroxide (CH). Owing to a high water/cement ratio, these crystalline products in the vicinity of coarse aggregate consist of relatively large crystals, and therefore form a more porous framework than in bulk cement paste or mortar matrix. The platelike calcium hydroxide crystals tend to form in oriented layers, for instance, with the c -axis perpendicular to the aggregate surface. Finally, with the progress of hydration, poorly crystalline C-S-H and a second generation of smaller crystals of ettringite and calcium hydroxide start filling the empty space that exists between the framework created by the large ettringite and calcium hydroxide crystals. This helps to improve the density and

hence the strength of the transition zone. Figure 1.2 is a diagrammatic representation of the transition zone in concrete.

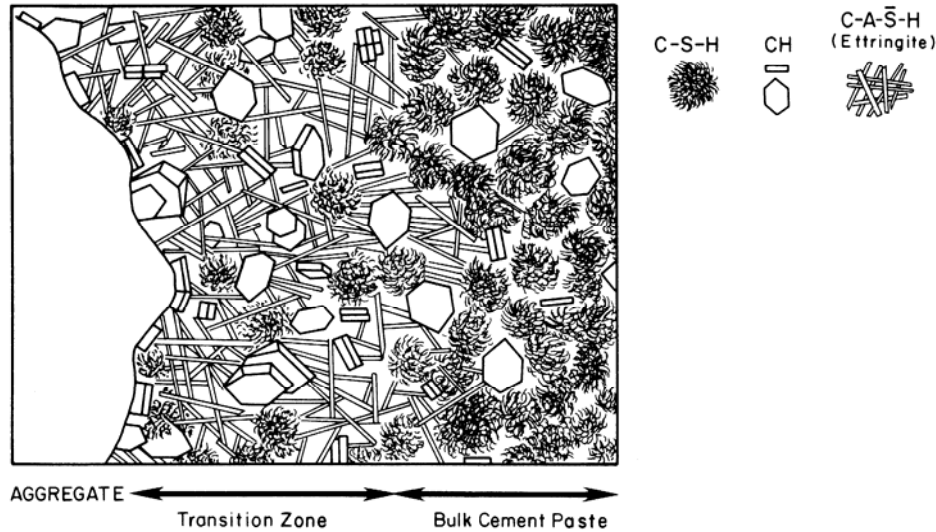


Figure 1.2 Diagrammatic representation of the transition zone and bulk cement paste in concrete (Mehta and Monteiro 1993)

In such a model, defects known as *microcracks* are imposed upon the three-phase composite. Bond cracks known as transition zone microcracks, may occur at mortar-aggregate interfaces, while mortar and aggregate cracks occur in the mortar and aggregate, respectively.

A quantitative connection between fracture stress and flaw size came from the work of Griffith (1920, 1924). He used the results obtained by Inglis (1913), and applied a stress analysis of an elliptical hole to the unstable propagation of a crack. According to the first law of thermodynamics, when a system goes from a nonequilibrium state to equilibrium, there will be a net decrease in energy. A crack can form (or an existing crack can grow) only if such a process causes the total energy to decrease or remain constant. Thus the critical conditions for fracture can be defined as the point where crack growth occurs under equilibrium conditions, with no net change in total energy (Anderson 1991). Griffith invoked the first law of thermodynamics to formulate a fracture theory based on simple energy balance. According to his theory, a flaw becomes unstable, and thus fracture occurs, when the strain energy change that results from an increment of crack growth is sufficient to overcome the surface energy of

the material. Griffith's model correctly predicted the relationship between strength and flaw size in glass specimens. Since this model assumes that the work of fracture comes exclusively from the surface energy of the material, the Griffith approach only applies to ideally brittle solids.

Although the general relationships between stress level and crack development are reasonably well understood in concrete, the origin and development of cracks in concrete composite systems is still uncertain. In an effort to explore these issues, the theory of linear elastic fracture mechanics (LEFM) has been extended and applied to cement and concrete. These studies, however, have not been very successful; this may be because the observations they made about the way small cracks form and propagate in these materials were very limited.

Since the 1920s, researchers have suggested and assumed the existence of different kinds of defects that occur in concrete called microcracks (Richart 1929; Jones 1952; L'Hermite 1954; Hognestad et al. 1955; Czernin 1962; Hsu et al. 1963). However, only since the early 1960s have such cracks been carefully observed, measured, and characterized in interior portions of the system (Hsu 1963; Hsu and Slate 1963; Hsu et al. 1963; Slate and Olsefski 1963). These microcracks were verified and, to some extent, defined by microscopic study. This trend continued up until the middle 1970s when, finally, major advances were made. The contributions were based on the development of nonlinear fracture mechanics models, where the structure and behavior of concrete could be taken into account. In the 1980s and 1990s, intensive research has been performed. Applications of fracture mechanics in the design of beams, anchorage, and large dams are now becoming more common. In spite of this, the theory of fracture mechanics in concrete is not yet as mature as other continuum theories, such as elasticity, viscoelasticity, and thermal problems.

1.2 METHODS OF STUDY OF MICROCRACKING

The investigation of *microcracking* ranges from a macroscopic study of the behavior of cracked specimens to a microscopic study of the cracks themselves. The presence of microcracks was predicted on the basis of macrobehavior and verified by microscopic study.

1.2.1 Early Methods

Several methods have been used to study the microcracking of concrete. Some of those methods are as follows:

1.2.1.1 Acoustic emission. This method involves an investigator “listening” to the test specimen to detect the occurrence of internal cracking. The sophistication of the test depends on the type and sensitivity of the acoustic emission amplification, collecting, and recording equipment (Jones 1952; L’Hermite 1954; Hamstad 1986). An acoustic emission (AE) is a localized, rapid release of strain energy in a stressed material. AE is a microseismic wave generated by microcracking, dislocation movement, phase transformation, and other irreversible changes in a stressed material. These waves can be detected on the surface of the material by transducers which convert the mechanical acoustic vibrations to electric signals which are digitized, stored, and analyzed to obtain useful information about the AE events (Maji et al. 1990). Acoustic emission differs from most nondestructive methods in that the energy detected is released from within the test object rather than being supplied by an external source such as ultrasonic or radiography. Acoustic emission techniques are also capable of detecting the dynamic processes associated with the degradation of structural integrity (Ouyang et al. 1991).

1.2.1.2 Sonic testing. This method involves using resonant frequency to measure the apparent velocity of sound waves traveling through an elastic continuum. The velocity at which sound waves pass through an uncracked concrete specimen depends on the geometry and density of the concrete specimen. A crack in the specimen represents a discontinuity across which a sound wave cannot pass efficiently. Sound waves in a cracked specimen must pass around microcracks, thus traveling a further distance than in an uncracked specimen. The travel time for the cracked specimen is therefore greater than for the uncracked specimen (Whitehurst 1966). This method detects the presence of cracking by recording the increase in sound wave travel time in proportion to the increase in discontinuities in the elastic medium as the compressive load on the concrete specimen is increased. It has also been shown that the measurements of ultrasonic waves in mortar can be a powerful and reliable method of analyzing the elastic properties (Monteiro et al. 1988).

1.2.1.3 *Microscope and X-ray techniques.* These have been used at Cornell University since the 1960s to intensively study the interior cracks, as opposed to the surfaces, of concrete specimens. The following three procedures are representative of several methods studied at Cornell University involving radiant energy.

1.2.1.3.1 *Hydrophilic tracer liquid technique.* A hydrophilic tracer liquid, such as a fluorescent aqueous system, is allowed to penetrate cracks and voids in a slightly dried, cut, and polished surface. Afterwards the surface is lightly ground to remove the surface film of the tracer liquid. The cracks and voids shown by the tracer liquid which penetrated them can then be directly observed or photographed in a darkroom under ultraviolet radiation. The fluorescence method is useful, but cumbersome; it is not conducive to detailed, prolonged study such as can be done readily with the optical microscope (Wittmann 1983).

1.2.1.3.2 *Dye technique.* The bottom face of a slightly dried slice of ½-to 1-centimeter-thick concrete is placed in a container of an aqueous dye without being submerged. The capillary rise of the dye brings it to the top surface through the cracks. The colored cracks are then observed or photographed. This method does not work well because the internal surfaces of the cracks absorb most of the dye during the capillary rise. Additionally, many or most of the cracks may not be continuous for an appreciable distance (Wittmann 1983).

1.2.1.3.3 *Lead salt.* A partially dried, thin slice of concrete is subjected to the capillary rise of a saturated water solution of a lead salt. X-ray is then used to identify cracks and voids that were once relatively opaque (Wittmann 1983).

1.2.1.4 *Microscope technique with dye.* The clean, surface-dried face of a specimen 0.15 to 3 inches (4 to 75 mm) thick is painted with carmine drawing ink, which then penetrates the voids and cracks. After the ink becomes surface dry on all the paste portions, the inked surface is ground wet until only a faint pink color can be seen by the naked eye. Cracks and voids thus dyed contrast visibly with the rest of the surface of the specimen. A stereomicroscope is used to observe the cracks, which are then sketched or photographed as observed (Slate and Olsefski 1963; Hsu et al. 1963).

1.2.1.5 Mercury intrusion porosimetry. This entails using high pressure to infuse mercury into the concrete structure. This technique makes it possible to determine the size and quantity of void spaces and pores as well as particle size distribution. Information regarding the shape and structure of pores can also be obtained from the volume of mercury expelled from the pores as a function of decreasing pressure (Orr 1969).

1.2.1.6 X-ray technique. Since meaningful observations and studies of cracks must focus on cracks on the interior of the specimen rather than on the exterior surface, the method of using X-ray was developed for observation at depth within concrete. The first use of X-radiography to study cracks and other internal structural features of concrete was that developed and used by Slate and Olsefski (1963). They used an industrial X-ray unit, with a rating of 150 kilovolts (KV), and directly X-rayed thin specimens of concrete after cracks were induced, or after simply curing. Even relatively small variations in the thickness of specimens caused significant differences in the darkness of the X-ray film. Specimens that were too thick yielded too much detail, causing confusion in the interpretation of the X-ray plates, or loss of definition of very small cracks which extended only a small part of the way through the specimen. Specimens that were too thin sometimes had cracks induced by the sawing process. Later, thin ($\frac{1}{2}$ inch or 13 mm) plates of models of concrete were loaded under uniaxial and biaxial compression and in tension, X-ray film was placed under the specimens, and radiation was passed through the specimens to expose film after film during loading. This resulted in a nondestructive test which showed progressive cracking and failure, as described by Buyukozturk et al. (1971, 1972), by Liu et al. (1972), and by Carino and Slate (1976).

1.2.1.7 Computerized tomography analysis. γ -ray computerized tomography (CT) has been used as a nondestructive method to assess the degree of distress existing in reinforced concrete members (Martz et al. 1993). Different specimen configurations were employed to study the determination of voids and location of reinforcing bars. The objective of γ -ray CT is to reconstruct object absorption cross sections from projections through the object by using CT scanners. When the scanner cannot fully surround the reinforced concrete structure, the problem of limited-angle tomography can occur.

1.2.1.8 Fiber optics. Using a special device, optical fibers are used to detect the formation and propagation of one or more cracks in a material containing a hydraulic binder, such as concrete. The operation of the device is based on the finding that an optical fiber embedded in a piece of concrete breaks as soon as a crack, propagating in the material surrounding, it reaches it; and that this break causes an almost complete disappearance of the luminous signal transmitted by the fiber (Rossi and Le Maou 1989).

1.2.1.9 Holographic interferometry. In this method, reflection holographic interferometry is used to characterize the initiation and propagation of microcracks in cement-based composites (Mobasher et al. 1990). Holographic interferometry makes it possible to observe a large area of the specimen with no surface preparation required. The whole-field capacity of holographic interferometry can allow real-time observations of gradual curvature of the propagating crack with high accuracy (Maji and Shah 1990). Unlike optical microscopy, which measures the total number of cracks developed, holographic interferometry is an incremental-displacement measurement technique which makes it possible to differentiate between previously existing and active cracks, cracks that open or propagate, at any load level. Holographic interferometry technique has been used to determine the fracture process zone of mortar and concrete (Regnault et al. 1990).

Almost all of the above-mentioned techniques failed to render accurate representations of the geometry and state of microcracks as they exist under load. Some of the techniques are limited in their resolution, sensitivity in detecting cracks, and ability to make full-field observations. Other methods are incapable of examining the specimen while under load; or they require special preparation of the specimen, which alters its behavior.

1.2.2 Proposed Method

The proposed method involves the application of a metal in liquid phase, *Wood's metal*, which has a melting point below the boiling point of water, to preserve the microstructure of stress-induced microcracks in concrete. Used in conjunction with scanning electron microscopy (SEM), it has made possible the detailed observation of microcracks in concrete as they exist under load. Named

after the astronomer who used an alloy of bismuth, lead, tin, and cadmium to create a perfect parabolic surface for astronomical observations, Wood's metal has been used in the past few years to study the microstructure of different materials. Yadev (1984) used Wood's metal to study pore fluid porosimetry and to measure contact areas and voids between the surfaces of natural fractures. Pyrak (1988) used Wood's metal to study the fracture of rocks. Zheng (1989) used Wood's metal to fill voids and microcracks in clastic rock specimens during loading and solidified it before unloading to preserve the microstructure in specimens under load.

This research expands the application of Wood's metal as a preservative of the microstructure of concrete under applied compressive stresses. In this study microcracks induced in concrete by applied stresses were preserved and identified, employing the method introduced by Zheng (1989), in order to understand the mechanisms by which stress-induced microcracks generate and interact.

Eight concrete cylinders-five normal-strength and three high-strength-each 8 inches (203 mm) long by 4 inches (102 mm) in diameter, were tested at the structural engineering laboratory of the University of California at Berkeley. Wood's metal was used to preserve the cracks induced in concrete by various stresses. After the metal was solidified, each of the cylinders was sectioned into eight specimens. The specimens were observed at the materials department of the Imperial College of Science and Technology at the University of London, using JEOL JSM-35CF scanning electron microscopy (SEM). Fifty-five images were taken from each specimen. The SEM images were then analyzed using an image analyzing system.

1.3 OBJECTIVES

The objectives of this investigation are as follows:

1. Examine the mechanisms for the generation of stress-induced microcracks in concrete under compression, and establish the effect of microstructure on the generation of stress-induced microcracks.

2. Determine the real shapes and geometry of stress-induced microcracks as they exist under load.
3. Assess how the density, length, orientation, localization, and behavior of microcracks depend upon the confining stresses.
4. Evaluate the interactions between microcracks and provide experimental information for micromechanical models, such as crack growth, under sustained load.
5. Determine the shapes of the stress-induced microcracks in three dimensions, and the relationship of microcrack planes to the boundary of the specimen.
6. Ascertain whether the microstructure or the stress conditions are the major factors that control the propagation of microcracks once they are generated.
7. Compare the experimental results obtained in this research with some of the existing micromechanical models and determine whether a simple numerical model could be used to simulate the interactive effect of existing microcracks on the location of new microcracks to be generated.

1.4 SUMMARY OF THE CHAPTERS

The chapters describing the work performed in this study were divided in such a way that they are predominantly self-contained. In order to help the reader to obtain a better understanding of the topics covered, a summary of Chapters 2 to 6 is presented below:

CHAPTER 2

This chapter explains the experimental technique used to preserve the compressive stress-induced microcracks in concrete. The components of the special test equipment that was developed for this research, as well as the concrete specimens, the metal alloy-Wood's metal-used to fill the voids and compressive stress-induced cracks in concrete, and the experimental procedure, are described in detail. Confinement and its

effect on microcrack behavior is discussed. The experiments conducted and specimen preparation for scanning electron microscopy (SEM) study are discussed.

CHAPTER 3

The use of scanning electron microscopy (SEM) to extract images from the concrete specimens for different testing conditions is explained. The images rendered were analyzed using an image analyzer. The image analyzer identifies Wood's metal, which represents the crack network in concrete specimens. Special computer programs were developed to perform stereological and two-dimensional measurements on the stress-induced cracks in concrete. The scanning electron microscope and the computer programs used are described. Stereology deals with the interpretation of three-dimensional structures from their two-dimensional sections. Stereology attempts to characterize numerically the geometrical aspects of features in the microstructure, such as microcracks in concrete represented by Wood's metal. The basic measurements and parameters used in stereological analysis and the application of stereology to concrete fracture mechanics are described in this chapter.

CHAPTER 4

The data obtained from the image analyzer and the micrographs from the scanning electron microscope (SEM) are analyzed and examined quantitatively and qualitatively in order to determine the characterization of microcrack initiation; orientation; density; length; crack branching; and interfacial cracks.

CHAPTER 5

The results of the analysis performed in Chapter 4 are compared to some of the existing models of fracture mechanics for composite materials.

CHAPTER 6

Summary, conclusion, and recommendations for future work.

Chapter 2

EXPERIMENTAL TECHNIQUE

2.1 INTRODUCTION

The experimental technique described here makes it possible to preserve the compressive stress-induced microcracks in concrete as they exist under applied loads. The results of these experiments can be used to better understand and quantify the general relationship between stress level and crack development, as well as the effects of confinement on crack behavior: crack orientation, crack density, crack length, crack localization, crack branching, interfacial cracks, etc. They will also facilitate investigations into the way small cracks form and then propagate in concrete, thus making the application of fracture mechanics to cement paste and concrete more realistic.

Special test equipment was created to preserve the cracks under applied load. This was accomplished by injecting a molten metal into the induced cracks and solidifying it before unloading. The experiments carried out involved three procedures:

- a) concrete casting and preparation,
- b) crack induction, and
- c) molten metal injection and solidification.

The second and third procedures were carried out simultaneously.

2.2 CONCRETE SPECIMENS

Five normal-strength and three high-strength concrete cylinders, 8 inches (203 mm) long by 4 inches (102 mm) in diameter, were cast using the mix designs shown in Tables 2.1 and 2.2. Both the normal-strength and high-strength concrete cylinders were cast at the Civil Engineering Materials Laboratory of the University of California at Berkeley.

Table 2.1 Normal-strength concrete mix design

NORMAL-STRENGTH CONCRETE	
MATERIAL	QUANTITY/TYPE
Cement	583 pcy (346 Kg/m ³)
Water	308 pcy (183 Kg/m ³)
Coarse Aggregate (Pea Gravel)	1,650 pcy (979 Kg/m ³)
Sand	1,448 pcy (859 Kg/m ³)
HRWR Admixture	15 oz/100 lb. Cement Weight
W/C	0.528
Slump	1.5 inches (38 mm)
Date of Cast	November 16, 1989
Strength (on March 4, 1992)	7,500 psi (51.7 MPa)

Table 2.2 High-strength concrete mix design

HIGH-STRENGTH CONCRETE	
MATERIAL	QUANTITY/TYPE
Cement Type I/II	600 pcy (356 Kg/m ³)
Rice Husk Ash (RHA)	90 pcy (53 Kg/m ³)
Crushed Limestone (3/8" MSA)	1,760 pcy (1,044 Kg/m ³)
Top Sand (FM=3.0)	1,325 pcy (768 Kg/m ³)
Water	215 pcy (128 Kg/m ³)
Superplasticizer Admixture	5.7 Liters/m ³
W/C	0.358
Slump	1 inch (25 mm)
Unit Weight	154 pcf (91 Kg/m ³)
Date of Cast	October 30, 1991
Strength (28-day f'_c)	11,000 psi (75.8 MPa)

The concrete cylinder ends were ground parallel to one another. Water was used as the cooling fluid during cutting and grinding. This procedure was performed at the Lawrence Berkeley Laboratory.

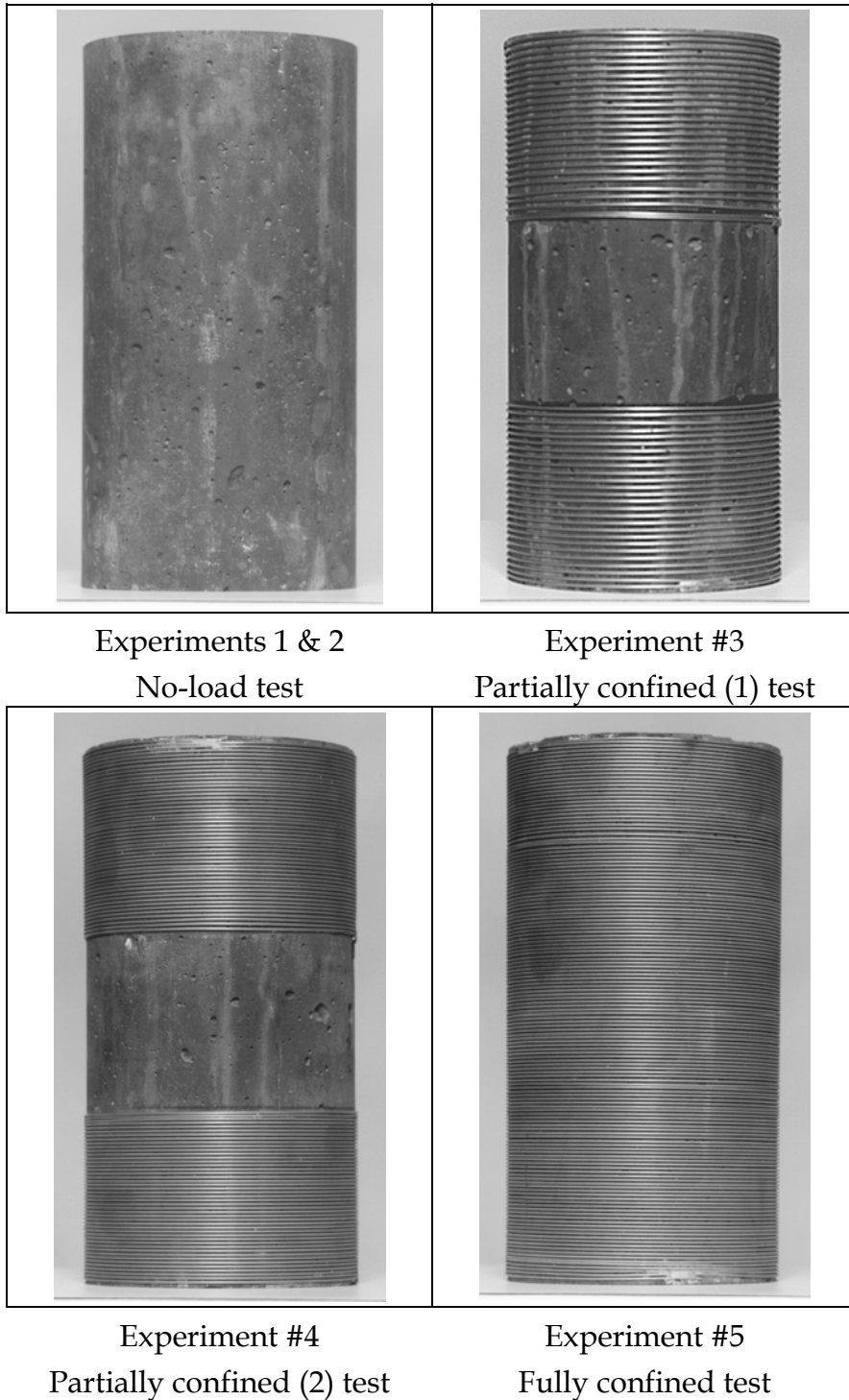


Figure 2.1 Normal-strength concrete specimens used in the experiments

Figure 2.1 represents the normal-strength concrete specimens used in Experiments 1 through 5. The high-strength concrete specimens used in Experiments 6, 7, and 8 resemble specimens used in Experiments 1, 2, and 3, respectively.

2.3 CONFINEMENT

The confining stress used to generate triaxial compression was supplied by stainless steel wires, 0.041 inch (0.3 mm) in diameter, that were wound around the concrete cylinders, both the entire length and one-third of the way from each end, at a pre-tension of 150 pounds (670 N). The purpose of the triaxial compression test was to observe the extensile microcracks generated under uniaxial compression in the middle of the concrete cylinder without causing unstable failure of the entire cylinder. The triaxial-compression test also eliminated the end effect caused by friction between the loading plates and the ends of the concrete cylinder because no failure occurred within the confined ends.

In a specimen subjected to uniaxial compression, most microcracks propagate to a certain length and stop. With the application of confining stress, the average length of the microcracks decreases. Coefficient α is the ratio of the incremental confining stress to the incremental axial stress and depends on the specimen diameter, elastic modulus, Poisson's ratio, and the pitch of the winding wire (Zheng 1989). Equation (2.1) is the expression for the coefficient α ,

$$\alpha = \frac{\Delta\sigma_r}{\Delta\sigma_a} = \frac{\Delta\varepsilon_r n \pi R_w^2 E_w}{R_s \Delta\sigma_a} \quad (2.1)$$

and the confining stress σ_r itself can be expressed as:

$$\sigma_r = \frac{\varepsilon_r n \pi R_w^2 E_w + n T_w}{R_s} \quad (2.2)$$

where: ε_r = radial strain of the specimen

R_s = radius of specimen

σ_a = axial stress on the specimen

n = number of turns of wire per unit specimen length (pitch⁻¹)

R_w = radius of wire

E_w = Young's modulus of wire

T_w = pre-tension on the wire.

Within the elastic range of the concrete the Poisson's ratio is constant. The ratio of $\frac{\Delta \varepsilon_r}{\Delta \sigma_a}$ can be shown as:

$$\frac{\Delta \varepsilon_r}{\Delta \sigma_a} = \frac{\Delta \varepsilon_r}{E_s \Delta \varepsilon_a} = \frac{\nu_s}{E_s} \quad (2.3)$$

Substituting Equation 2.3 in Equation 2.1, α can be expressed as:

$$\alpha = \frac{\nu_s n \pi R_w^2 E_w}{R_s E_s} \quad (2.4)$$

Multiplying the ratio in Equation 2.2 by E_s , it yields to:

$$\sigma_r = \frac{E_s \varepsilon_r n \pi R_w^2 E_w + n T_w E_s}{R_s E_s} \quad (2.5)$$

The Poisson's ratio of the specimen is:

$$\nu_s = \frac{\varepsilon_r}{\varepsilon_a} = \frac{\varepsilon_r}{\frac{\sigma_a}{E_s}} = \frac{E_s \varepsilon_r}{\sigma_a} \quad \text{or} \quad E_s \varepsilon_r = \nu_s \sigma_a \quad (2.6)$$

substituting Equation 2.6 in Equation 2.5, the confining stress can be shown as:

$$\sigma_r = \frac{\nu_s n \pi R_w^2 E_w \sigma_a + n T_w E_s}{R_s E_s} \quad (2.7)$$

where: ν_s = Poisson's ratio of the specimen

E_s = Young's modulus of the specimen (MPa or psi).

For the normal-strength concrete specimens:

$$R_s = 2 \text{ inches (51 mm)}$$

$$\sigma_a = 6,375 \text{ psi (44.63 MPa)}$$

$$n = 20 \text{ pitches/inch (8 pitches/cm)}$$

$$R_w = \frac{0.041 \text{ inches}}{2} = 0.0205 \text{ inches (0.5 mm)}$$

$$E_w = 28 \times 10^6 \text{ psi (196 GPa)}$$

$$T_w = 150 \text{ pounds (670 N)}$$

$$\nu_s = 0.15-0.20 \text{ (use 0.175)}$$

$$E_s = 3.5 \times 10^6 \text{ psi (24,500 MPa)}$$

Substituting the above values into Equation 2.7, σ_r can be computed as:

$$\sigma_r = \frac{(0.175)(20)\pi(0.0205 \text{ inch})^2(28 \times 10^6 \text{ psi})(6375 \text{ psi}) + (20)(150 \text{ lbs})(3.5 \times 10^6 \text{ psi})}{(2 \text{ inches})(3.5 \times 10^6 \text{ psi})}$$

or

$$\sigma_r = \frac{82.5 \times 10^7 + 1050 \times 10^7}{7 \times 10^6} \approx 1,620 \text{ psi (10.8 MPa)}$$

The maximum compressive stress, $\sigma_{p'}$, under biaxial loading, is a function of the principal stress ratio $\alpha = \sigma_r / \sigma_a$ and the uniaxial compressive strength f'_c (Chen 1982). The values of maximum stresses in the two principal directions σ_{rp} and σ_{ap} are obtained from the modified-biaxial-strength envelope of Kupfer and Gerstle (1973). In the compression-compression region ($\sigma_a = \text{compression}$, $\sigma_r = \text{compression}$, $0 \leq \alpha \leq 1$):

$$\sigma_{ap} = \frac{1 + 3.65\alpha}{(1 + \alpha)^2} f'_c \quad (2.8)$$

and

$$\sigma_{rp} = \alpha \sigma_{ap} \quad (2.9)$$

Therefore:

$$\alpha = \frac{\sigma_r}{\sigma_a} = \frac{1,620 \text{ (psi)}}{6,375 \text{ (psi)}} = 0.25$$

substituting for α and f'_c in Equation 2.8:

$$\sigma_{ap} = \frac{1 + 3.65(0.25)}{(1 + 0.25)^2} (7,500 \text{ psi}) = 9,180 \text{ psi} (61.6 \text{ MPa})$$

(20% increase) and from Equation 2.9,

$$\sigma_{rp} = (0.25)(9,180 \text{ psi}) \approx 2,295 \text{ psi} (15.4 \text{ MPa})$$

2.4 TEST EQUIPMENT

The equipment used for this research was specially designed and developed at the University of California at Berkeley. It consists of five pieces: pedestal, vessel, piston, top cap, and heater. Each piece is described and illustrated below. For detailed design drawings refer to Appendix 3.

2.4.1 Pedestal

Made of graphitized steel, the pedestal is a monotonic, solid cylinder with a circular plate, the diameter of which is greater at the middle, as shown in Figure 2.2. The cylinder is 5 inches (127 mm) long and 4.25 inches (108 mm) in diameter, except for the upper 1 inch (25 mm) which has a diameter of 4 inches (102 mm). The circular plate has a thickness of 1 inch (25 mm) and a diameter of 7.25 inches (184 mm). The vessel is placed on the circular plate. There is an o-ring groove on the cylinder above the circular plate to provide an airtight system after assembly. There are six equally spaced 1/2-inch (12.7 mm) through holes on the circular plate to accommodate bolts that secure the vessel to the pedestal.

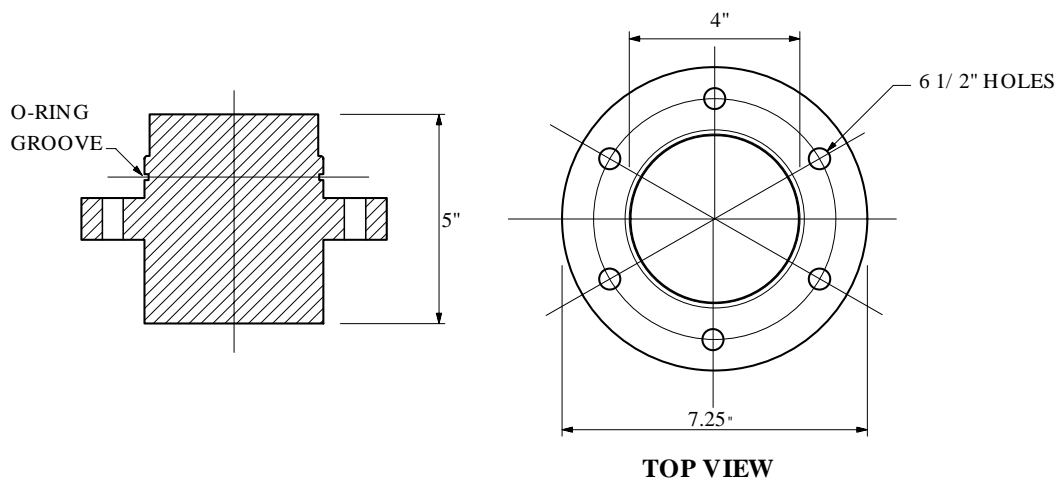


Figure 2.2 Pedestal

2.4.2 Vessel

Made of high-strength steel, the vessel is a hollow cylinder with an outside diameter of 7.25 inches (184 mm) and an inside diameter of 4.25 inches (108 mm). The diameter was enlarged to 5.25 inches (133 mm) at the top to provide a reservoir for the molten metal alloy at the time of testing. It is 11.75-inches (298 mm) tall. There are six 1½-inch (38-mm)-deep bolt holes with a diameter of ½ inch (12.7 mm) on top and bottom of the vessel in order to secure the pedestal and the top cap to the vessel. Close to the top of the vessel, there is a 45-degree, 1/8-inch (3 mm)-diameter hole with a plug at the end of it in order to facilitate vacuum and nitrogen connection to the airtight assembly (Figure 2.3). The inclination of the hole facilitates the drainage of Wood's metal into the reservoir should the molten metal freeze due to a premature drop in temperature or some other problem occur while the experiment is in progress. This prevents clogging.

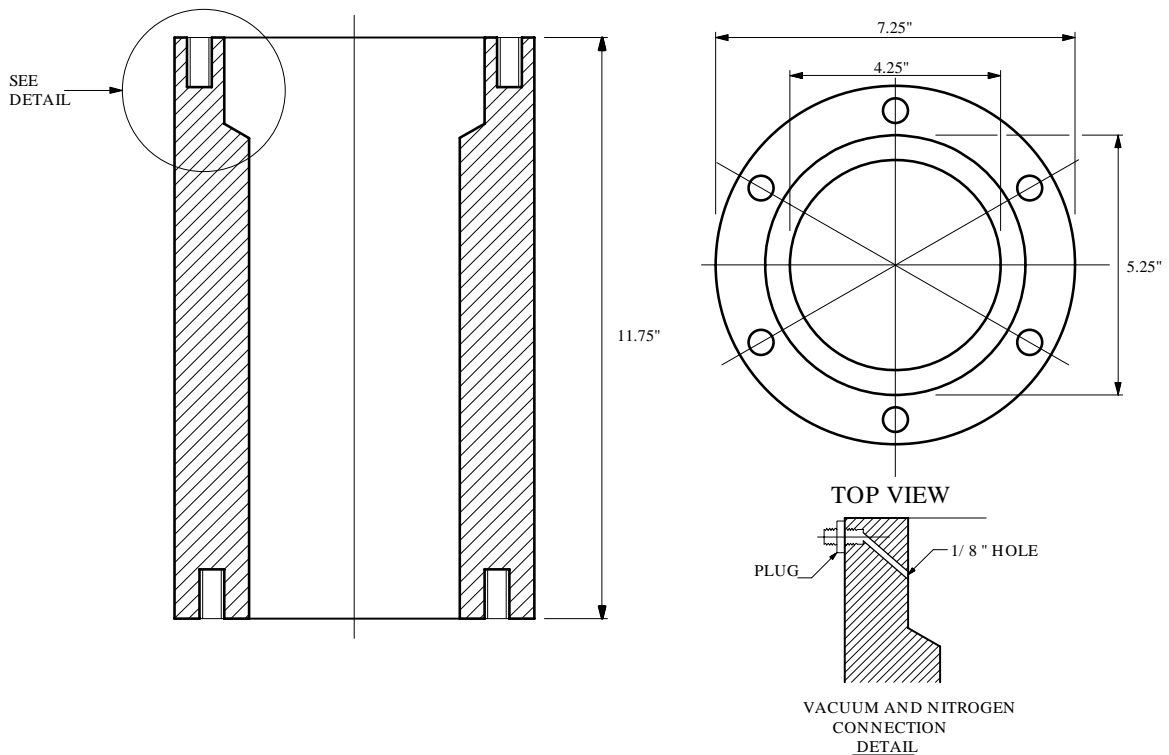


Figure 2.3 Vessel

2.4.3 Piston

Made of high-strength steel, the piston is a 4-inch (102 mm)-diameter, 5-inch (127 mm)-tall solid cylinder which is placed on top of the concrete specimen and

surrounded by the top cap. The piston transfers the applied compressive stresses from the loading machine to the concrete specimen (Figure 2.4).

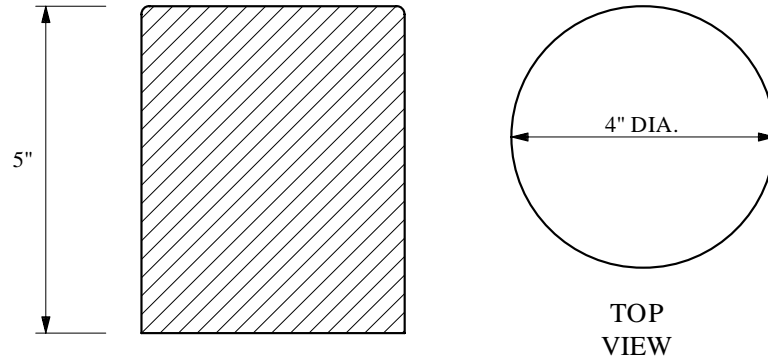


Figure 2.4 Piston

2.4.4 Top Cap

Made of galvanized steel, the top cap is a hollow donut-shaped cylinder with two tiers and an inner radius of 4 inches (102 mm). The top tier is 1-inch (25 mm) thick and has an outer radius of 7.25 inches (184 mm). The bottom tier is $\frac{1}{2}$ -inch (12.7 mm) thick and has an outer radius of 5.25 inches (133 mm). As with the pedestal, there are six equally spaced $\frac{1}{2}$ -inch (12.7 mm) through holes on the upper tier of the top cap to accommodate the bolts which secure it to the vessel. There are also two o-ring grooves on the inner and outer faces of the bottom tier (Figure 2.5).

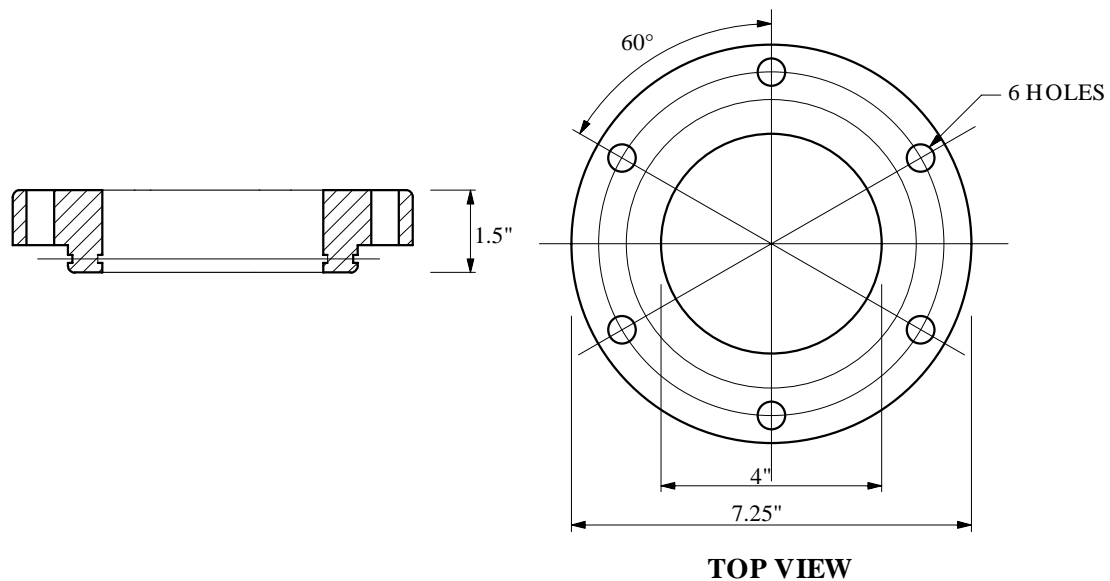


Figure 2.5 Top Cap

Once the entire system is assembled, with the concrete cylinder resting on the pedestal, the top cap closed, and the plug connected to either vacuum or nitrogen, the system is completely airtight.

2.4.5 Heater

The heat was supplied by a ceramic heater operated by a microprocessor-based ramping temperature control unit (Figures 2.11 and 2.13). The ceramic heater was assembled inside two stainless steel half-cylinders with an 18-inch (457 mm) outside diameter and 12-inch (305 mm) inside diameter. The half-cylinders were hinged together on one side and could be made into a monotonic unit by nuts and bolts on the other side of it.

2.5 WOOD'S METAL

Wood's metal, whose commercial name is Cerrosafe[®], is a fusible alloy. In the liquid phase it is nonwetting, with an effective surface tension of about 400 mN/m (Yadev et al. 1984). It consists of 42.5% bismuth (Bi), 37.7% lead (Pb), 11.3% tin (Sn), and 8.5% cadmium (Cd). It has a melting point range from 160°F to 190°F (71.1°C to 87.8°C) below the boiling point of water, and is solid at room temperature. Wood's metal has a Young's modulus of 9.7 GPa and a density of 9.4 g/cm³. The advantage of such an alloy is that it can be injected into voids and stress-induced microcracks at the desired stress level, then solidified at any stage of the experiment to preserve, in three-dimensional form, the geometry of the microcracks induced at any given stage of the experiment. Figure 2.6 shows Wood's metal in solid and molten modes.



Figure 2.6 Wood's Metal

2.6 EXPERIMENTAL PROCEDURE

Two different loading conditions, uniaxial and triaxial, were used to induce cracks in the concrete cylinders. Triaxiality was provided by the wire wound around the concrete cylinders.

After preparation for testing, each concrete cylinder was first dried in an oven at a temperature of 110°F (43.3°C). This removed the moisture in the concrete and preheated the cylinder, ensuring that the molten metal alloy could penetrate into pores and cracks deep within its core without solidifying prematurely. The concrete cylinder was then placed on the pedestal inside the vessel and the piston was placed on top of it. The top cap was left open resting on three wedges a short distance from the top of the vessel so that the molten metal could be poured through the gap using a funnel (Figure 2.10). At this point, a minimum load was applied to the piston to prevent the cylinder from floating after the Wood's metal was poured in. Once the concrete cylinder was submerged in the molten metal the top cap was dropped by removing the wedges and then bolted tightly to the vessel. Figure 2.7 shows a schematic diagram of the test apparatus. To monitor the temperature, a thermocouple was inserted into a predrilled hole on the top cap. The heater was then placed around the assembled system with a special noncombustible board placed on top to prevent heat convection and thus uniform heating of the test assembly (Figure 2.12).

The heat was supplied in three stages. Starting at room temperature, the heat was ramped up to 122°F (50°C) and held at that temperature for 10 minutes. Then the temperature was ramped up to 167°F (75°C) and held there for an additional 10 minutes. The final stage involved ramping the temperature up to a target of 205°F (96°C) for a period of 15 minutes and holding it at that temperature until the heat was no longer needed. Figure 2.8 shows the heating scheme diagram.

When the test assembly was thus heated, Wood's metal was poured into the vessel to a level above the top end of the concrete cylinder to form a metal reservoir with the concrete cylinder totally submerged inside. The top cap was then immediately closed and the thermocouple reinserted to the side of the top cap. A LVDT (linear variable displacement transducer) for the axial displacement measurement was attached to the loading frame. The ceramic heater was placed

around the vessel to liquefy the Wood's metal inside and to maintain a constant temperature throughout the experiment. This temperature was, in turn, monitored by a thermocouple that was attached to the side of the top cap. Figure 2.9 shows a schematic setup for the testing.

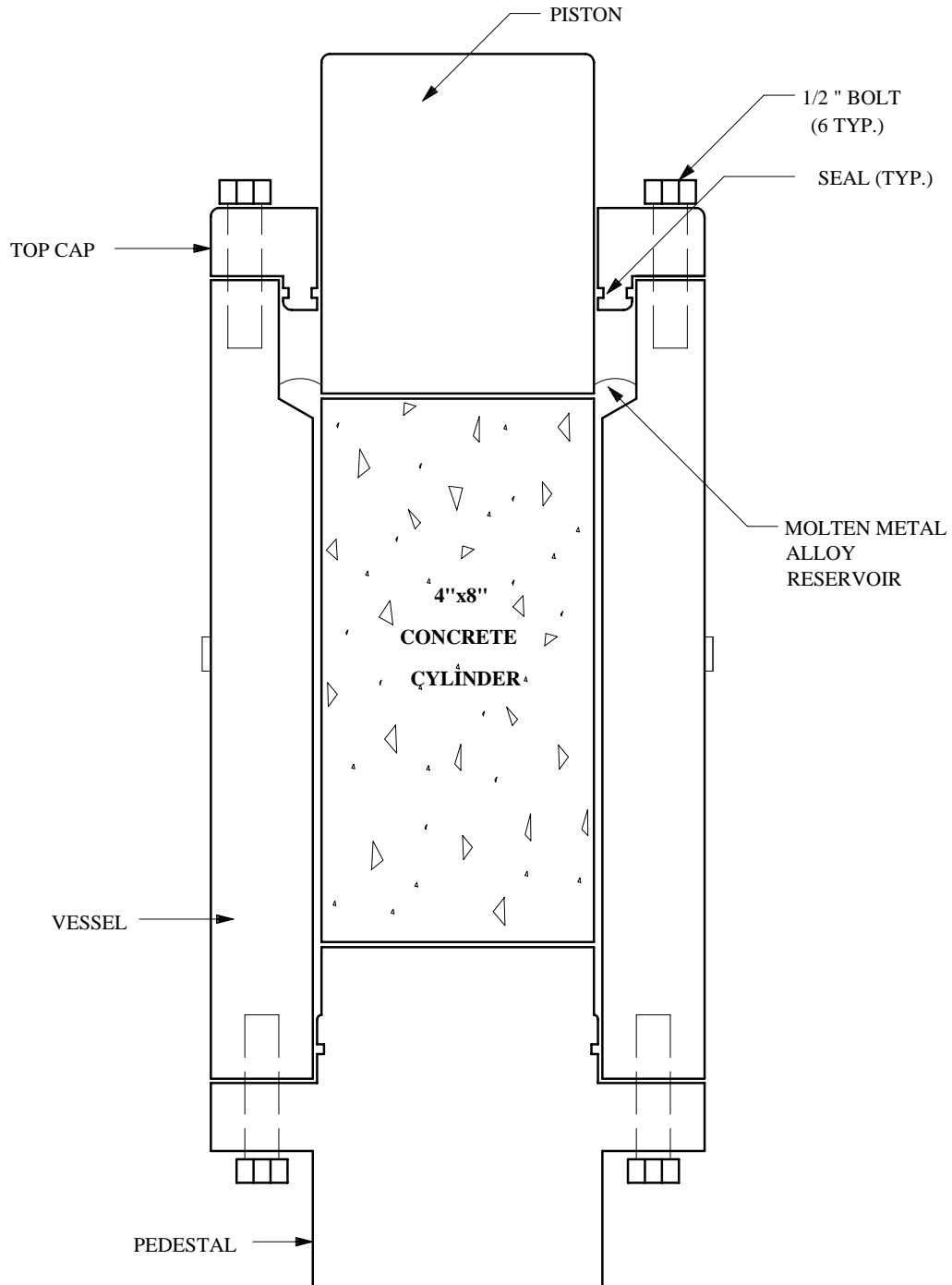


Figure 2.7 Diagram of the test apparatus

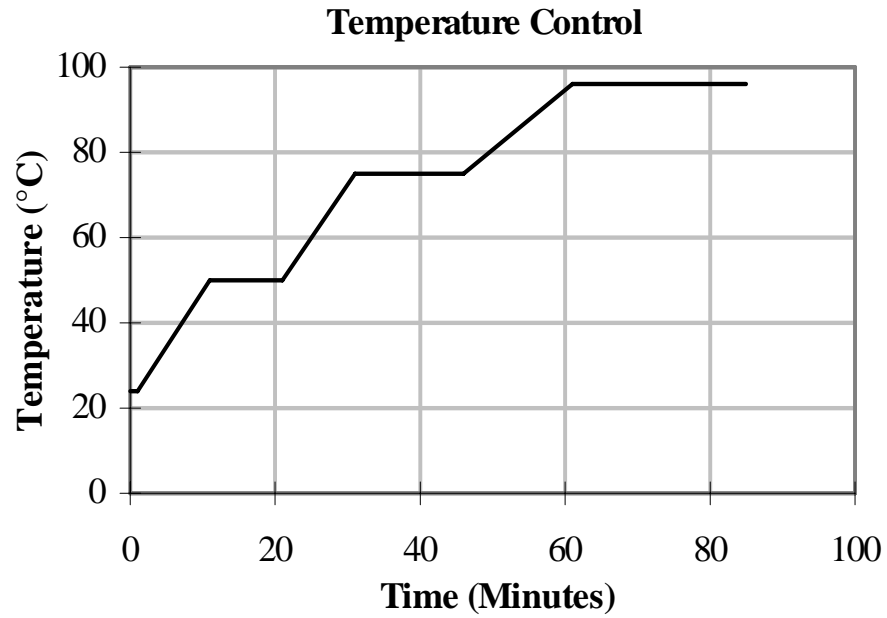


Figure 2.8 Heating scheme diagram

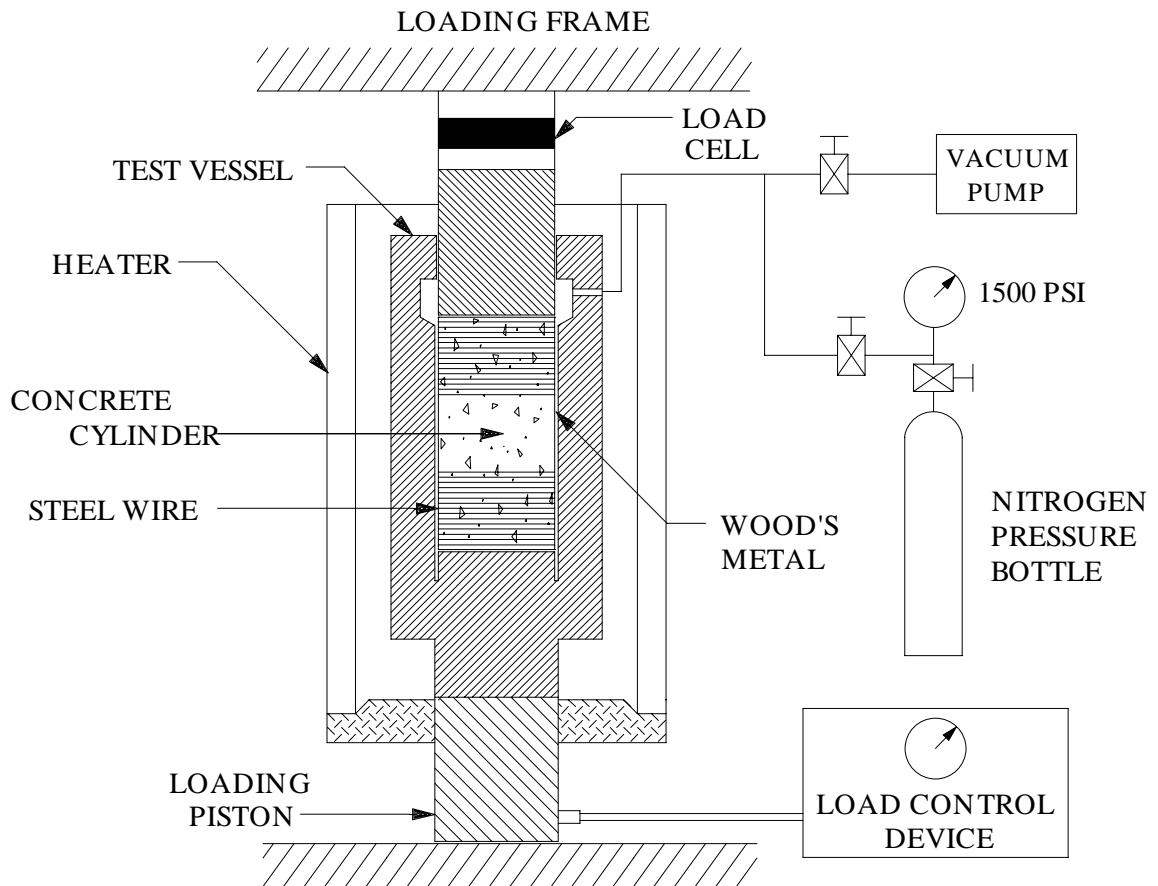


Figure 2.9 Schematic diagram of the test assembly

With the internal temperature thus established and maintained at 96°C (205°F), a vacuum was applied to the vessel and kept constant for at least 30 minutes. The vacuum removed any air that had become trapped in the concrete cylinder when it was assembled inside the vessel. An axial stress of up to 90% of the ultimate strength was applied to the concrete cylinder, at which point the vacuum was removed.

Finally, in order to saturate the induced microcracks with the molten metal, nitrogen pressure was applied to the top of the vessel. It was controlled by a high-pressure regulator on a bottle of nitrogen (Figure 2.14). A nitrogen pressure of 1500 psi (10.3 MPa) was applied to the molten metal as the pore pressure, which was kept constant throughout the tests and which did not alter the effective stresses on the concrete cylinder. With a surface tension of 400 mN/m, the alloy could penetrate into flat cracks with apertures as fine as 0.08 microns.

Throughout the period of loading and unloading, the axial load and axial displacement were recorded on a data acquisition system and monitored on an X-Y plotter. The axial stress of interest was kept constant for 2 hours to allow the liquid metal to penetrate into pores and fractures. Afterwards, fans were used to cool the vessel down to room temperature and to expedite solidification (Figure 2.15). Approximately 3 hours elapsed between the time pore pressure was applied and the period during which the metal was allowed to solidify. Figures 2.10 through 2.13 illustrate some aspects of the experiments.

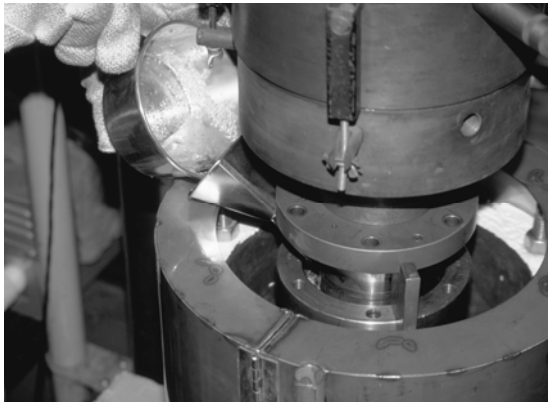


Figure 2.10 Pouring molten metal into the vessel

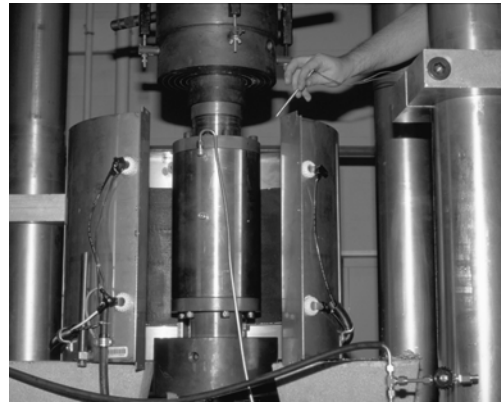


Figure 2.11 Inserting the thermocouple into the top cap

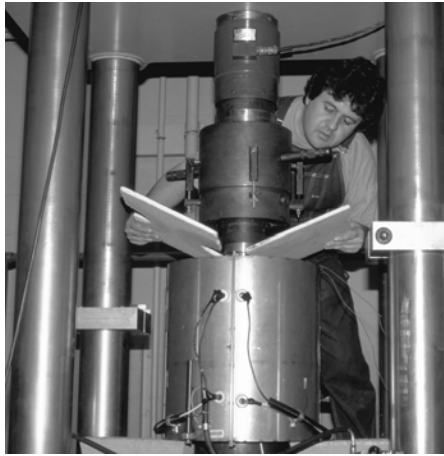


Figure 2.12 Placing the heater and the insulation



Figure 2.13 Temperature and load control devices

A step-by-step explanation of the experimental procedure is outlined below:

1. The hydraulics of the Universal Testing Machine are activated.
2. Piston of cell engages swivel head. Top cap and pedestal bolts are tightened. 100 psi (0.7 MPa) axial load is applied.
3. The head remains unlocked during heating.
4. Feedback thermocouple is positioned in top cap (Figure 2.11).
5. Vacuum line is attached with bleed valve open.
6. M-board is placed in position (Figure 2.12).
7. Heater is activated to 50°C, soak, 75°C, soak, 96°C, soak (Figure 2.13).
8. Vacuum is applied.
9. Heater is operated for 100-120 minutes.
10. Specimen is loaded to 85-90% of f'_c , is held under load control.
11. Vacuum is changed to nitrogen at 1,500 psi (10.3 MPa) (Figure 2.14).
12. Heater is turned off and removed.

13. Fans are turned on (Figure 2.15).
14. Specimen is cooled for at least 70 minutes.
15. Nitrogen pressure is dropped.
16. Specimen is unloaded.
17. Bolts are broken loose from top cap and pedestal.
18. Head of machine is positioned so as not to bang human head.
19. Top cap and piston are removed using T-handle allen wrench.
20. Cell is inverted and pedestal bolts removed. (Caution: nitrogen pressure remains high below sample until o-ring is fully exposed.)
21. Pedestal is removed.
22. Aircraft cable is used to lift cell (Figures 2.17 & 2.18).
23. Spacer is used to elevate cell (Figure 2.16).
24. Head is locked, specimen extruded (Figure 2.19).



Figure 2.14 Nitrogen dispensed through a high pressure regulator

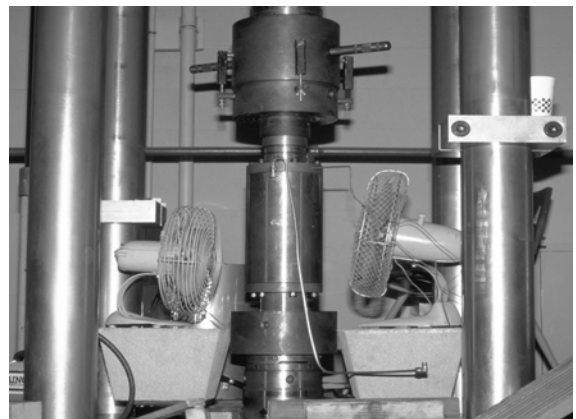


Figure 2.15 Post-experiment cooling of the cell

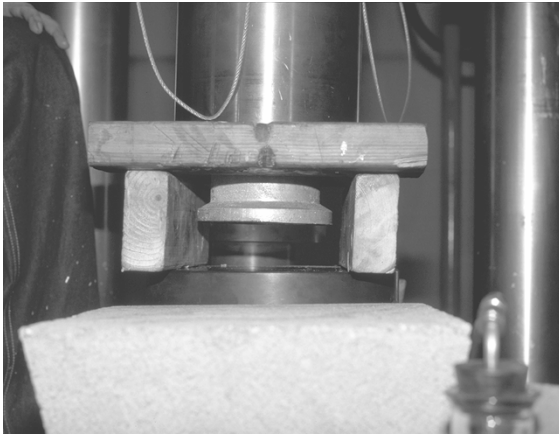


Figure 2.16 Extrusion of concrete specimen

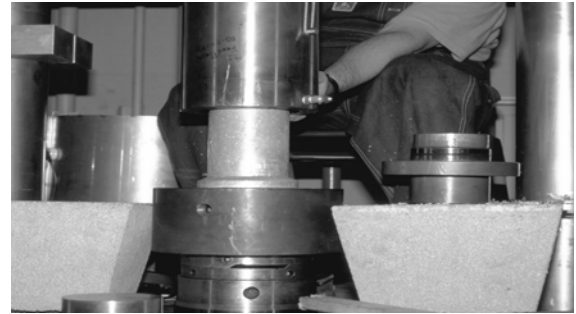


Figure 2.17 Raising the vessel



Figure 2.18 Raising the vessel by aircraft cable

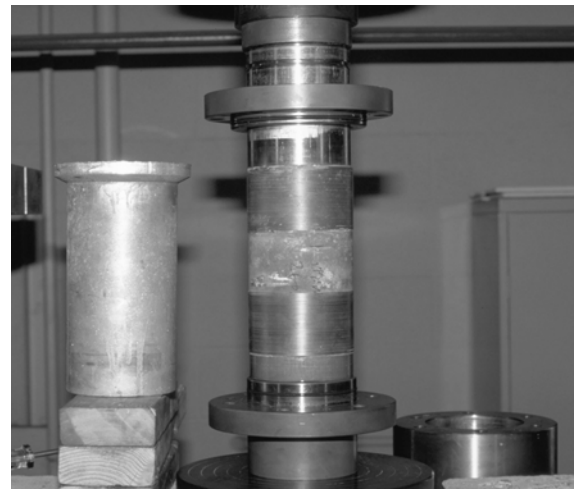


Figure 2.19 Specimen prior to and after Wood's metal injection

2.7 EXPERIMENTS CONDUCTED

A total of eight experiments, five on normal-strength and three on high-strength concrete cylinders, were conducted with conditions as defined in Table 2.3:

Table 2.3 Experiments conducted

Test	LOADING CONDITION	CONCRETE TYPE
Experiment 1	No-load	Normal-Strength
Experiment 2	Uniaxial	Normal-Strength
Experiment 3	Partially Confined	Normal-Strength
Experiment 4	Partially Confined	Normal-Strength
Experiment 5	Fully Confined	Normal-Strength
Experiment 6	No-load	High-strength
Experiment 7	Uniaxial	High-strength
Experiment 8	Partially Confined	High-strength

Complete information on concrete strength, confinement conditions, applied stresses, and drying data on each experiment is provided in Appendix 1.

2.8 SPECIMEN PREPARATION

2.8.1 Cutting

After each experiment, the 8-by-4-inch concrete cylinder was sectioned along its long axis, using oil to cool the cutting saw (Figure 2.20). Then one of the half-cylinders was sectioned at the middle, along its diameter (Figure 2.21). An axial slab, approximately 1/8-inch thick, was sliced parallel to the direction of the load. Two half-circle slabs of similar thickness, one from the top and one from the bottom of the quarter-cylinder, were sliced as well. Figure 2.23 shows a cross section of a concrete cylinder cut along its diameter.



Figure 2.20 Axial cut of concrete cylinder



Figure 2.21 Lateral cut of concrete cylinder

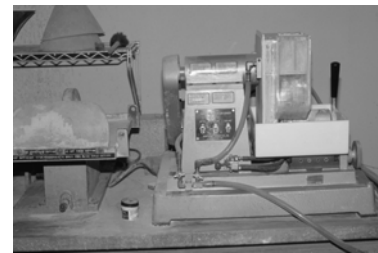


Figure 2.22 Specimen extraction

Four specimens were extracted from the axial slab (specimens 1, 2, 3, and 4). Specimens 5 and 6 were extracted from the top lateral slab, and specimens 7 and 8 were taken from the bottom lateral slab (Figure 2.25). The next step was to polish the specimens for the SEM study.

2.8.2 Polishing

The concrete specimens extracted from the axial and lateral slabs were 1-inch (25 mm) square and had an approximate thickness of 5 mm. First, one side of each specimen was polished with 120#, 220#, 320#, and 600# silicon carbide using a rotating grinder and mounting it against a 1-inch (25.4 mm)-diameter glass plate with epoxy. In order to make both sides of the specimen parallel to each other, the samples were cut 2-3-mm-thick by using a diamond slicing wheel with a nonaqueous lubricant (propylene glycol coolant) (Figure 2.22). The specimens were then lapped (grinding on a flat surface) with a wheel grinder and polished with 600# silicon carbide. Further polishing was performed with 100-, 50-, and 10-micron aluminum powder on a glass plate. The final stage involved treating specimens with 5-, 3-, and 1/4-micron diamond paste using a special polishing equipment (ASTM 1993). After each stage of polishing, the specimens were immersed in acetone and placed in an ultrasonic machine in order to remove the residual silica film on their surfaces, thus preparing them for the next stage of polishing.



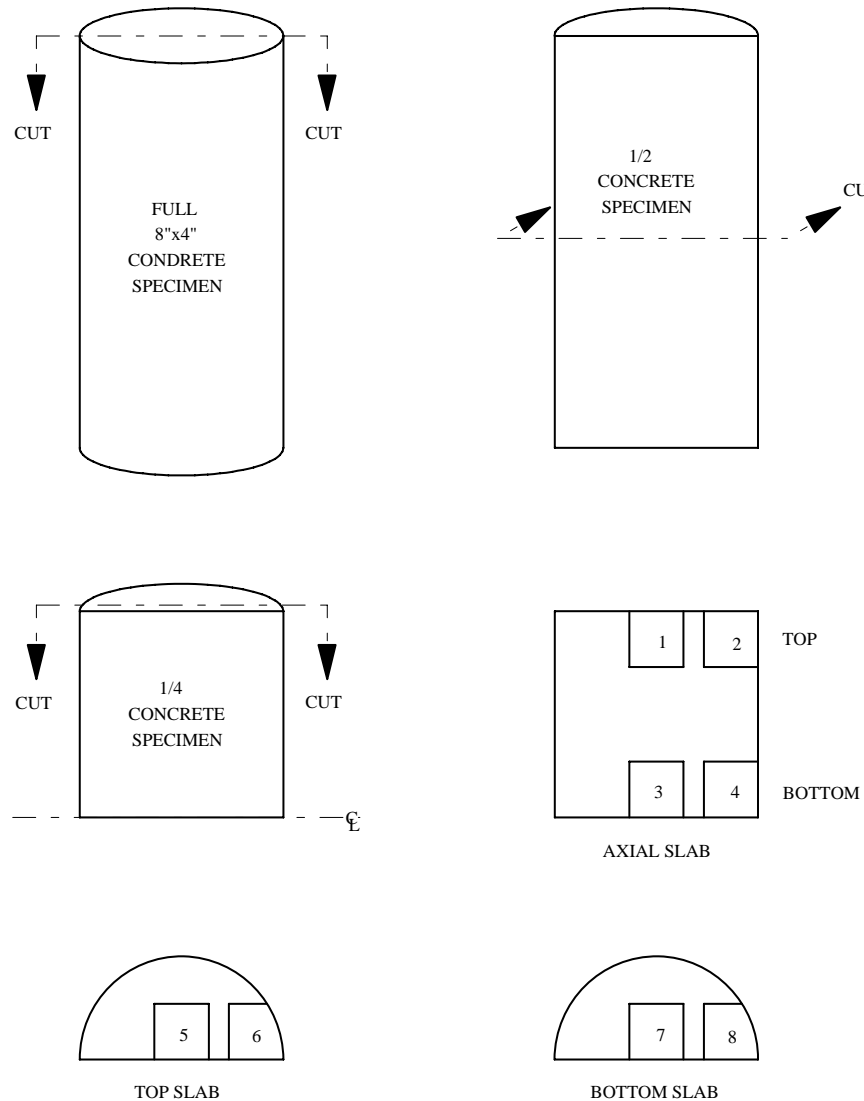
Figure 2.23 A lateral section showing macrocracks filled with metal alloy



Figure 2.24 Specimen placed on glass plate and aluminum base for SEM study

2.8.3 Specimen Identification

All the experiments conducted are identified by a number; for example, Experiment 5 is the triaxial-compression test on a normal-strength concrete cylinder, with continuous wire confinement over the entire length of the cylinder at a pitch of 20 threads per inch. The specimens are identified by two sets of numbers. The first number refers to the experiment number, i.e., 1 through 8, and the second number indicates the specimen location shown in Figure 2.25.



SPECIMEN NUMBERING SCHEME
FIRST NUMBER: EXPERIMENT NUMBER
SECOND NUMBER: SPECIMEN LOCATION

Figure 2.25 Specimen extraction and numbering scheme

2.8.4 Preparation for Scanning Electron Microscope (SEM) Analysis

After all the specimens were thus prepared, and prior to observation by SEM, they were gold coated. The single most important reason for coating or increasing the bulk conductivity is to increase the electrical conductivity of the sample. Materials of high resistivity, such as concrete, charge rapidly under the incident beam and might develop a potential sufficient to cause a dielectric breakdown in regions of the specimen. This could lead to variations in the surface potentials, giving rise to the complex and dynamic image artifacts commonly referred to as *charging*. A suitable conducting path may be established with a thin coating layer of gold which eliminates the problems associated with charging (Goldstein et al. 1992). Once the gold coat is in place, the specimen is then ready to be put into the scanning electron microscope (SEM).

Chapter 3

SCANNING ELECTRON MICROSCOPY, IMAGE ANALYZER, AND STEREOLOGY

3.1 INTRODUCTION

The microscope has been a powerful tool in the study of cement and concrete since the early development of these materials. Le Chatelier (1882) was amongst the first to apply the microscope to the study of cementitious materials. He used it to investigate the chemical and physical aspects of hydration and setting, rather than to study cracks. His efforts undoubtedly influenced later workers in their use of the microscope. Tavasci (1942) successfully used the microscope to study the composition and structure of concrete, but not for cracks per se. His work, however, set the stage for the studies of cracks on the interior surfaces of cut specimens which were conducted in the 1960s.

The electron microscope was apparently first used by Eitel (1941, 1942), and by Radczewski and his co-workers (1939) to study the hydration process of concrete. Grudemo (1960) was another important pioneer in the use of high magnification, including the use of the electron microscope. Although most of these studies were not directly related to cracks, they led the way to later studies of cracks in which electron microscopy was a powerful tool. Diamond and Mindess (1980) used the scanning electron microscope to observe the growth of surface cracks during loading, using magnifications generally from 35X to 450X.

3.2 SCANNING ELECTRON MICROSCOPY

The scanning electron microscope (SEM) is one of the most versatile instruments available for the examination and analysis of the microstructural characteristics of solid objects. The primary reason for the SEM's usefulness is the high resolution that can be obtained when bulk objects are examined; values on the order of 2 to 5 nm (20-50 Å) are now usually quoted for commercial

instruments, while advanced research instruments are available that have achieved resolutions of better than 1 nm (10\AA).

The basic components of the SEM are the lens system, electron gun, electron collector, visual and recording cathode ray tubes (CRTs), and the electronics associated with them. In the SEM, a fine electron probe is produced which rapidly scans (rasters) across the area of interest. The signals generated in the latter case are detected and converted to CRT electronic signals, which are then fed to a cathode ray tube (CRT). The CRT and the scanning coils are linked through the same scan generator, so that the image appearing on the CRT corresponds spatially to the area of the sample scanned.

The interaction of the electron beam with the specimen produces a variety of signals that are used for imaging and spectroscopy. These signals are not generated at a point, but rather within a volume known as the *interaction volume*.

The incident (primary) electrons lose energy as they penetrate the sample, giving rise to an X-ray continuum, which consists of all possible wavelengths corresponding to the range of energies of the incident beam. The high-energy primary electrons may penetrate some distance into the sample before being scattered outside of the sample again by the Coulombic repulsion of the electron clouds in the solid. It has been experimentally determined that a significant fraction of the incident electrons that strike a flat, bulk target placed normal to the probe subsequently escape through the same surface that they entered. The re-emergent beam electrons are called *backscattered electrons* (BSE). The strength of the scattering will depend on the atomic number of the scattering atom, so that backscattered electron images exhibit *atomic number contrast*. Backscattered electrons provide an extremely useful signal for imaging in scanning electron microscopy. Backscattered electrons respond to composition (atomic number or compositional contrast), crystallography (electron channeling), and internal magnetic fields (magnetic contrast). Note that these backscattered electrons may be generated at greater depths than that indicated, in which case they may not possess enough energy to escape the sample. The primary or backscattered electrons may knock electrons out of the conduction band of the solid. These *secondary* electrons are relatively low in energy, and so can only escape from a

region near the surface of the sample. This signal is thus often used for generating topographic information.

The electron probe and the CRT are linked through the same scan generator, so that both sample and screen are scanned in the same X-Y grid pattern. The intensity of the signal reaching the detector from a given point on the sample is used to adjust the brightness of the CRT at the corresponding point. The result is the construction of a map of the sample. Figure 3.1 shows a scanning electron microscope and an image analyzer.



Figure 3.1 Scanning electron microscope (SEM) and Kontron Image Analyzer

3.3 IMAGE ANALYZER

The backscatter electron images obtained from scanning electron microscopy were analyzed on *Kontron Elektronik GmbH Image Analysis Division, IBAS "Interaktives Bild-Analysen System" (Interactive Image Analysis System)*. Computer programs were developed to analyze the images based on the concept of stereology which is covered in detail later on in this chapter, and also based on two dimensional measurements of the crack network represented by Wood's

metal. The computer program for stereological analysis obtains fifteen parameters from each image. The area of the image that Kontron analyzes is a square with the dimensions 512×512 pixels, each pixel corresponding to 3.2890 microns. The program creates a histogram for each image and establishes a threshold in the histogram, in order to identify the Wood's metal. It then scraps the noncontinuous short objects, lines, and dots out of the image. Its next step is to thin the features in the scraped image to create a binary image. The binary image is then intersected by an array of straight parallel lines at various angles, in this case at angles of 0° , 15° , 30° , 45° , 60° , 75° , 90° , 105° , 120° , 135° , 150° , and 165° . The number of crack intercepts at a given angle is measured according to the number of intersections on line array at that angle with the features in the binary image.

$$\text{Number of Crack Intercepts}(\theta) = \text{FIELD COUNT}$$

The program also calculates the total area of the features in the binary image. Since the area of each image is known, the percent of the area that is cracked (or, the crack density) can be determined. For each parameter in the computer program, two values were calculated: the first relates to the final binary image from the original image, and the second relates to the smoothed version of the cracks. Figure 3.2 is a flow chart summarizing the computer program for stereological analysis. The computer programs are presented in Appendix 2.

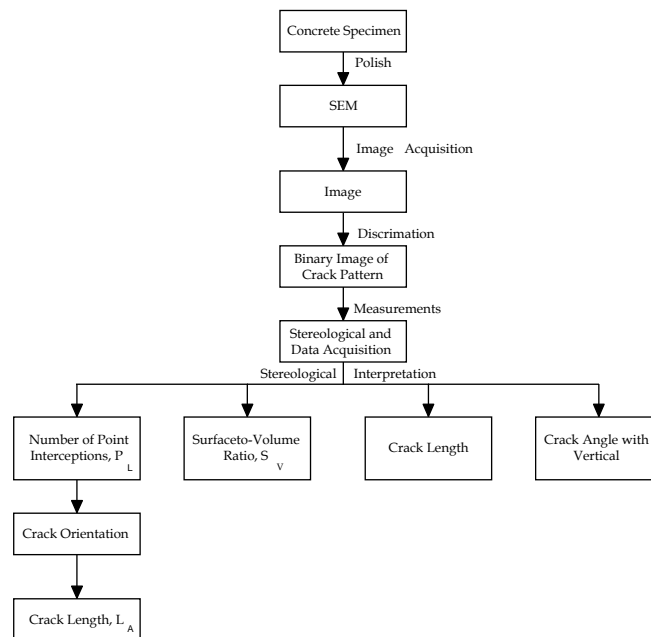


Figure 3.2 Flow chart for stereological steps

3.4 STEREOLOGY AND CONCRETE

3.4.1 INTRODUCTION

All matter can be described in terms of zero, one, two, and three dimensions. Stereology deals with the interpretation of three-dimensional structures by means of their two-dimensional sections. Stereology is the opposite of photogrammetry, which utilizes three-dimensional images in order to construct flat maps. Techniques conventionally used for studying the three-dimensional structure of materials, particularly in other material sciences, are often stereological ones.

If a sectioning plane cuts a three-dimensional aggregate of space-filling polyhedrons, a two-dimensional structure that consists of area-filling polygons can be observed. The task then is to relate the observations made on a section to the true three-dimensional microstructure. Stereology attempts to characterize numerically the geometrical aspects of those features of the microstructure of interest; for example, the microcracks in concrete represented by Wood's metal. In its broadest context, stereology includes not only the quantitative study and characterization of any spatial structure, but also its qualitative interpretation.

There are various approaches to stereological problems. The statistico-geometrical approach depends on measuring and classifying a large number of two-dimensional images and is the method utilized in this study. It is applicable when objects are randomly distributed in space. In such cases, a single section, if extensive enough to contain a statistically significant number of features, may suffice to obtain valid results.

In this study, we deal with the numerical or quantitative characterization of points, lines, surfaces, and volumes. Fundamental expressions have been determined which relate measurements on two-dimensional sections to the three-dimensional structure.

3.4.2 BASIC MEASUREMENTS

Table 3.1 presents some of the basic symbols commonly used in the measurements employing quantitative stereology.

Table 3.1 List of basic stereological symbols and their definition

Symbol	Dimensions	Definition
P		Number of point elements, or test points
P_L	μm^{-1}	Number of intersections of cracks in a section with a superimposed system of equally spaced test array of straight parallel lines per unit of line length
$P_L(\theta)$	μm^{-1}	Number of intersection of cracks in a section with a system of equally spaced test array of straight parallel lines positioned in such a way that it successively encloses an angle θ , $\theta=\pi/2$ and $\theta=0$, respectively, with the axis of symmetry
L	μm	Length of lineal elements, or test line length
L_A	$\mu\text{m}/\mu\text{m}^2$	Total crack length in a section per unit of area
A	μm^2	Planar area of intercepted features, or test area
A_A	$\mu\text{m}^2/\mu\text{m}^2$	Area fraction. Area of intercepted features per unit test area
S	μm^2	Surface or interface area (not necessarily planar)
S_V	$\mu\text{m}^2/\mu\text{m}^3$	Total crack surface area per unit of volume $\left(\frac{S}{V_T}\right)$
N_A	μm^{-2}	Number of cracks in a section per unit of area
V_T	μm^3	Volume of three-dimensional features, or test volume

In this research, the stereological parameters of P_L , L_A , and S_V will be used to perform the stereological analysis. The derivation of the relationships between L_A and S_V with P_L is presented below (Underwood 1968).

3.4.2.1 Number of Point Intersections, P_L

A linear test array is applied randomly to the microstructure in the section plane. P_L is the number of points (intersections) generated per unit length of test lines.

3.4.2.2 Surface-to-Volume Ratio, S_v

The aim of this method is to obtain the surface-to-volume ratio of a system of surfaces in a volume. The basic equation for obtaining the area of surfaces in a volume is

$$S_v = 2P_L \quad \mu\text{m}^2 / \mu\text{m}^3 \quad (3.1)$$

which was derived by Salitikov (1945) and later by Smith and Guttman (1953).

Equation 3.1 applies to a system of surfaces with any configuration. It is as valid for systems of interconnected surfaces as for systems of discontinuous, separated, or bounded surfaces.

In order to derive Equation 3.1, let us consider a test cube of edge length l and volume $V_T = l^3$ enclosing a system of surfaces oriented randomly throughout the cube. The surfaces may be planar or curved, continuous or interrupted, isolated or connected, as represented in Figure 3.3. A set of N vertical test lines of total length $L_T = Nl$ is passed randomly through the cube, cutting horizontal planes through the cube with density N/l^3 .

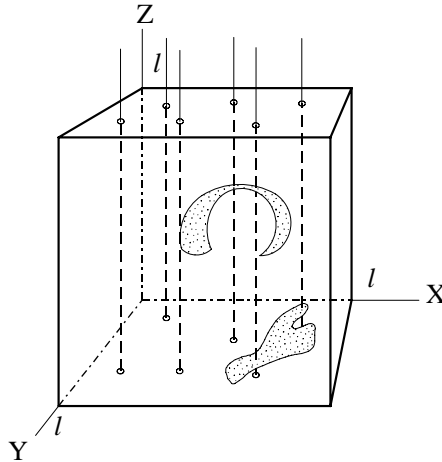


Figure 3.3 Model of deriving the relationship $S_v = 2P_L$. This cube contains random surfaces cut by random vertical test lines (Underwood 1968)

The total surface S is divided into n elementary units of surface area δS so that $S = n\delta S$. The normals to each elementary area form angle θ_i to the vertical test lines, and the areas of the projections of the elementary areas on a horizontal plane, equal $\delta S \cos \theta_i$. Thus the fraction of test lines intersecting the elementary areas is $\delta S \cos \theta_i / l^2$.

An expression is set for the density of intersections of the test lines with the elementary areas, then the individual contributions are added to obtain the total number of intersections with the total surface area. If P_i is the number of intersections associated with each elementary area, then the expected value of the total number of intersections with the entire surface is

$$E(P) = \sum^n P_i = N \sum^n \frac{\delta S \cos \theta_i}{l^2} = \frac{N \delta S}{l^2} \sum^n \cos \theta_i \quad (3.2)$$

Since the elementary units of surface are oriented randomly, every value of θ_i has equal likelihood and $\left(\frac{1}{n}\right) \sum^n \cos \theta_i$ equals the average value, $\overline{\cos \theta}$. Making appropriate substitutions in Equation 3.2 yields:

$$E(P) = \left(\frac{N}{l^2}\right) (\delta S n) \overline{\cos \theta} \quad (3.3)$$

Since $n \delta S = S$, and $\frac{N}{l^2} = \frac{Nl}{l^3} = \frac{L_T}{V_T}$, where L_T is the total length of test arrays, Equation 3.3 can be rewritten as:

$$E(P) = \left(\frac{L_T}{V_T}\right) S \overline{\cos \theta} \quad (3.4)$$

where $E(P)$ is the expected value of the total number of intersections of the test lines with the system of surfaces.

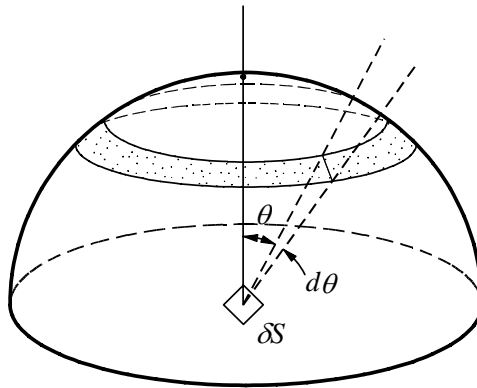


Figure 3.4 Geometry involved in the determination of the probability that random normals lie between θ and $\theta + d\theta$ (Underwood 1968)

The evaluation of $\overline{\cos \theta}$ can be visualized by means of the hemisphere depicted in Figure 3.4. The probability that normals lie between θ and $\theta + d\theta$ is expressed by

$$P(\theta)d\theta = \frac{\text{area of zone}}{\text{area of hemisphere}} = \frac{2\pi r^2 \sin \theta d\theta}{2\pi r^2} = \sin \theta d\theta$$

and average value of $\cos \theta$ is

$$\overline{\cos \theta} = \int_0^{\pi/2} P(\theta) \cos \theta d\theta = \int_0^{\pi/2} \sin \theta \cos \theta d\theta = \left. \frac{\sin^2 \theta}{2} \right|_0^{\pi/2} = \frac{1}{2}$$

Rearrangement of Equation 3.4 gives

$$E(P) = \frac{L_T}{V_T} \frac{S}{2} \quad \text{or} \quad \frac{S}{V_T} = \frac{2E(P)}{L_T}$$

which yields the required relationship, in our notation,

$$S_V = 2P_L \quad \mu\text{m}^2 / \mu\text{m}^3 \quad (3.5)$$

3.4.2.3 Length of Line Per Unit Area, L_A

The equation that relates the length of lineal elements in a plane to their intersection with a test line is

$$L_A = \left(\frac{\pi}{2} \right) P_L \quad \mu\text{m} / \mu\text{m}^2 \quad (3.6)$$

The quantity L_A is a basic microstructural parameter that is useful either as it is or when manipulated into other forms. The derivation of Equation 3.6 is similar to the derivation of Equation 3.1.

Given a randomly oriented system of lines in a plane, let us consider a square test area A_T of edge length l . A set of N vertical test lines of total length $L_T = Nl$ is passed randomly through the test area, cutting horizontal lines through the square with density N/l . The system of lines is divided into n straight elementary segments of length δL and the total line length in the system is

$L = n\delta L$. The elementary segments form angle θ_i to the vertical test lines, and the length of projections of the elementary segments on a horizontal line, are $\delta L \sin \theta_i$. Thus the fraction of test lines intersecting the elementary segments is $\delta L \sin \theta_i / l$.

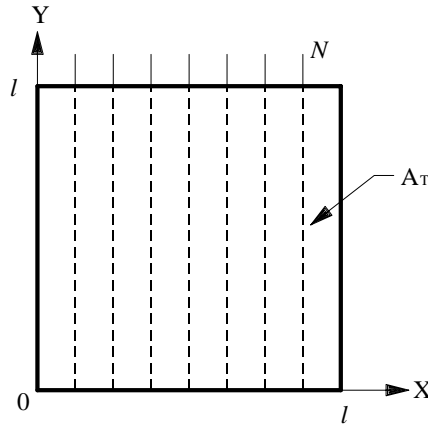


Figure 3.5 Model of deriving the relationship $L_A = \left(\frac{\pi}{2}\right)P_L$

If P_i is the number of intersections of each elementary segment by the test lines, then the expected value of the total number of intersections with the entire system of lines is

$$E(P) = \sum^n P_i = N \sum^n \frac{\delta L \sin \theta_i}{l} = \frac{N\delta L}{l} \sum^n \sin \theta_i \quad (3.7)$$

Since the elementary systems are oriented randomly, each value of the angle θ_i has equal likelihood of existence and $\left(\frac{1}{n}\right) \sum^n \sin \theta_i$ equals the average value $\overline{\sin \theta}$. Making appropriate substitutions in Equation 3.7 yields:

$$E(P) = \frac{N\delta L n}{l} \overline{\sin \theta} \quad (3.8)$$

Since $n\delta L = L$ and $\frac{N}{l} = \frac{Nl}{l^2} = \frac{L_T}{A_T}$, Equation 3.8 can be rewritten as:

$$E(P) = \frac{L_T}{A_T} L \overline{\sin \theta} \quad (3.9)$$

The evaluation of $\overline{\sin \theta}$ can be visualized by means of the circle depicted in Figure 3.6.

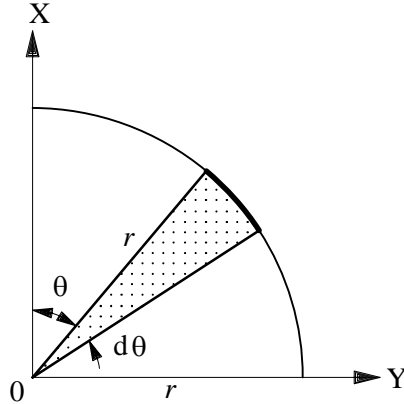


Figure 3.6 Geometry involved in the determination of the probability that elementary segments lie between θ and $\theta + d\theta$

The probability that the elementary segments are oriented between θ and $\theta + d\theta$ is equal to the fraction of the perimeter of a circle that is occupied by this orientation range. From the symmetry involved, only one quadrant of the circle needs to be considered, giving for the probability

$$P(\theta)d\theta = \frac{\text{fraction of perimeter}}{\text{perimeter of circle}} = \frac{rd\theta}{\pi r/2} = \frac{2}{\pi}d\theta$$

Thus the average value of $\sin \theta$ is

$$\overline{\sin \theta} = \int_0^{\pi/2} P(\theta) \sin \theta d\theta = \frac{2}{\pi} \int_0^{\pi/2} \sin \theta d\theta = \frac{2}{\pi}$$

Rearrangement of Equation 3.9 gives

$$\frac{L}{A_T} = \left(\frac{\pi}{2}\right) \frac{E(P)}{L_T} \quad \mu\text{m}/\mu\text{m}^2$$

or, in our notation,

$$L_A = \left(\frac{\pi}{2}\right) P_L \quad \mu\text{m}/\mu\text{m}^2 \quad (3.10)$$

3.4.3 DEGREE OF ORIENTATION

In real structures, the lines in a microsection of a given specimen are usually either isometric or partially oriented. Only in rare cases do we find completely oriented systems of lines. In a partially oriented system of lines in a plane, part of the total length of lines is oriented in a definite direction (or directions). The remaining segments may essentially have a random orientation.

The lines of a partially oriented system of lines in a plane can be divided into elementary straight segments that are very small and of equal length. Some or all of the segments will lie parallel to one or more definite directions (the orientation axes). The remaining segments are assumed to be oriented randomly, or isometrically. From this point of view, a partially oriented system of lines may be regarded as consisting of two superimposed systems of lines: an oriented portion and a random portion.

The length of linear elements in a plane is proportional to the number of intersections made with a test line. Using a test array of straight parallel lines, the number of intersections with an oriented system of lines (such as a crack system) will vary with the direction of the test array. The dependence of the number of intersections per unit length with the angle of the test array can be used to characterize the degree and type of orientation of a system of lines in a plane.

If a test array system of equally spaced, straight parallel lines is superimposed on a sample area, i.e., an image of the crack network in concrete, the number of intersections per unit length of the test line P_L can be determined. Since the value of P_L is a function of the direction of the line system, the specific number of intersections is indicated as $P_L(\theta)$. The *rule of total projections* (Stroeven 1973) states that this value of $P_L(\theta)$ equals the value of the total projected length $L_{A_{Proj}}$ of the lineal features upon a line perpendicular to the test array, or

$$P_L(\theta) = L_{A_{Proj}} \quad (3.11)$$

This type of sampling procedure is called the *method of directed secants on a plane* (Saltikov 1967).

In the case of an isometric (randomly oriented) system, the value of $P_L(\theta)$ is dependent on θ and both sides of equation 3.11 can be averaged with respect to orientation. The result is an important relationship connecting the length of lineal features in a sampling area, L_A , to the specific surface area or to the number of intersections per unit length of the test line, and averaged with respect to the orientation. Therefore,

$$\frac{\pi}{2} P_L = L_A = \frac{\pi}{4} S_V \quad (3.12)$$

Applying the method of random secants on a plane to an image of a crack pattern, Equation 3.12 presents simple algebraic relationships to calculate the total crack length per unit area or the specific surface area (of the cracks) per unit volume. The dependence of the number of intersections per unit length with the angle of the test array can be used to characterize the degree and types of orientation of a system of lines in a plane. Saltikov (1945) proposes a polar plot of P_L with respect to the orientation axis (axes), and calls the resulting curve the *rose of the number of intersections*, or simply the *rose*.

The rose for an oriented system of lines can readily be obtained experimentally by applying a test array to the system of lines at equal angular increments with respect to the orientation axis, and determine P_L separately at each angle. A polar diagram can be made by plotting the radius vectors, P_L , versus θ . The rose diagram is created by connecting the ends of the radius vectors by lines or a smooth curve. In the case of isometry, the rose will be a circle with its center at the origin of the polar figure. If a preference direction should occur in a crack pattern, the shape of the rose will change.

The stress-induced microcrack system in concrete, a composite material, is considered to be a partially oriented as opposed to a completely oriented (idealized) system.

3.4.4 APPLICATION OF STEREOLOGY TO CONCRETE FRACTURE MECHANICS

Stroeven (1973, 1976, 1979, 1991, 1992), Ringot (1988), and Massat et al. (1988) successfully applied the concept of stereology to study micromechanical aspects of concrete. With the advent of modern image analysis systems, it is now

possible to perform stereological analysis on a great number of images accurately and expeditiously, whereas in the past this was not achievable by means of manual methods.

In this section, the application of stereology to the microstructure of concrete will be explained sequentially. After the concrete samples were prepared for scanning electron microscope studies (see Chapter 2), 55 images were extracted from each sample. A total of four samples taken from the center and edge of the concrete cylinders in axial direction were studied (samples 1 through 4 in Figure 2.25). SEM produces a multiphase image from each observation (Figure 3.7).

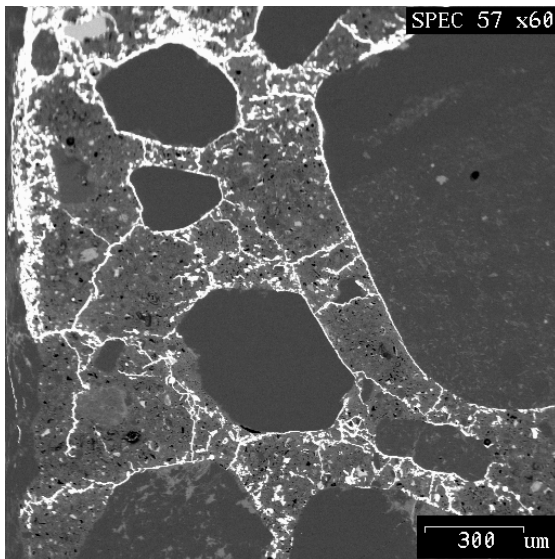


Figure 3.7 A SEM backscatter image

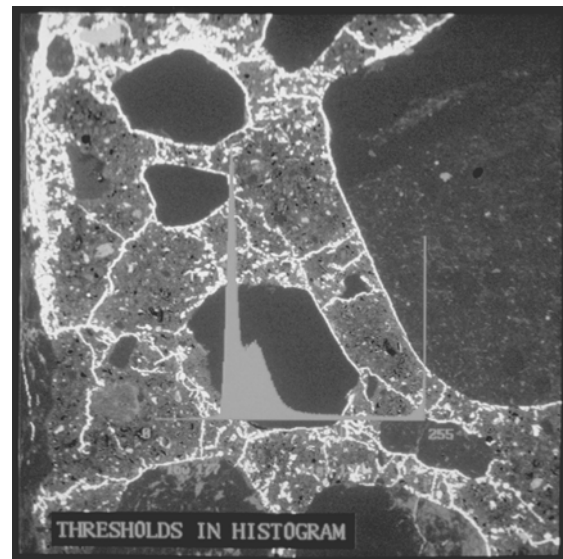


Figure 3.8 Establishing threshold in histogram

In order to recognize and isolate Wood's metal, which is the representative of pores and fractures in concrete, the image analyzer can make a histogram for all of the different phases in the image based on their gray levels, with zero representing the darkest phase and 255 representing the brightest phase (Figure 3.8).

From this histogram, and by means of the trial and error method, two threshold levels can be established to encompass the brightest phase in the

image, namely Wood's metal. The threshold for Wood's metal identification was set between 170 and 255 (Figure 3.9).

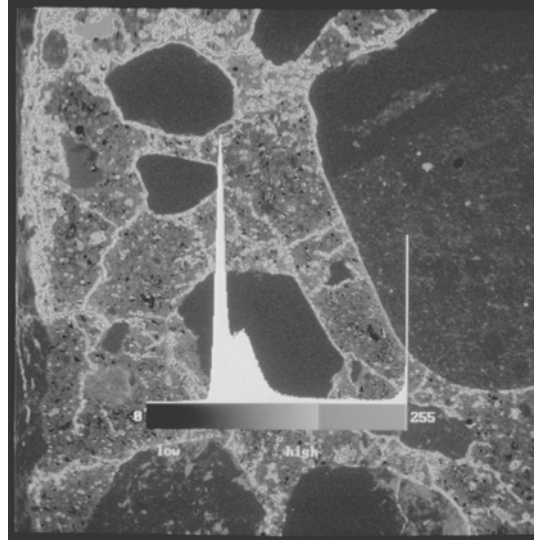


Figure 3.9 Wood's metal identification by establishing threshold levels in histogram

The next step is to eliminate objects from the background that don't fall between these threshold levels (*dis2lev* command). Once the above task is accomplished, what is left in the image is the crack network and pores shown by Wood's metal (Figure 3.10). At this point the aim is to eliminate objects on the basis of their area in pixel units. The lower and upper limits of the objects to be eliminated has to be established to include small pores, small non-continuous cracks, etc. (Figure 3.11).

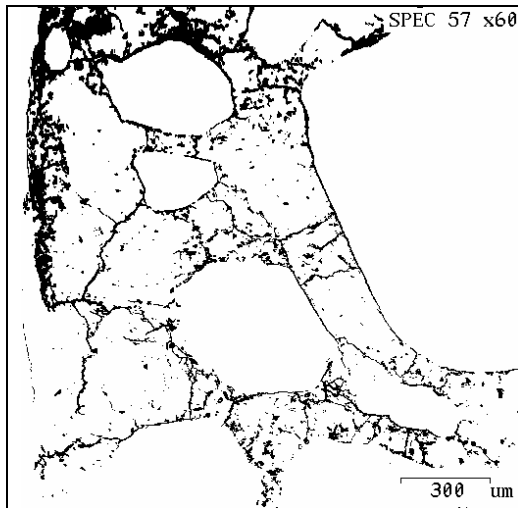


Figure 3.10 Crack network

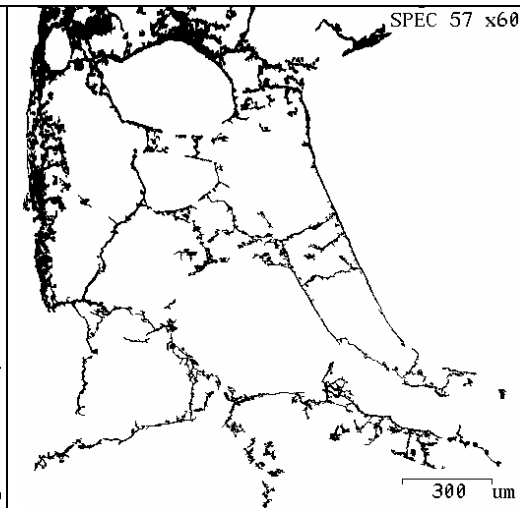


Figure 3.11 Scrap command

The next step is to transform this image into a skeletonized binary image by means of a binary thinning process (invoked by *thinbin* command). For every thinning step, pixels that are not relevant to the connectivity of an object are removed from the object margins, i.e., converted into background pixels. The connectivity of objects is thus maintained. This process can be continued until all objects are reduced to a width of one pixel that approximates the skeletons. Figure 3.12 is the final binary image used for stereological measurements.

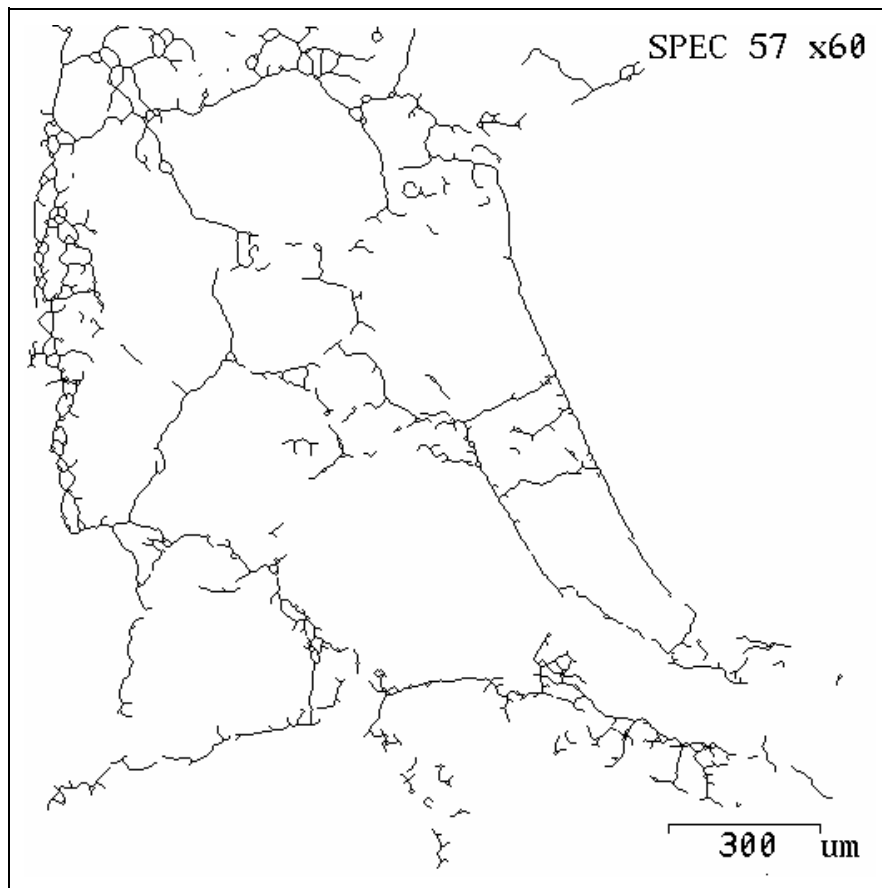


Figure 3.12 Binary-thinned image of the crack network in concrete

The binary image in Figure 3.12 is then intersected by an array of straight parallel lines at 15° angular increments, in this case at angles of 0° , 15° , 30° , 45° , 60° , 75° , 90° , 105° , 120° , 135° , 150° , and 165° (Figure 3.13). The number of crack intercepts at a given angle is measured according to the number of intersections on line array at that angle with the features in the binary image, or crack

network. The number of intersections were determined separately at each angle θ . Then the number of intersections were plotted versus θ , creating the rose of the number of intersections diagram. The rose diagram characterizes the degree of orientation of the cracks, and makes it easier to interpret the data.

$$\text{Number of Crack Intercepts}(\theta) = \text{FIELD COUNT}$$

The rose of the number of intersections diagrams for all the experiments are presented in Chapter 4. It is clear from these diagrams that the cracks are not randomly oriented and that more lie at angles between 0° and 15° and 165° and 180° than in other directions.

The rose diagrams were plotted to cover only the range of 0° to 165° (cracks at 0° and 180° have equal lengths) since the range from 180° to 360° is redundant (Russ 1986). Figure 3.13 depicts the array of straight parallel lines at 0° (or 180°), 15° , and 165° .

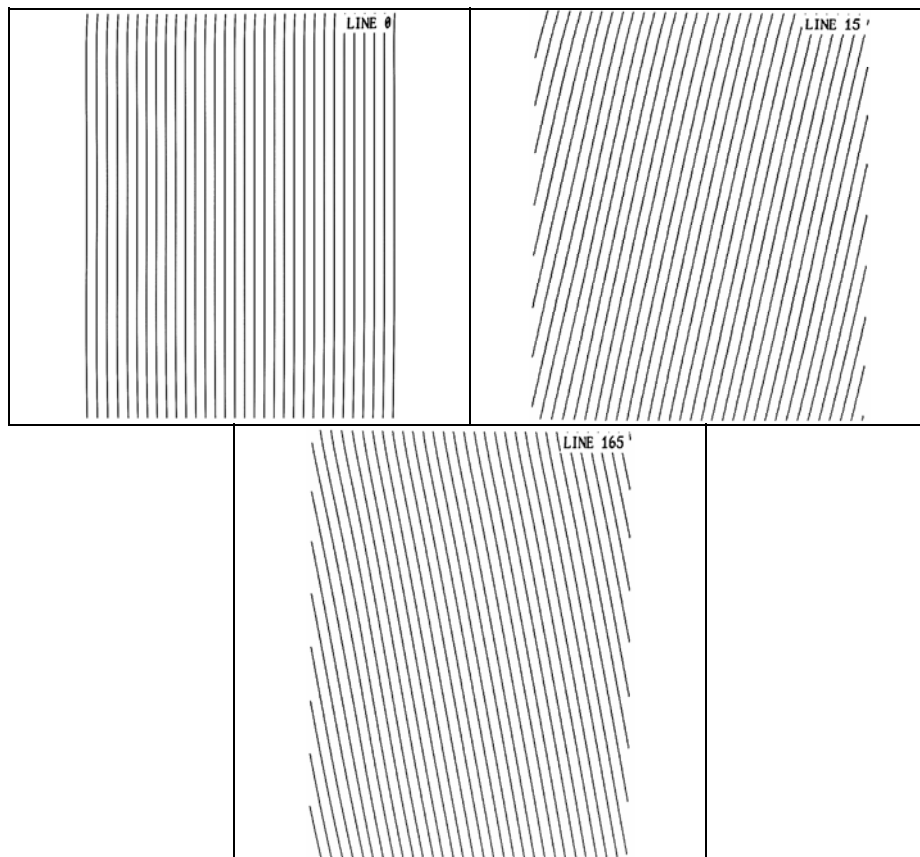


Figure 3.13 Array of straight parallel lines

Chapter 4

OBSERVATION RESULTS AND ANALYSIS OF DATA

4.1 INTRODUCTION

Eight specimens, four parallel and four perpendicular to the direction of maximum applied compressive stresses, were extracted from each experiment as described in Chapter 2. For purposes of analysis, only the specimens parallel to the direction of the maximum compression, i.e. specimens 1, 2, 3, and 4 in Figure 2.25, were examined. A minimum of 55 scanning electron microscope (SEM) images were taken from each specimen, bringing the total number of analyzed images to over 2,220.

Computer programs were developed to analyze the images. These were based both on the concept of stereology as described in Chapter 3, and also on two-dimensional measurements (such as the number of cracks per unit of observed area, crack lengths, and crack orientation) for every image. The computer programs are outlined in Appendix B. The analysis was performed using an image analyzer with the commercial name, Kontron Image Analyzer. The quantitative and qualitative analysis of the data obtained from the image analysis is presented in this chapter.

4.2 CHARACTERIZATION OF MICROCRACK INITIATION

The characterization of the microcrack initiation was studied under the scanning electron microscope (SEM) and on micrographs of cross sections of the specimens for different conditions of confining stresses.

No stress-induced microcracks were observed in the reference specimen, which was subjected to only a small compressive stress when filled with molten metal at a pressure of 1,500 psi (10.3 MPa). Figure 4.1 shows two micrographs from the no-load experiment.

It is important to note that concrete is inherently cracked even before the application of any load (Hsu et al. 1963). Existing pre-load cracks are due to factors such as bleeding, creep, drying shrinkage, etc.

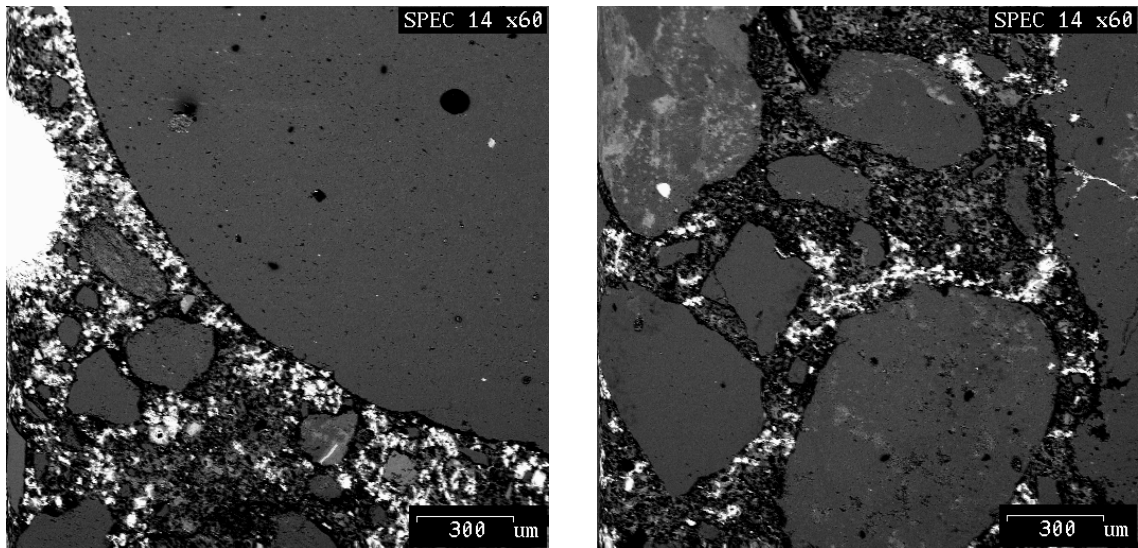


Figure 4.1 SEM micrographs from the no-load experiment

The microcracks in the rest of the specimens appear to have been generated by several different mechanisms. Figure 4.2 shows two micrographs taken from a specimen under confining condition #3; that is, uniaxial compression in the central portion, with ends constrained by pre-tensioned wire, and a pore pressure of 1,500 psi (10.3 MPa). As can be seen, microcracks propagate through the cement paste and along the transition zone.

Many cracks were generated from voids in a mechanism similar to that suggested for rocks by Lajtai (1974), Olson (1974), and Sammis and Ashby (1986). Figure 4.3 shows two micrographs of microcracks generated from a pore space, which is filled with Wood's metal. These microcracks were generated as a result of local tensile stress tangential to the boundary of voids, with a value that was of the order of the maximum applied principal stress. It was found that these cracks usually start from the pore boundaries and then propagate in the direction of maximum compression.

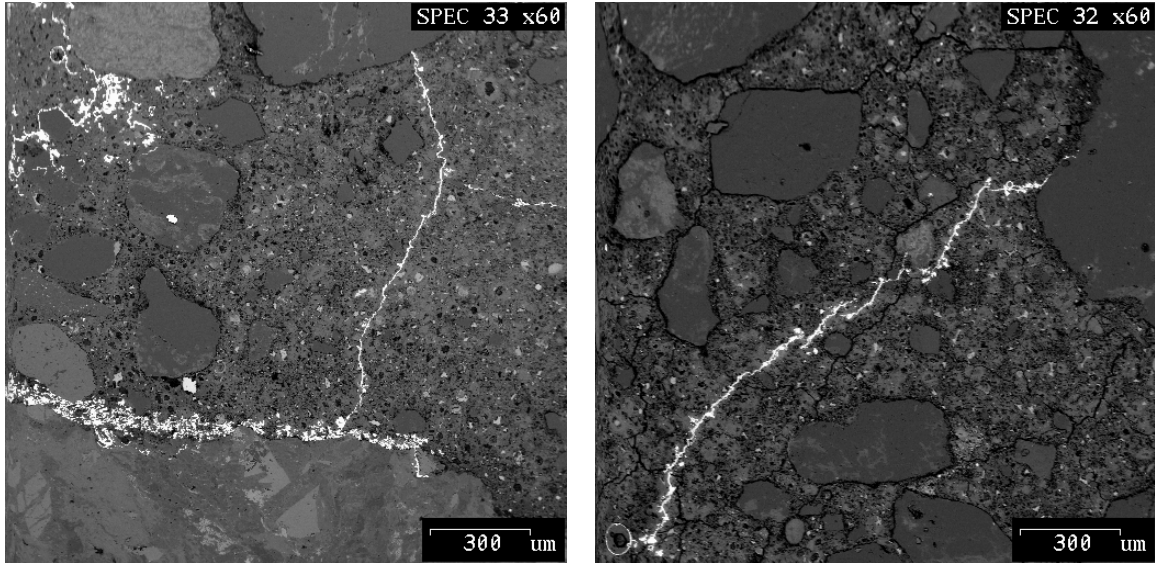


Figure 4.2 SEM micrographs from the partially confined experiment

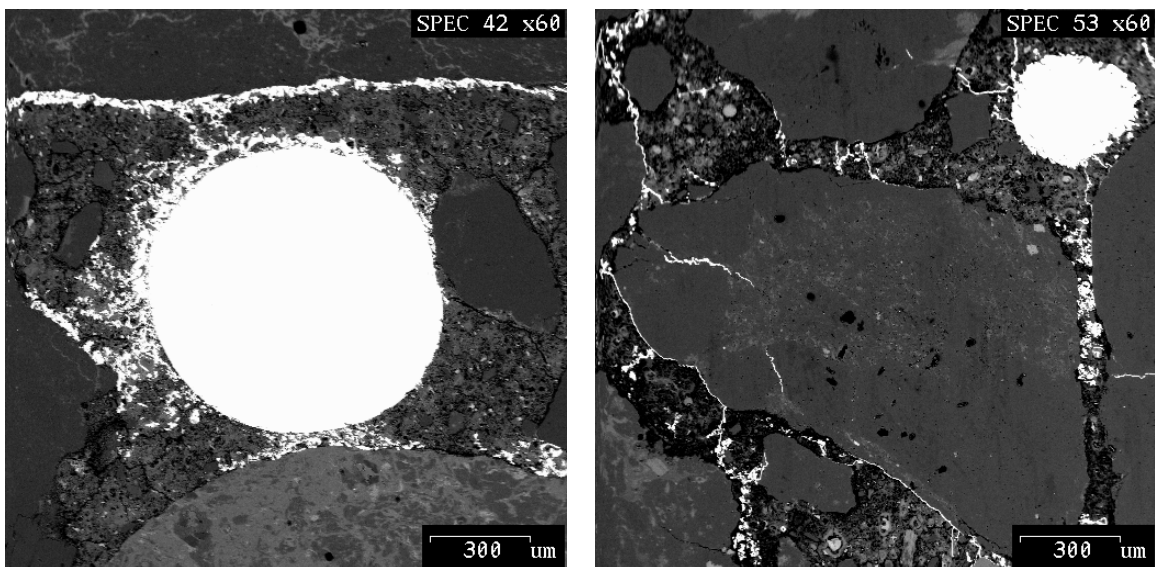


Figure 4.3 SEM micrographs of microcracks propagating from a pore

Microcracks were also found to have been generated from the inside of aggregates, in a manner similar to a Brazilian test, when the aggregates were loaded across their height. Figure 4.4 shows four micrographs of this phenomenon for three different loading conditions- fully confined, partially confined, and uniaxial.

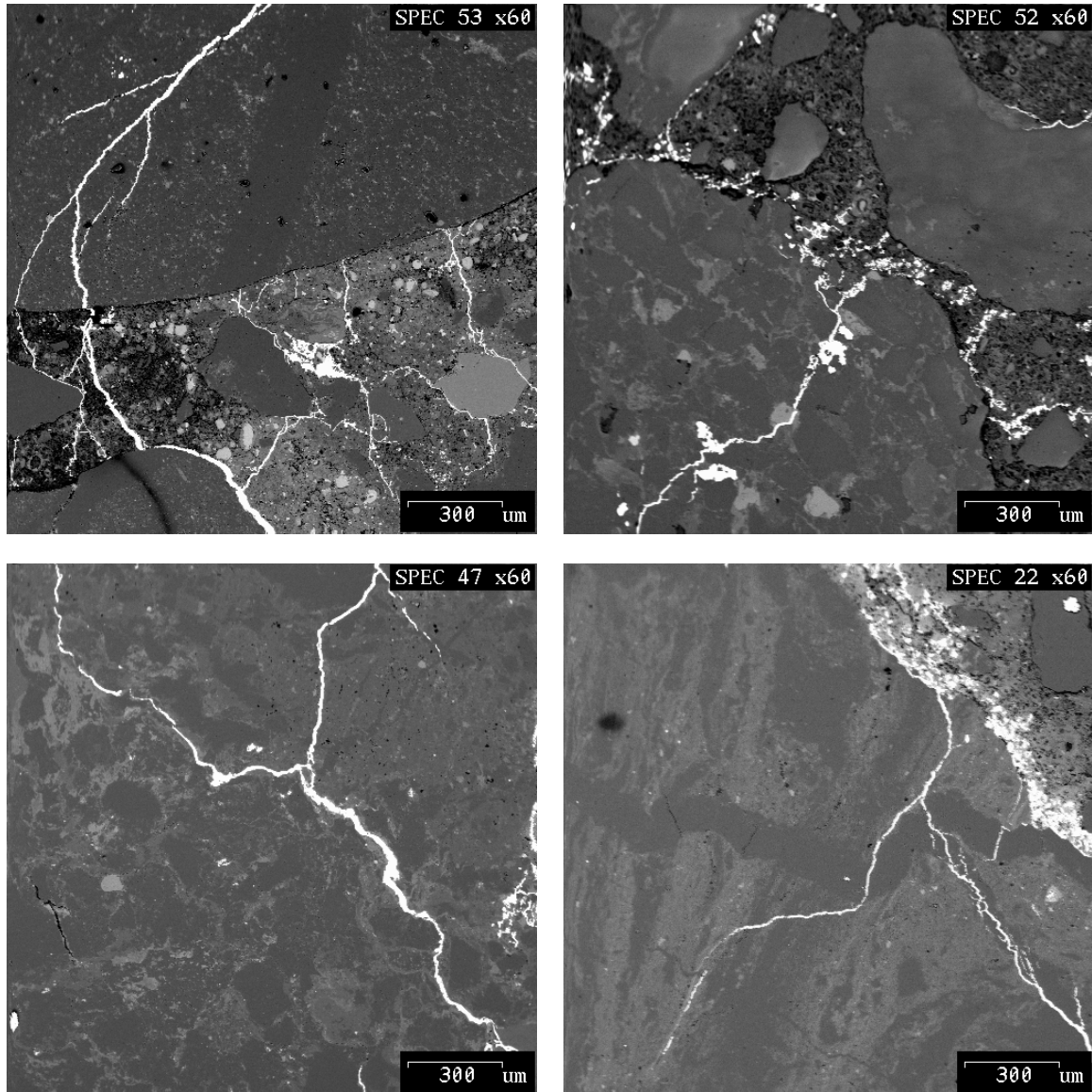


Figure 4.4 SEM micrographs of aggregate cracking

High-strength concrete behaves more like a homogeneous material than does normal-strength concrete. The stress-strain curves for high-stress concrete are steeper and closer to linearity to a high stress-strength ratio than in normal-strength concretes. This is because of a decrease in the amount and extent of microcracking in the transition zone. Thus the high-strength concrete exhibits a more brittle mode of fracture and less volumetric dilation (Carrasquillo et al. 1981). High-strength concrete has a stronger and tougher cement paste due to a

lower water/cement ratio, which results in a closer packing of cement grains and a reduced amount of pores and cracks. Apart from this microstructurally improved matrix, high-strength concrete also has a stronger transition zone- the area of interface between the cement matrix and the aggregates. This presumably results from the reduction of excess bleeding and the filling of gaps by admixtures, which in this case was rice husk ash. The microstructural differences between high-strength and normal-strength concrete cause significant differences in their deformation and fracture behavior. For example, high-strength concrete tends to behave with greater linear elasticity up to its peak strength, while normal-strength concrete typically exhibits non-linear behavior, possibly because of interfacial crack extension prior to peak strength (Carrasquillo et al. 1981; Huang et al. 1989; ACI Committee 363, 1984). Further, fracture development in high-strength concrete is usually accompanied by a relatively small process zone and tends to be characterized better by linear elastic fracture mechanics than does to normal-strength concrete (Gettu et al. 1990).

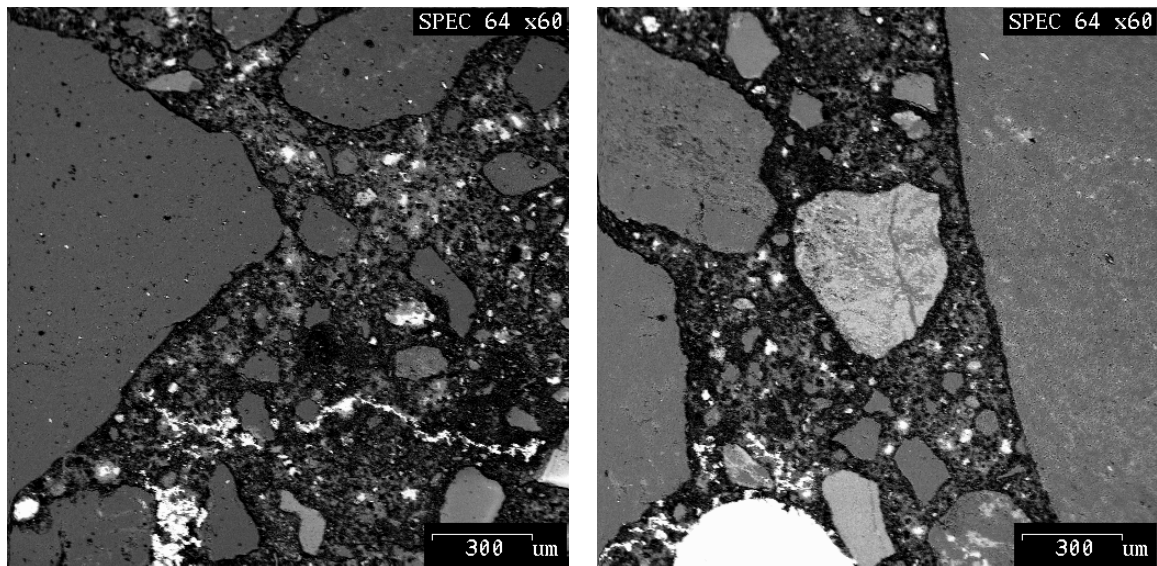


Figure 4.5 SEM micrographs from the no-load experiment for high-strength concrete specimen

Figure 4.5 shows two SEM micrographs from the reference specimen of high-strength concrete, which is a no-load sample. No stress-induced microcracks were observed in the reference specimens. The microcracks observed in these micrographs are attributed to factors such as drying shrinkage.

Figure 4.6 shows four SEM micrographs of a high-strength concrete specimen from Experiment #7, which was conducted under uniaxial loading condition—that is, uniaxial compression with no confinement and a pore pressure of 1,500 psi (10.3 MPa).

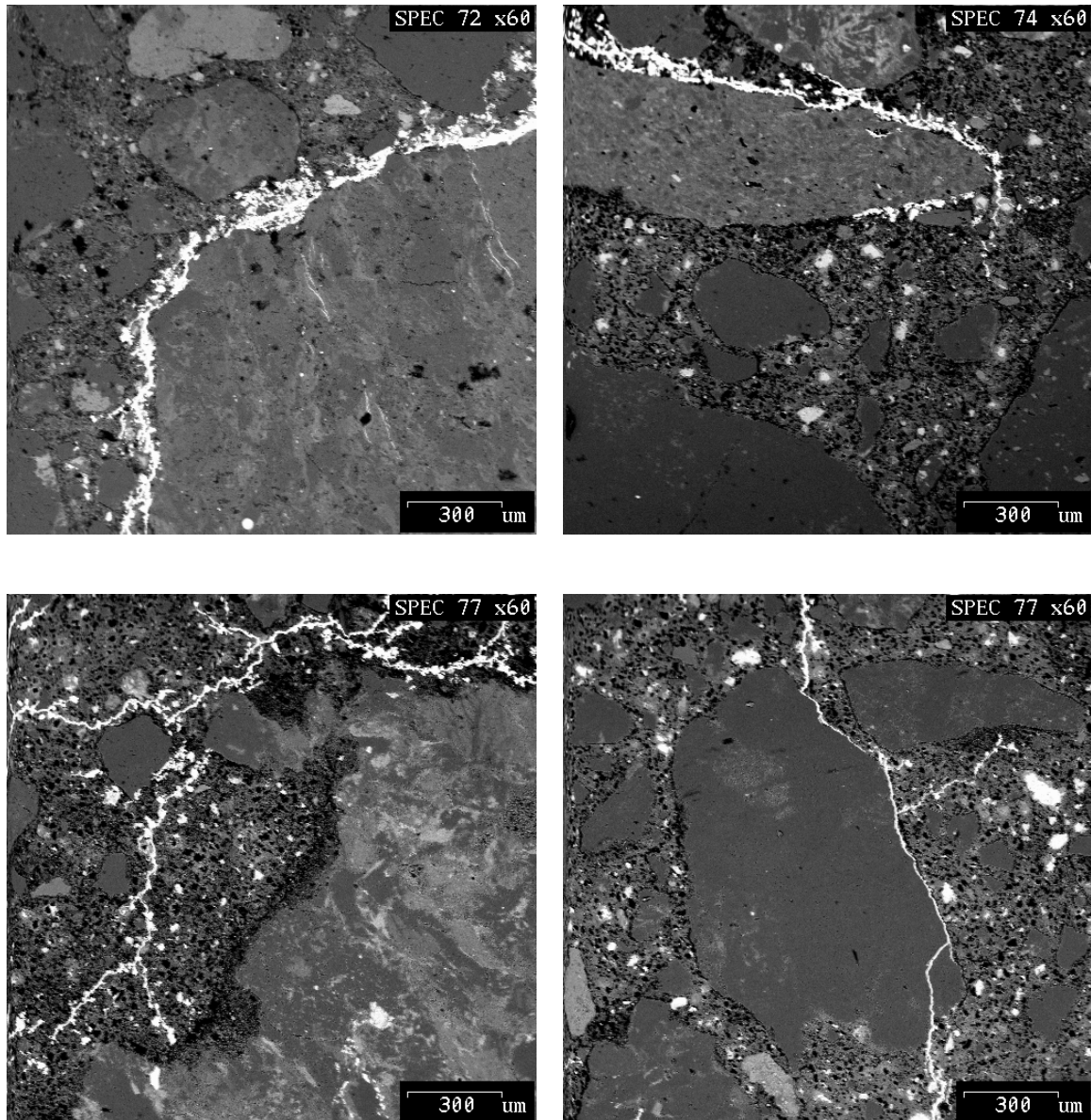


Figure 4.6 SEM micrographs from the partially confined experiment for high-strength concrete

It is clear, then, that less cracking occurs in high-strength than in normal-strength concrete; and because of the stronger cement paste, most of this cracking takes place in the transition zone.

4.3 ORIENTATION OF MICROCRACKS

Most of the microcracks observed were subparallel to the direction of the maximum compression. In all the specimens on which the observations were made, the microcracks were found to exist within a few degrees of the direction of the maximum compression. Figures 4.7 and 4.8 show the microcrack orientation for normal and high-strength concrete specimens. Confined 1 and confined 2 refer to experiments 3 and 4 respectively (see Appendix A). The degree of orientation obtained for the partially confined specimens were base on the cracks in the confined portion.

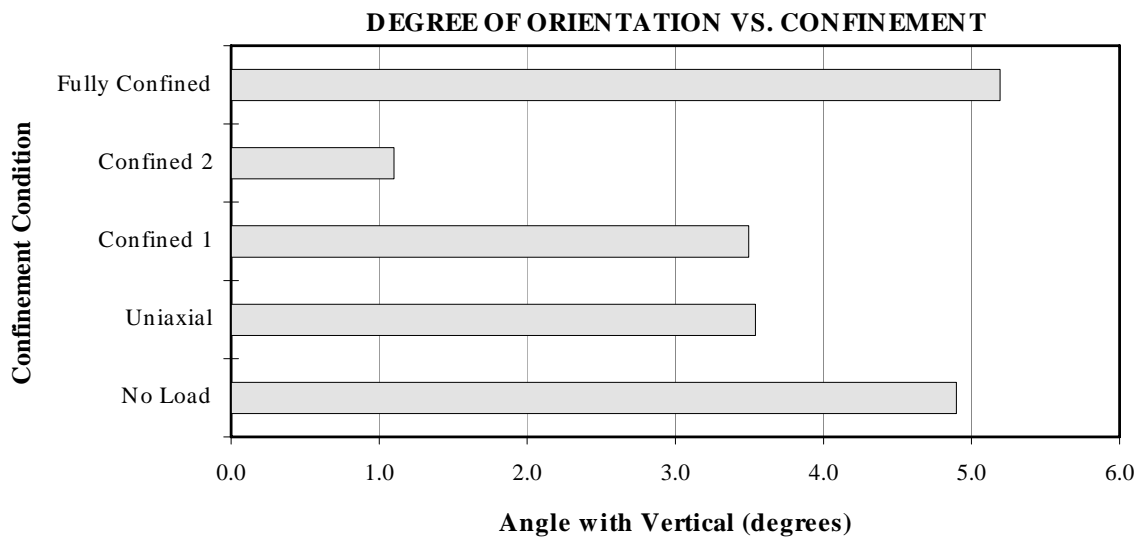


Figure 4.7 Average crack orientation for normal-strength concrete (results of confined 1 and 2 conditions are from the confined portion of the specimen)

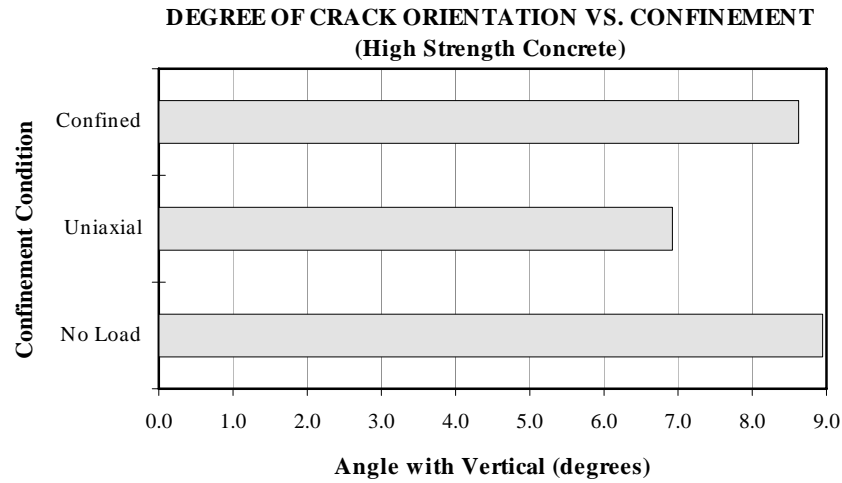


Figure 4.8 Average crack orientation for high-strength concrete

The orientation of microcracks in these figures were algebraic averages of the orientation of the microcracks within each 512×512 pixel square on the corresponding SEM images. The average orientation of microcracks in each of the specimens are listed in Table 4.1. The average values and standard deviations of the orientations listed in the table were obtained assuming normal distribution and using absolute values (ignoring signs) of the angle from the planes of the microcracks to the direction of the maximum compression. The overall average value and standard deviation of the orientation from the normal-strength concrete specimens were 5 degrees and 3 degrees, respectively. The same average values for high-strength concrete were 8 degrees and 2 degrees, respectively.

Table 4.1 Number, length, and orientation of microcracks

CONC. TYPE	EXPERIMENT TYPE	Unsmoothed Crack			Smoothed Crack		
		AVE. NO. OF CRACKS	AVE. LENGTH OF CRACKS	AVE. ANGLE WITH VERTICAL	AVE. NO. OF CRACKS	AVE. LENGTH OF CRACKS	AVE. ANGLE WITH VERTICAL
Normal Strength Concrete	No Load	60	51.4	4.9	21	81.7	2.9
	Uniaxial	86	51.8	3.5	29	85.4	3.3
	Confined 1	65	50.5	3.5	21	80.0	0.8
	Confined 2	37	50.6	1.1	12	73.4	5.9
	Fully Confined	35	49.5	5.2	16	74.8	2.4
High Strength Concrete	No Load	56	39	8.9	20	56.4	2.7
	Uniaxial	82	45	6.9	31	74.0	2.1
	Confined	53	39	8.6	19	51.0	2.9

Table 4.2 summarizes the results of stereological analysis. As described in Chapter 3, after a binary image of the crack network is developed, that binary image is then intersected by an array of straight parallel lines at angles of 0°, 15°, 30°, 45°, 60°, 75°, 90°, 105°, 120°, 135°, 150°, and 165°. The number of crack intercepts at a given angle is measured according to the number of intersections on line array at that angle with the crack network in the binary image.

$$\text{Number of Crack Intercepts}(\theta) = \text{FIELD COUNT}$$

Table 4.2 also shows the total area of the cracks in the binary image. Since the area of each image is known, the percent of the area that is cracked (i.e., crack density) can be determined. Another value in the table below is the surface-to-volume ratio, S_v , determined from the basic equation for obtaining the area of surfaces in a volume, $S_v = 2P_L$. The last column in the table shows the number of crack nodes, which indicates crack branching. For each parameter two values are measured: the first one relates to the unsmoothed crack network from the binary image, and the second value relates to the smoothed version of the cracks.

Table 4.2 Data from stereological analysis

Unsmoothed Crack																		
SPECIMEN	AREA	% AREA	0	15	30	45	60	75	90	105	120	135	150	165	180	TOTAL	S_v	NODES
No Load	8223	1.00	31	31	29	27	29	31	30	30	28	25	28	32	31	349	1.1E-3	28
Uniaxial	11843	1.53	47	48	44	39	41	42	41	42	39	36	42	47	47	506	1.6E-3	40
Confined 1	7337	0.86	28	28	26	24	25	27	27	27	25	22	25	27	28	311	9.6E-4	26
Confined 2	7005	0.77	26	26	25	23	25	27	26	26	24	22	24	26	26	299	9.3E-4	24
Fully Confined	6485	0.74	25	24	23	20	22	23	22	23	21	20	22	25	25	269	8.3E-4	25
No Load	5228	0.98	21	20	19	16	18	20	19	19	18	16	18	20	21	226	7.0E-4	18
Uniaxial	10829	1.90	43	43	39	35	38	41	39	40	36	34	39	43	43	470	1.5E-3	32
Confined	6274	1.21	25	25	23	20	22	23	22	22	21	19	23	25	25	269	8.3E-4	21
Smoothed Crack																		
SPECIMEN	AREA	% AREA	0	15	30	45	60	75	90	105	120	135	150	165	180	TOTAL	S_v	NODES
NO LOAD			20	19	18	15	18	20	21	20	17	15	17	19	20	227	0.00070	4
UNIAXIAL			30	31	27	25	28	30	31	30	26	23	26	30	30	350	0.00108	8
CONFINED 1			18	17	16	14	16	18	19	18	16	13	16	17	18	205	0.00063	4
CONFINED 2			18	18	16	14	17	18	19	18	16	14	15	17	18	206	0.00064	4
FULLY CONFINED			15	14	13	11	12	14	14	14	12	11	13	14	15	166	0.00052	3
NO LOAD			14	14	12	10	12	13	14	13	12	10	12	14	14	155	0.00048	3
UNIAXIAL			31	31	27	25	27	30	31	30	27	23	27	30	31	348	0.00108	7
CONFINED			17	16	14	12	14	15	16	15	14	11	14	16	17	181	0.00056	3

Figures 4.9 and 4.10 are the plots of the number of intercepts of line arrays with the crack networks.

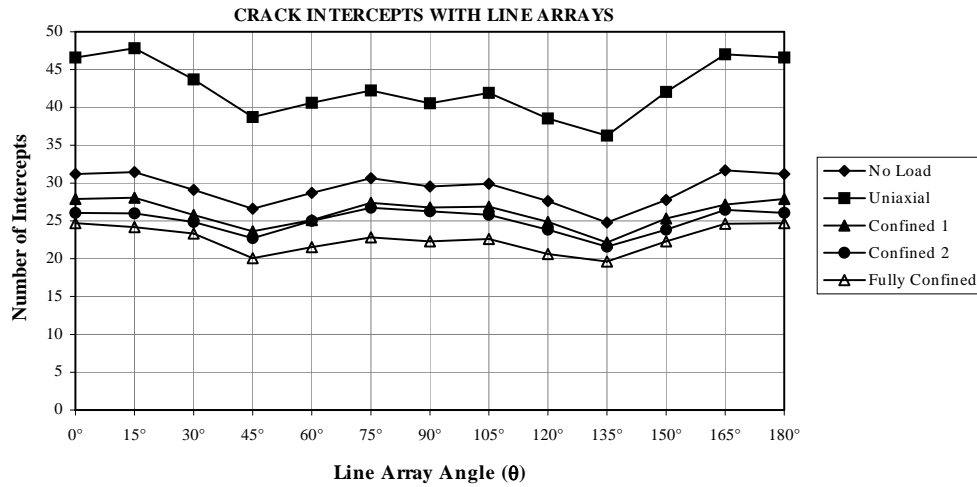


Figure 4.9 Crack orientation for normal-strength concrete

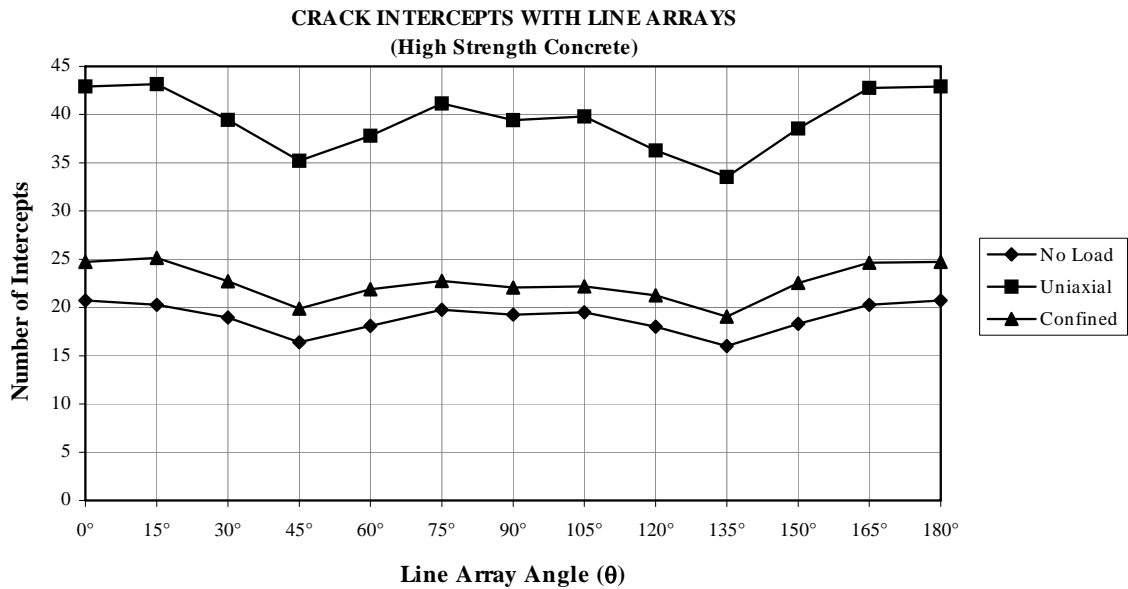


Figure 4.10 Crack orientation for high-strength concrete

Figures 4.11 and 4.12 are the plots of numbers of intercepts of line arrays with the smoothed crack networks.

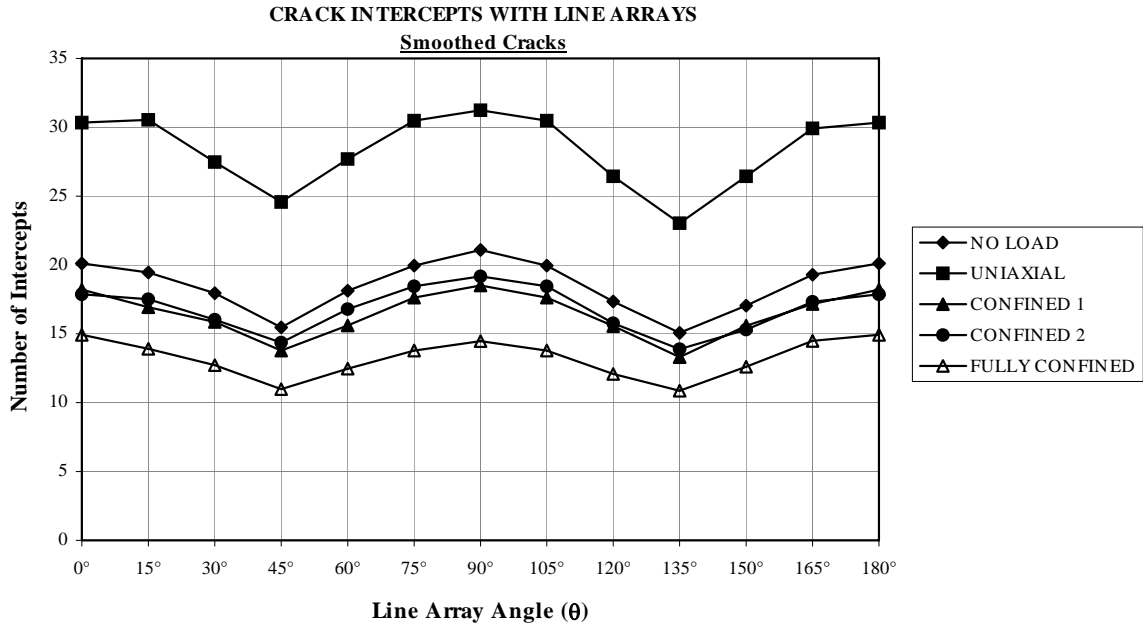


Figure 4.11 Number of intercepts for smoothed cracks

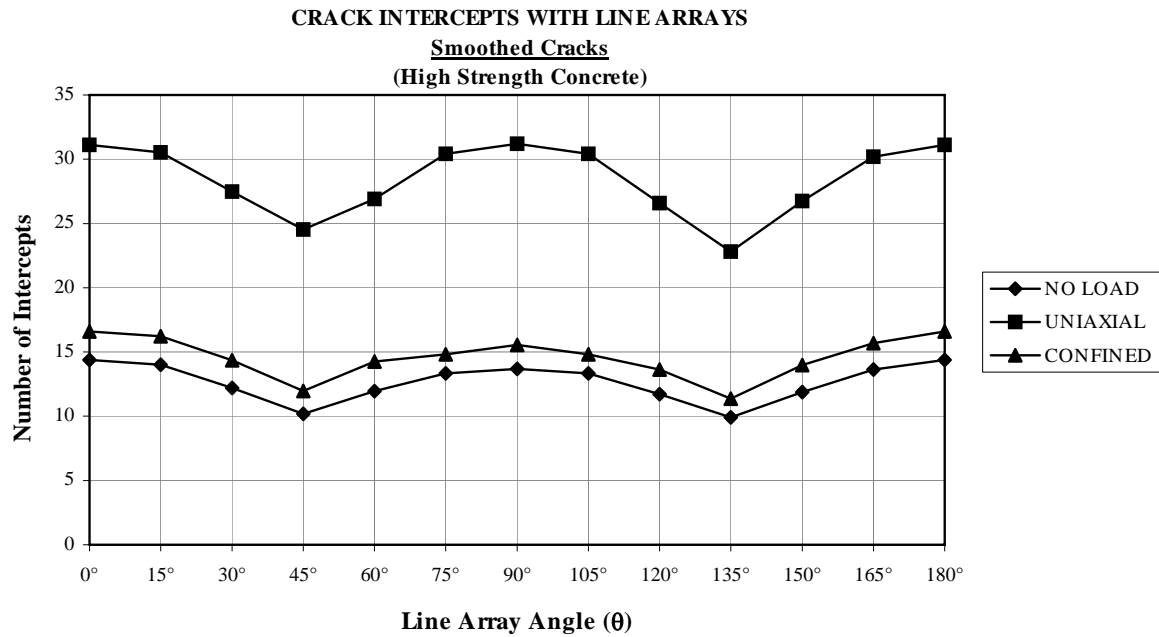


Figure 4.12 Number of intercepts for smoothed cracks

Another way to determine the anisometry of the crack network, $P_L(\theta)$, is to plot it in a polar figure according to the specific orientation of the cracks. The plot of number of intersections versus orientation (in 12 equal angle steps) covers only the range of 0-180 degrees (the range 180-360 degrees is redundant), and is shown in different format than most distribution plots because the *compass rose* pattern makes it easier to interpret the data. A so-called *rose of the number of intersections* is constructed in this way. Figures 4.13 and 4.14 show the rose of the number of intersections for normal and high-strength concrete samples.

From Figures 4.9 through 4.14, it is evident that there is a definite orientation in the crack pattern, and that many cracks lie within 15 degrees of the direction of the maximum compression (between 0 to 15 degrees and 165 to 180 degrees). This holds true on all five normal-strength concrete specimens as well as the three high-strength specimens.

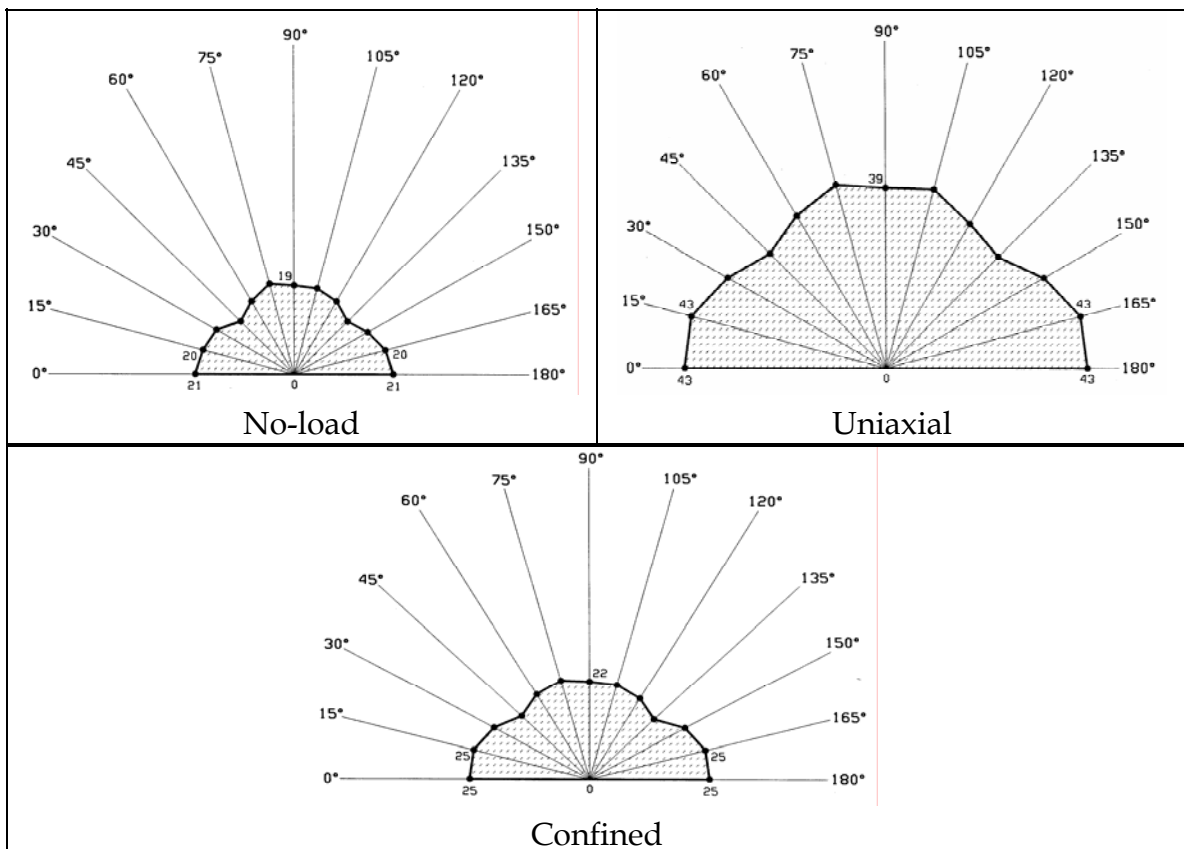


Figure 4.13 Rose of the number of intersections diagrams for high-strength concrete

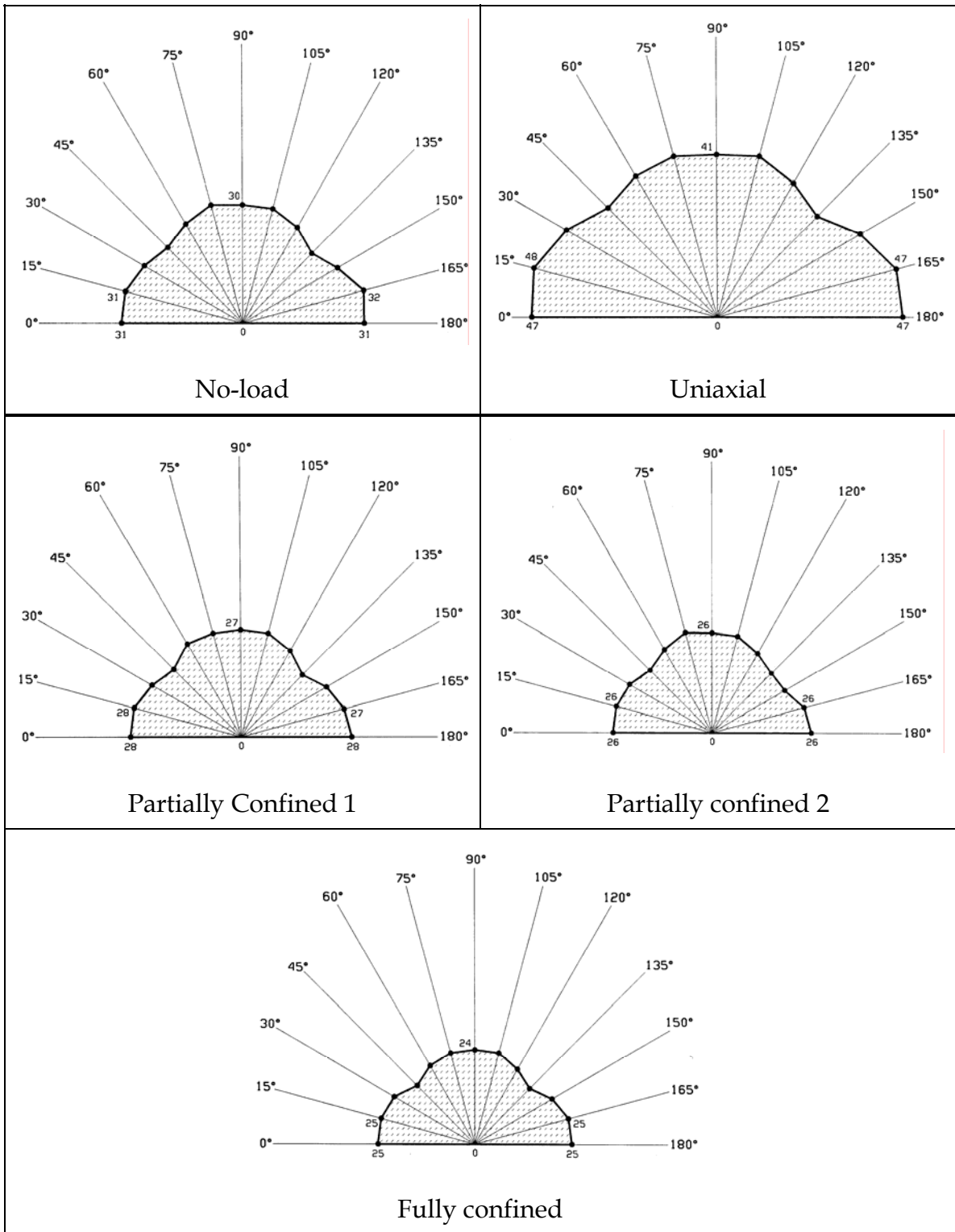


Figure 4.14 Rose of the number of intersections diagrams for normal-strength concrete

Careful examination of the micrographs reveal that microcracks may not necessarily be generated subparallel to the direction of the maximum compression. The initial orientation of the microcracks is dependent on the orientation of the local tensile stress which is responsible for the generation of the cracks (Zheng 1989). The microcracks turn towards the direction of maximum compression after they are generated and propagate in this direction throughout most of their length. The stress intensity factors generated by the overall stress field are favorable to opening microcracks against the least compressive stress. As a result, the microcracks turn towards the most favorable direction, which is parallel to the maximum compression.

Microcrack tips observed at a higher magnification appear to turn and change direction before they fully stop propagating. Figures 4.15 (a) and 4.15 (b) are higher magnification micrographs of crack tips that show this behavior.

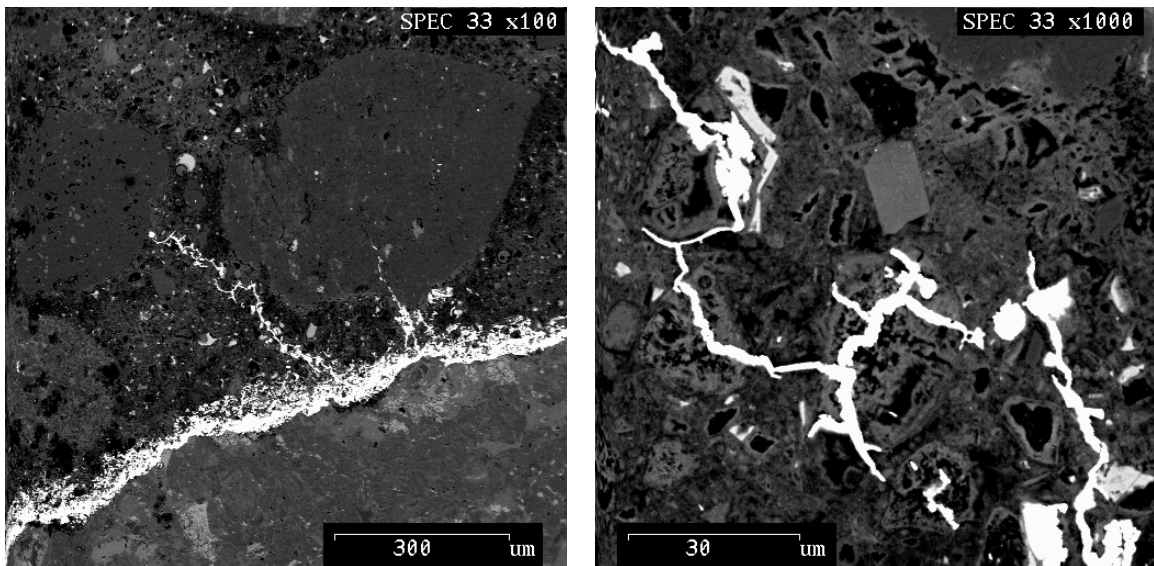


Figure 4.15 (a) SEM micrographs showing crack tips at higher magnification
(The direction of maximum compression is vertical)

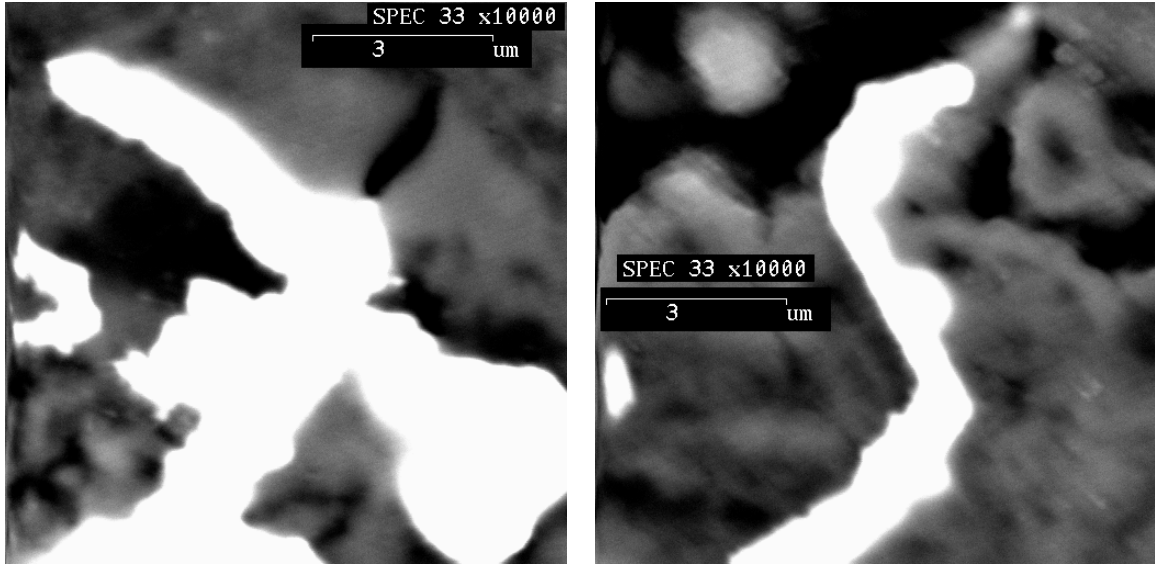


Figure 4.15 (b) SEM micrographs showing crack tips at higher magnification
(The direction of maximum compression is vertical)

This phenomenon may be explained as follows. As the crack starts to propagate, the energy that causes the propagation of the cracks is much greater than the energy required to generate fresh new surfaces. At this stage, the direction of the crack propagation is mainly controlled by the direction of the stress intensity factor, which is usually greatest when the crack plane is perpendicular to the least compressive stress. The crack at this stage propagates in the direction of the maximum compression. By the end of propagation, the energy that drives it is insufficient to continue the crack along unfavorable surfaces, but is still greater than that required to open new surfaces along one of the weak planes. The crack then turns into the weak plane that had the smallest angle with the maximum compression (Zheng 1989).

4.4 MICROCRACK DENSITY DISTRIBUTION

The microcrack density distribution, Γ , represents the number of microcracks per unit of observation area. Pore spaces were not counted as microcracks. For a body of volume V (unit thickness) containing N cracks with initial cracks of length ℓ_0 , the initial crack density parameter Γ is given by:

$$\Gamma = \frac{N\ell_0^2}{V} \quad (4.1)$$

The crack density parameter Γ , in an image of area A with N cracks of length ℓ_i , can be obtained from the following relationship:

$$\Gamma = \frac{\sum_{i=1}^N \ell_i^2}{A} \quad (4.2)$$

Where:

Γ = Crack density parameter

ℓ_i = Crack length (mm)

A = SEM image area (512 pixels \times 512 pixels = 2.8358 mm²)

Table 4.3 shows the average crack density parameters for all experiments. The reference specimen (no-load sample) has a relatively high crack density due to the fact that concrete is heavily cracked even before applying any load (Hsu et al. 1963). Hence, the effective crack density increase for the specimen subjected to applied loads is the difference between the final crack density and the crack density of the no-load specimen. The crack densities for the partially confined concrete cylinders in Table 4.3 are only the crack densities in the confined portion of the samples, i.e., specimens 1 and 2 in Figure 2.25. The tension in the wire wound around partially confined 2 sample (Experiment #4) is higher than that on partially confined 1 sample (Experiment #3).

Table 4.3 Crack density for different loading conditions

EXPERIMENT	CONCRETE TYPE	CRACK DENSITY
No-load	Normal-Strength	0.0444
Uniaxial	Normal-Strength	0.0919
Partially Confined 1	Normal-Strength	0.0308
Partially Confined 2	Normal-Strength	0.0285
Fully Confined	Normal-Strength	0.0262
No-load	High-Strength	0.0124
Uniaxial	High-Strength	0.1245
Partially Confined	High-Strength	0.0410

Figures 4.16 and 4.17 show the crack density as a function of confinement for normal and high-strength concrete specimens. From these two figures the effect of confinement on crack density is quite evident.

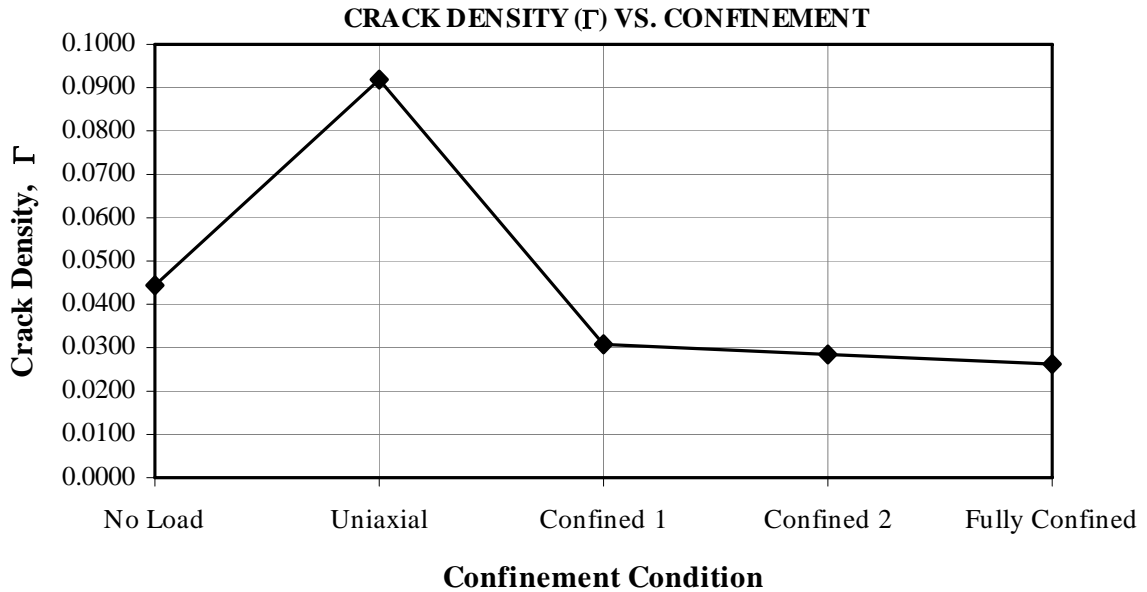


Figure 4.16 Crack density, Γ , as a function of confinement for normal-strength concrete

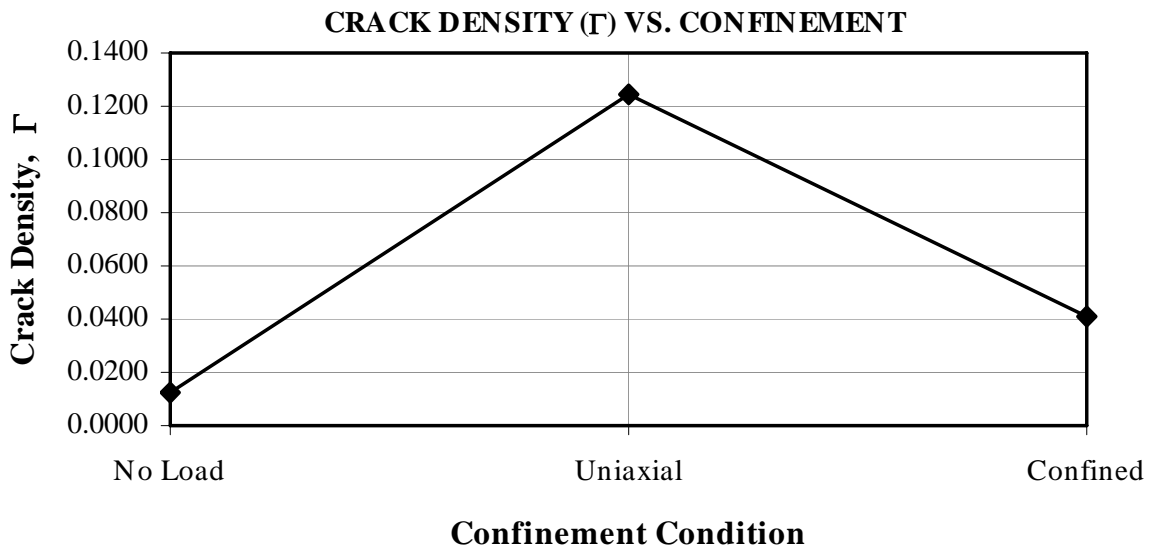


Figure 4.17 Crack density, Γ , as a function of confinement for high-strength concrete

The specimens subjected to uniaxial compression had the highest crack density. With increasing confining stress, the average crack densities decreased. Specimen 5, which was fully confined and subjected to the greatest confining stress, had the lowest crack density. Specimens 3 and 4 which were both partially confined, had very close crack densities. In the case of high-strength concrete, the number of cracks decreased substantially when confinement was introduced.

Figures 4.18 and 4.19 illustrate the crack length and crack densities for the partially confined specimens in both confined and unconfined portions of the specimen for Experiments #3 and #4 which were subjected to a confining stress over each end, and uniaxial compression over the center. In both cases the crack densities in the center and edge of the sample are smaller in the confined portion than in unconfined portion. Also, in both experiments, the average crack length is smaller in the center portion of the specimen than along the edge.

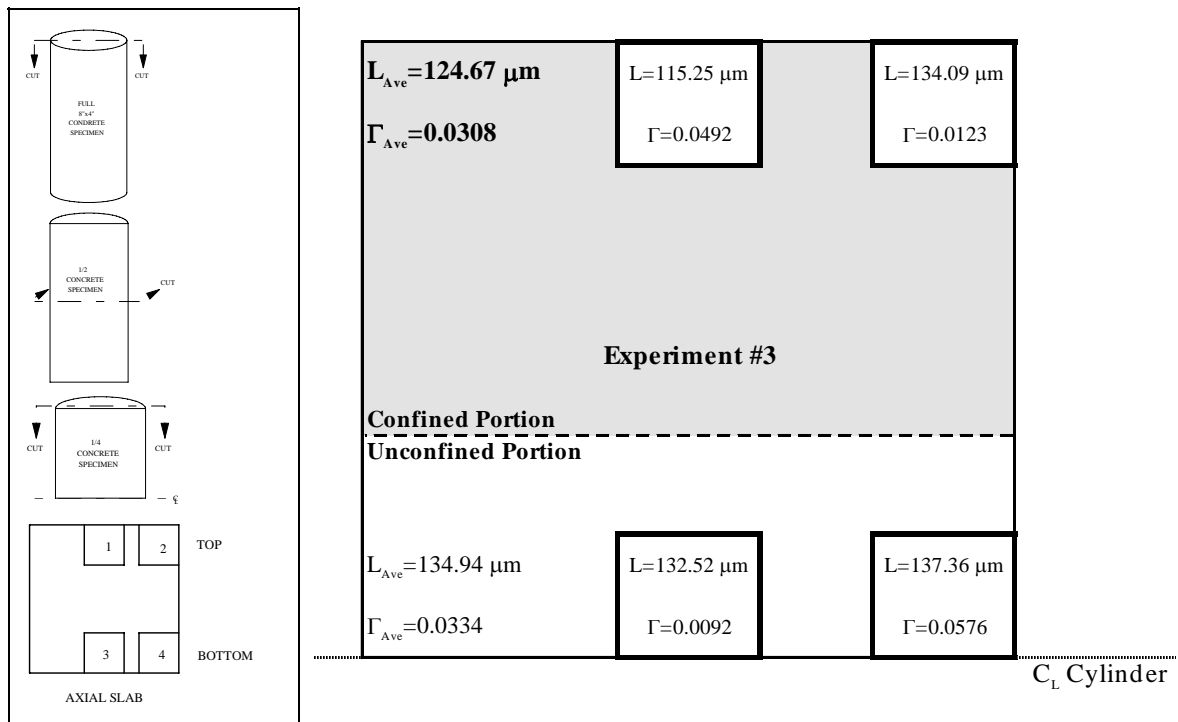


Figure 4.18 Diagrammatic representation of crack length and crack density at confined and unconfined portions of Experiment #3

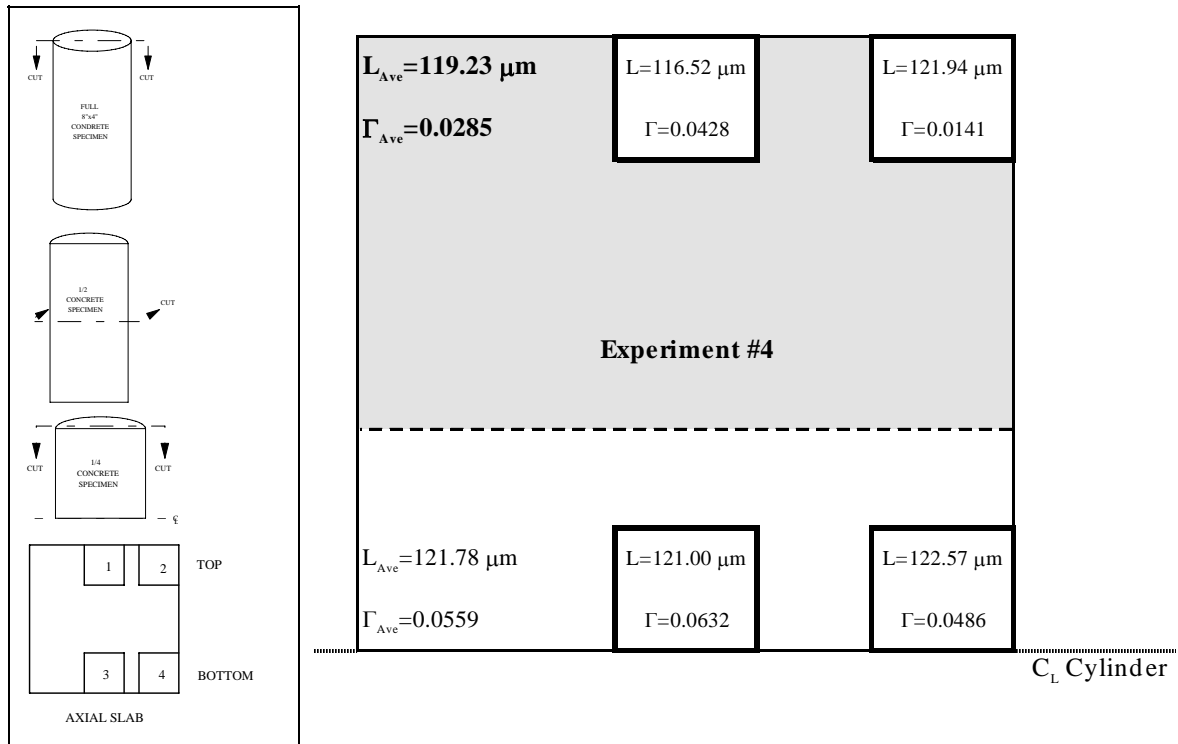


Figure 4.19 Diagrammatic representation of crack length and crack density at confined and unconfined portions of Experiment #4

Another way of assessing the crack density is by counting the number of microcracks per unit of observation area (see Table 4.1). Pore spaces were not counted as microcracks. Figures 4.20 and 4.21 show that the number of cracks is strongly influenced by confining condition for both types of concrete.

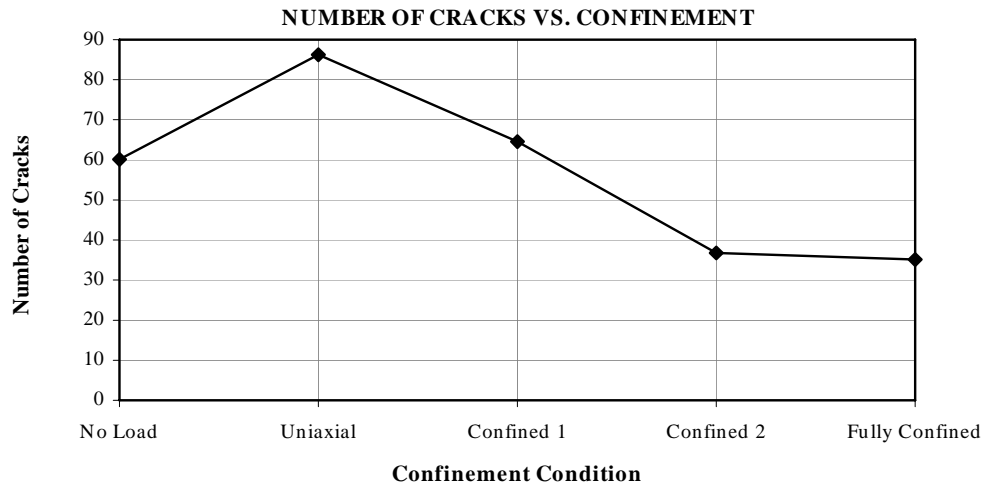


Figure 4.20 Number of cracks as a function of confinement for normal-strength concrete

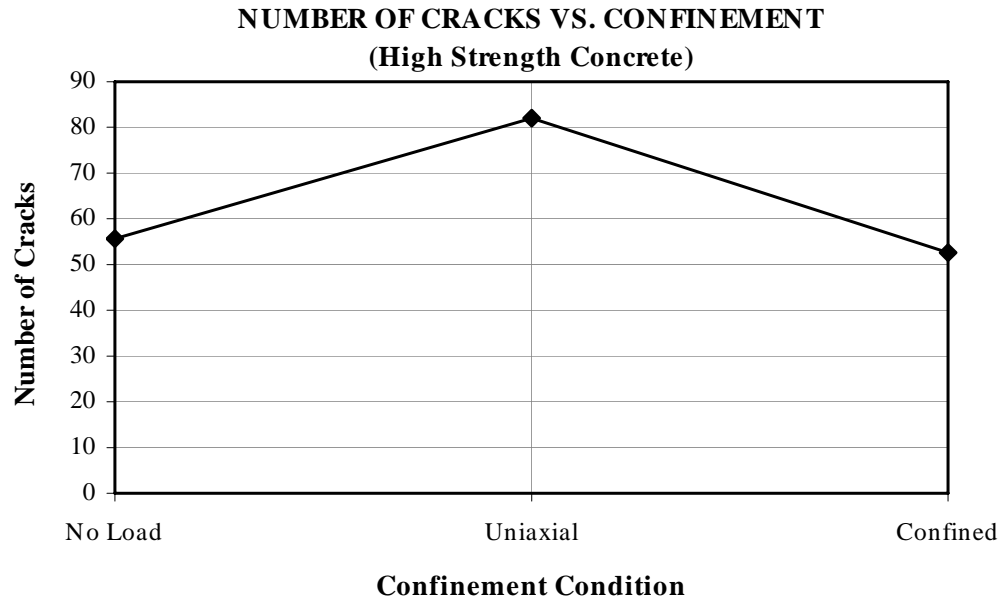


Figure 4.21 Number of cracks as a function of confinement for high-strength concrete

Crack density can also be measured in terms of percent cracked area (see Table 4.2). Figures 4.22 and 4.23 are the plots of percent cracked area as a function of confinement. Again, percent cracked areas decrease as the confinement increases, for both normal and high-strength concrete specimens.

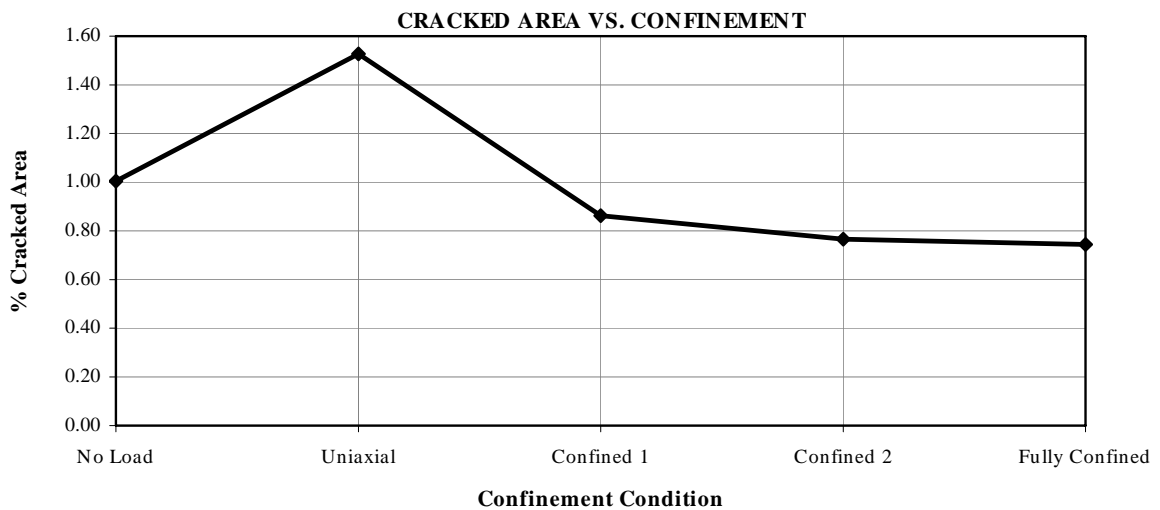


Figure 4.22 Percent cracked area as a function of confinement for normal-strength concrete

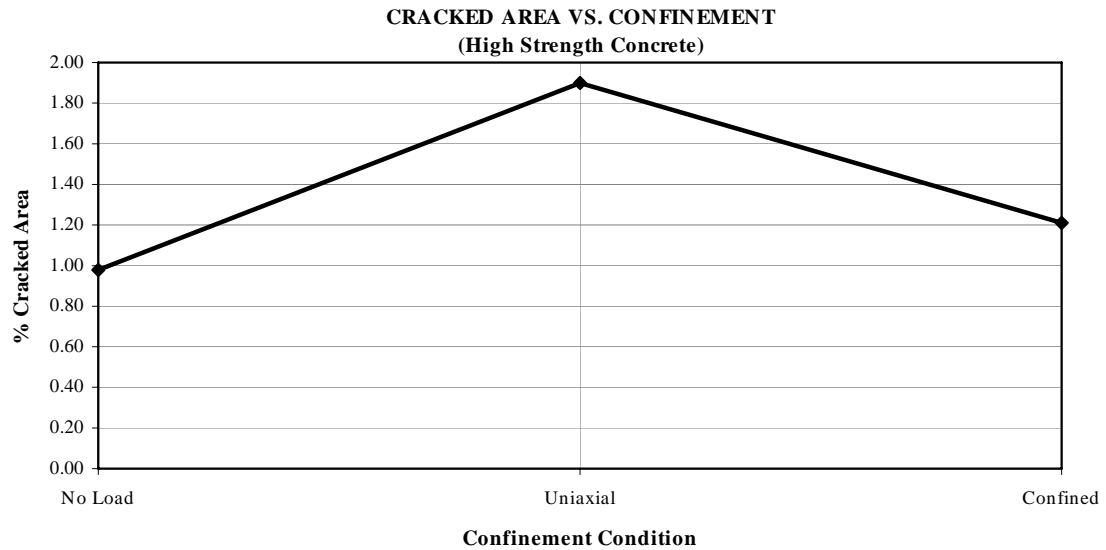


Figure 4.23 Percent cracked area as a function of confinement for high-strength concrete

The influence of confining stress on microcrack density was described by Kranz (1983) as follows. Microcracks are generated by local tensile stresses, which depend on the geometry of pores and aggregates, and material heterogeneity, as well as magnitude and direction of applied stresses. With increasing confining stress, an increasing hydrostatic stress is applied to the concrete; as a result, the local tensile stress which is responsible for the generation of microcracks is reduced. The superposition of hydrostatic pressure upon an existing deviatoric stress field is likely to decrease the range and magnitude of deviatoric stresses concentrated near crack tips, as well as increase frictional resistance to shear between crack surfaces in contact. For extensile cracks, this increases the energy of stress requirements for propagation and thereby makes crack interaction less probable. This most probably explains the decreasing microcrack density when confining stress is introduced.

The stereological measurement of the surface-to-volume ratio, S_v (S/V), was determined from the basic equation for obtaining the total crack surface area per unit of volume. Plots of S_v as a function of confinement are presented in Figures 4.24 and 4.25 for normal-strength and high-strength concrete specimens, respectively.

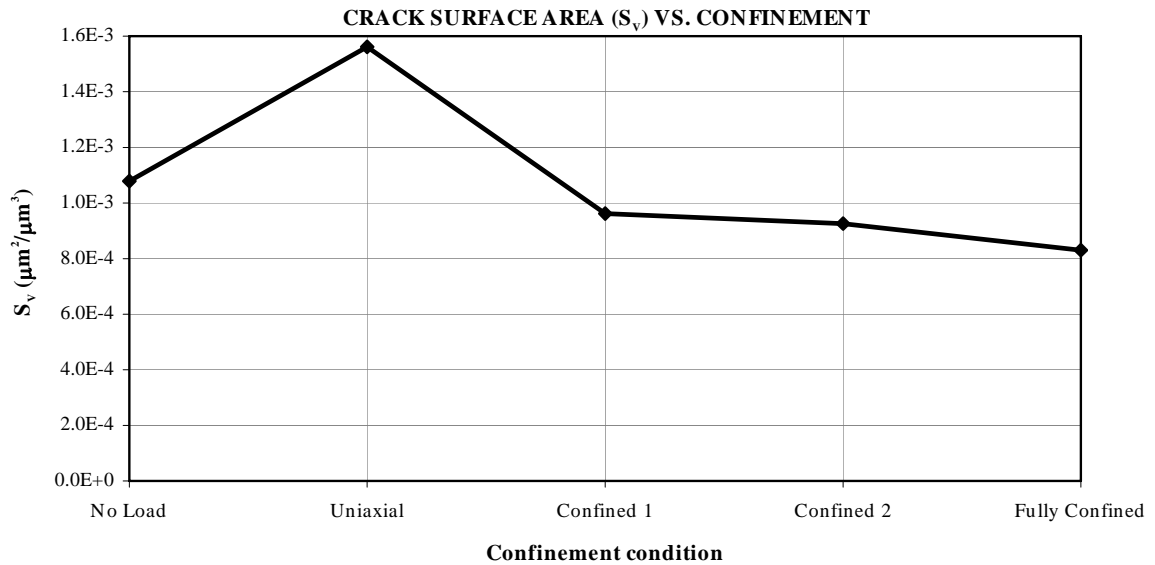


Figure 4.24 Crack surface area (S_v) as a function of confinement condition for normal-strength concrete

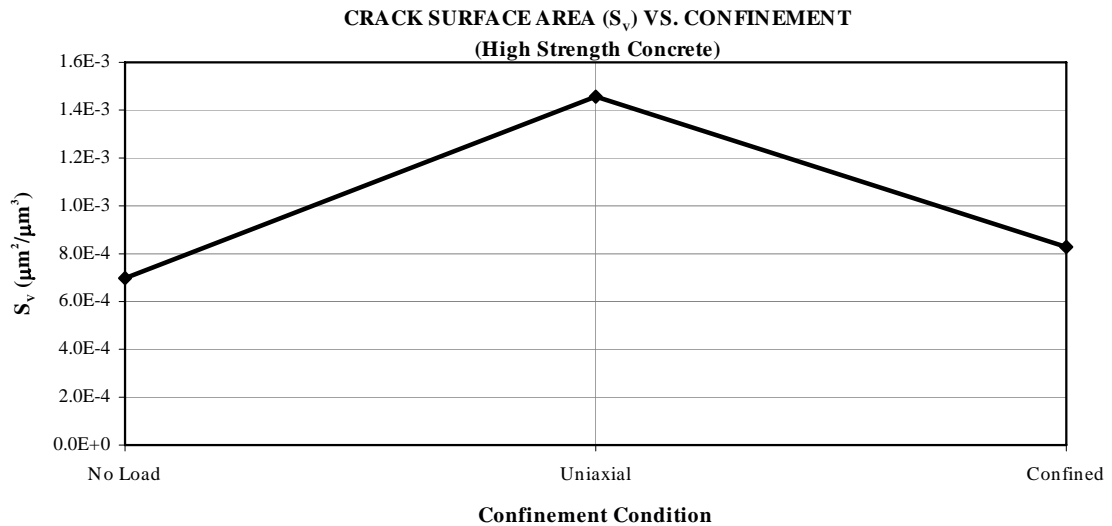


Figure 4.25 Crack surface area (S_v) as a function of confinement condition for high-strength concrete

Crack surface area, S_v , decreases as the confining stresses increases in both normal and high-strength concrete cases.

4.5 MICROCRACK LENGTH DISTRIBUTION

The average length distribution of the microcracks strongly depends on the confining stress. In the specimen subjected to uniaxial compression, most of the microcracks propagated to a certain length and stopped. When confining stress was introduced, the average length of the microcracks decreased, as indicated in Figures 4.26 and 4.27. With increasing confining stress, the average length of microcracks decreased. Specimen #5, which was fully confined, had the lowest crack length. In the partially confined specimens (Experiments #3 and #4), the influence of confinement of the crack length is illustrated in Figures 4.18 and 4.19, which show clearly that the average length distribution of microcracks is strongly dependent on the confining stress.

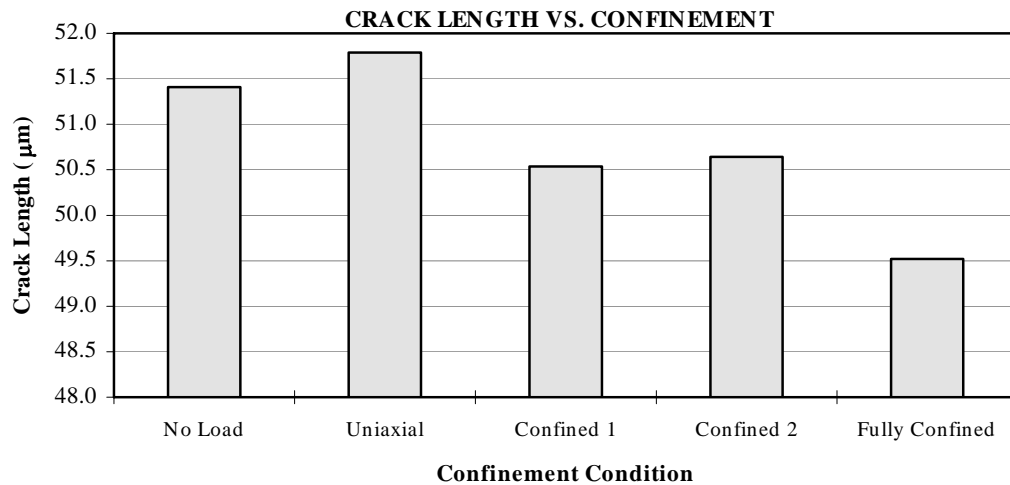


Figure 4.26 Crack length as a function of confinement condition for normal-strength concrete specimens

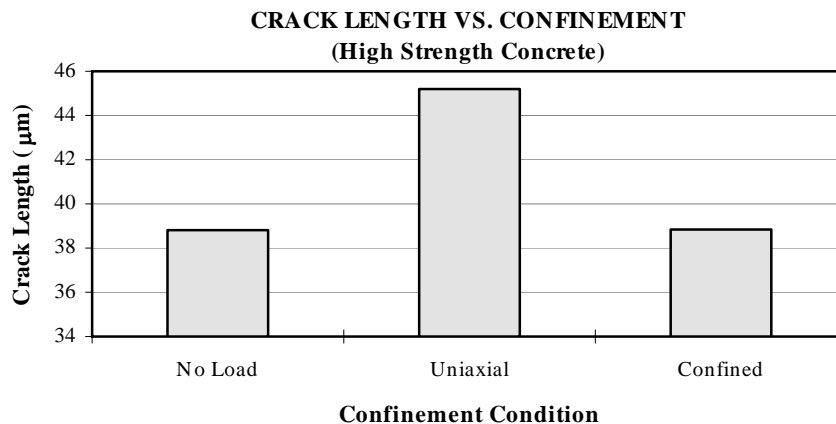


Figure 4.27 Crack length as a function of confinement condition For high-strength concrete specimens

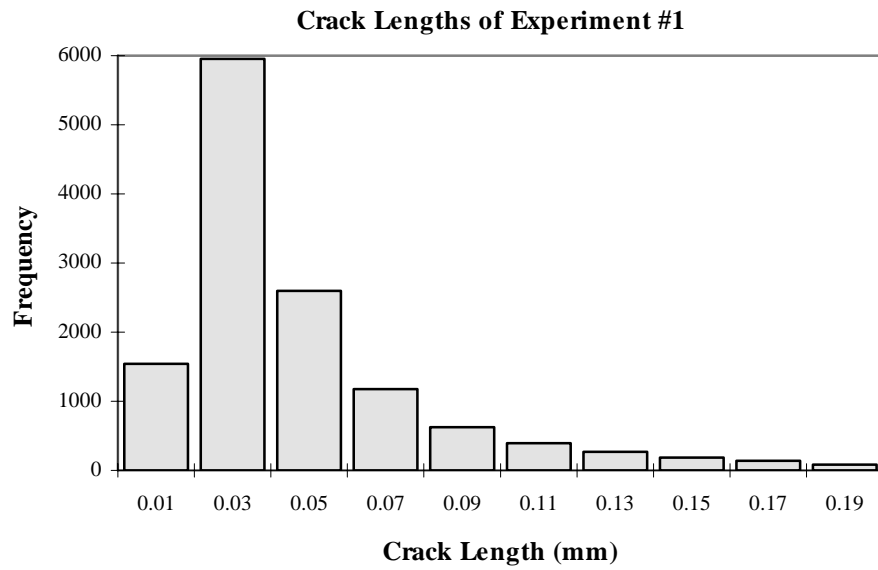


Figure 4.28 Histogram of microcrack length distributions for the no-load experiment of the normal-strength concrete

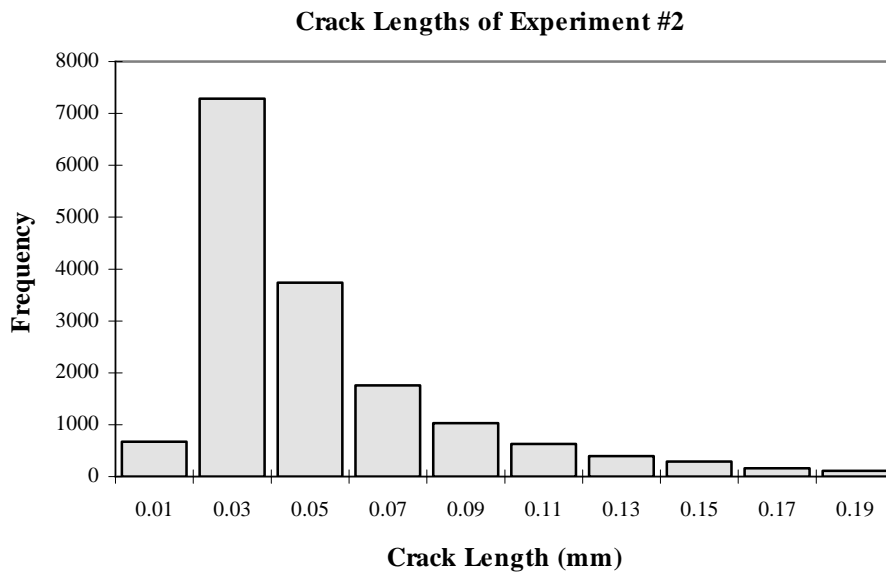


Figure 4.29 Histogram of microcrack length distributions for the uniaxial experiment of the normal-strength concrete

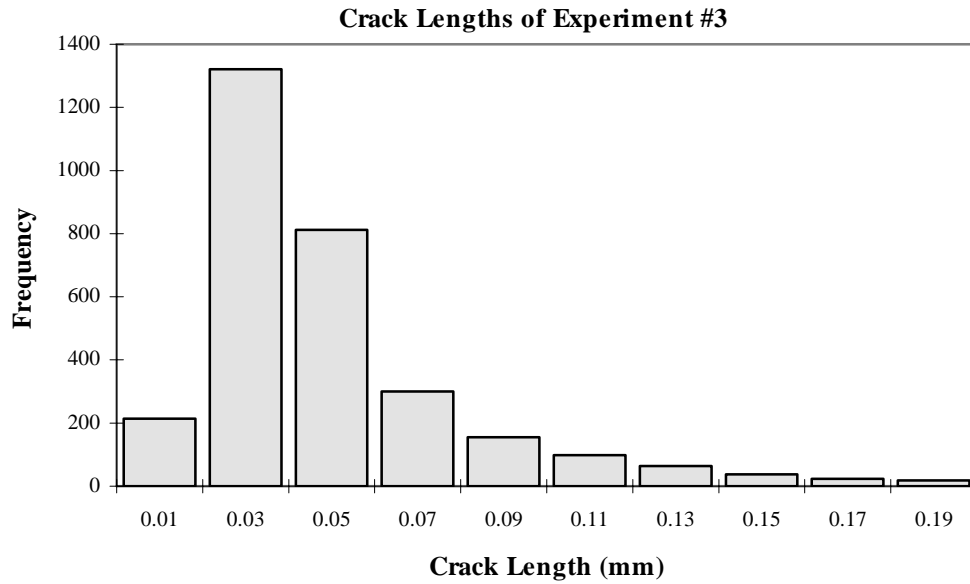


Figure 4.30 Histogram of microcrack length distributions for the partially confined (1) experiment of the normal-strength concrete

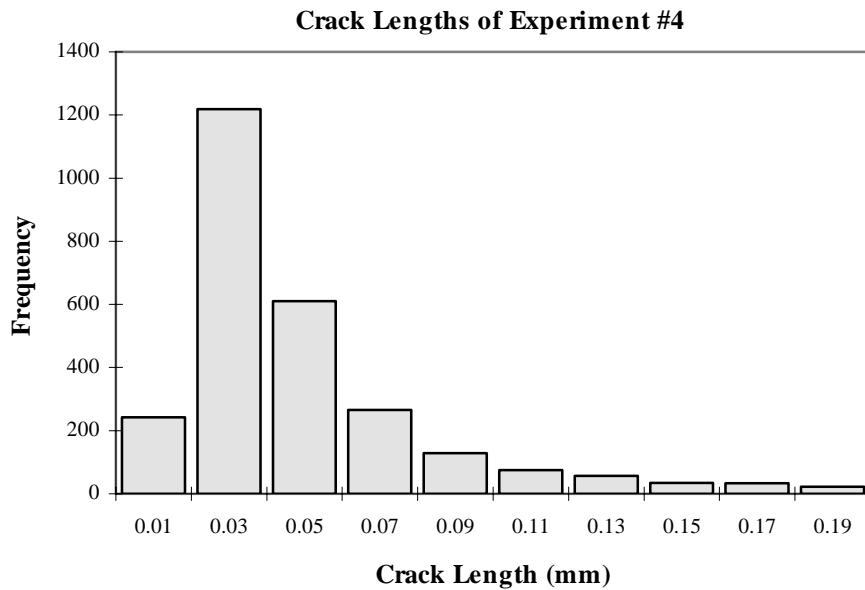


Figure 4.31 Histogram of microcrack length distributions for the partially confined (2) experiment of the normal-strength concrete

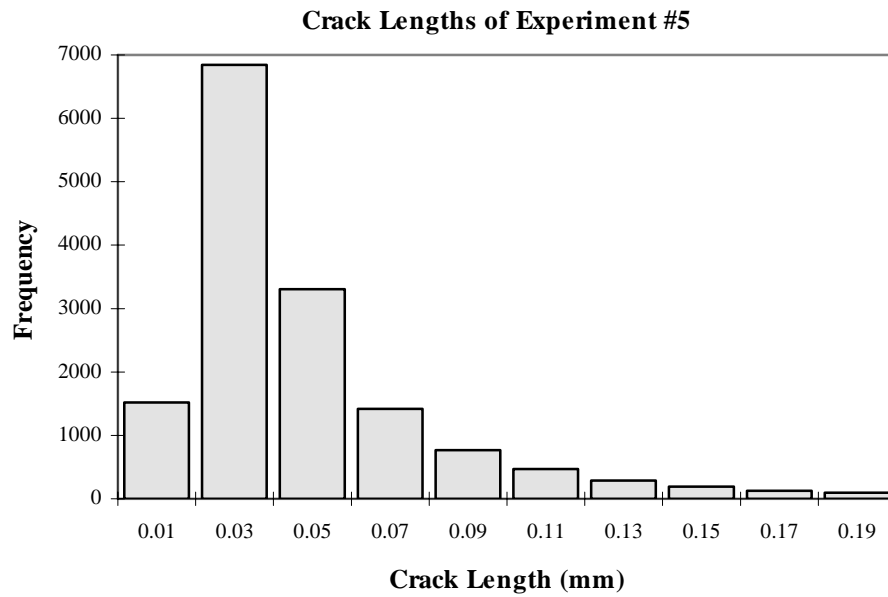


Figure 4.32 Histogram of microcrack length distributions for the fully confined experiment of the normal-strength concrete

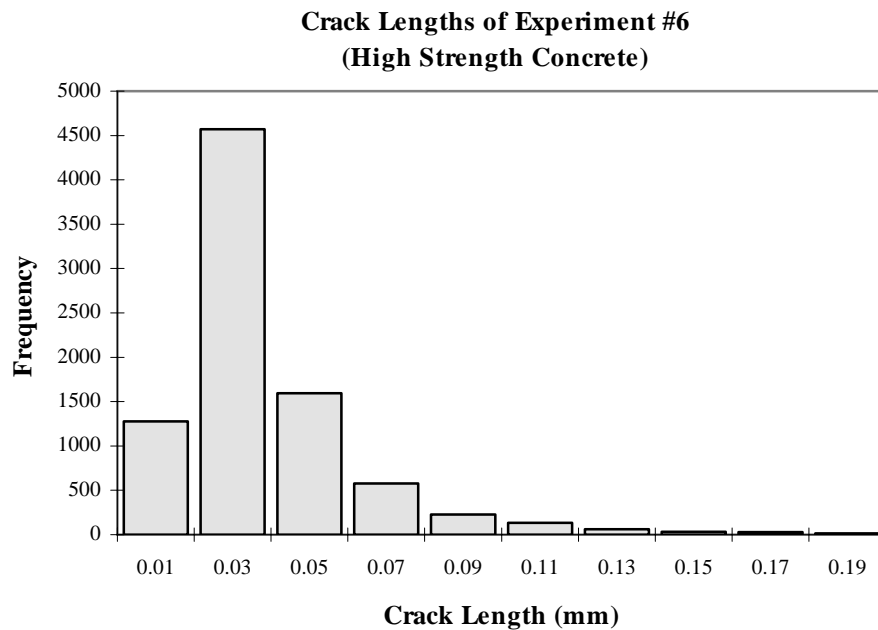


Figure 4.33 Histogram of microcrack length distributions for the no-load experiment of the high-strength concrete

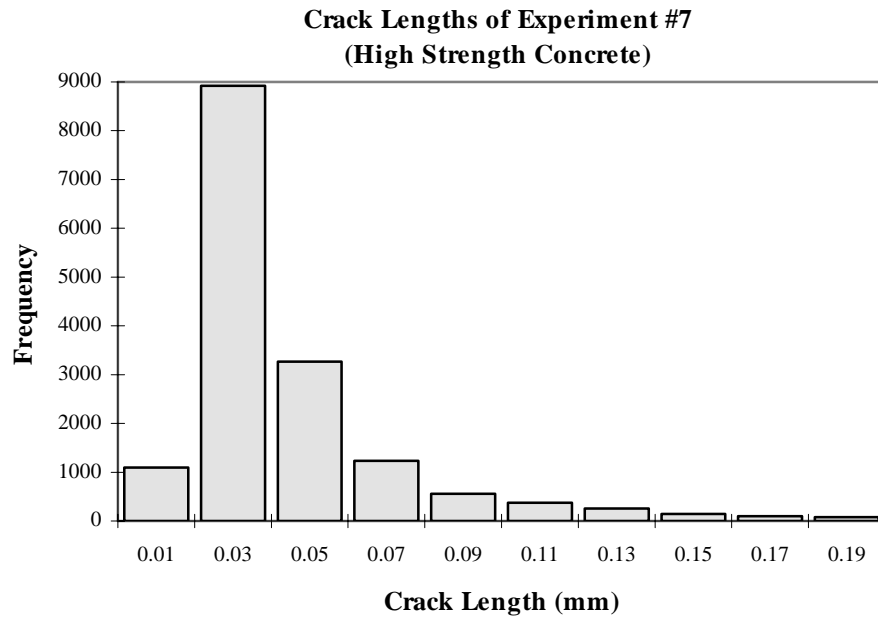


Figure 4.34 Histogram of microcrack length distributions for the uniaxial experiment of the high-strength concrete

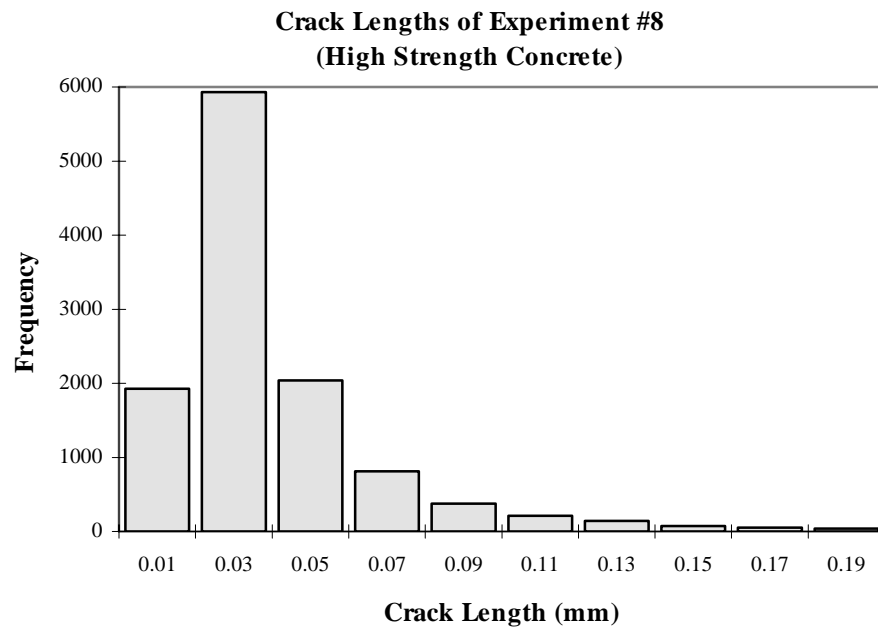


Figure 4.35 Histogram of microcrack length distributions for the partially confined experiment of the high-strength concrete

With increasing confining stress, both the average lengths of microcracks and the ratio of their standard deviation to average length, known as the coefficient of variation (COV), decreased. Figures 4.28 through 4.35 show the crack length histograms of five normal-strength and three high-strength concrete specimens.

Table 4.4 Tabulates the crack length, standard deviation, and the coefficient of variation for all the experiments.

Table 4.4 Coefficient of variation of crack length

Conc. Type	Experiment Type	Avg. Crack Length (mm)	Standard Deviation	Coef. of Variation
Normal Strength Concrete	No Load	0.05086	0.0506	0.99
	Uniaxial	0.05552	0.0454	0.82
	Confined 1	0.05248	0.0430	0.82
	Confined 2	0.05149	0.0413	0.80
	Fully Confined	0.04959	0.0390	0.79
High Strength Concrete	No Load	0.03922	0.0303	0.77
	Uniaxial	0.04996	0.0589	1.18
	Confined	0.04200	0.0387	0.92

Figures 4.36 and 4.37 are the plot of the coefficient of variation as a function confining condition for normal-strength and high-strength concrete specimens.

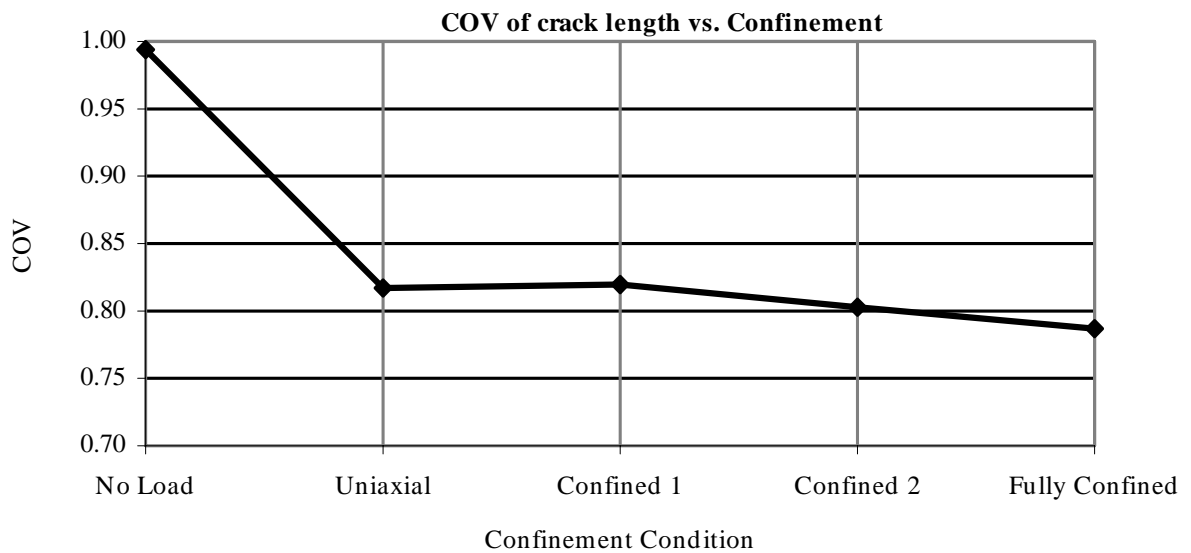


Figure 4.36 COV of crack length as a function of confinement for normal-strength concrete

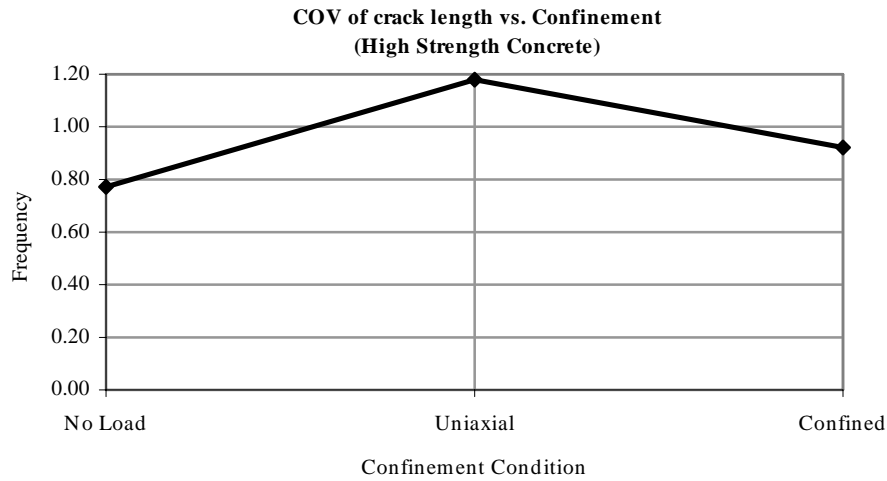


Figure 4.37 COV of crack length as a function of confinement for high-strength concrete

Table 4.4 and Figures 4.36 and 4.38 indicate that with increasing confining stress, the average lengths and the coefficient of variation of crack lengths (the ratio of standard deviation of microcrack lengths to average length of microcracks) decrease.

The stress intensity factor is a fundamental quantity that governs the stress field near the crack tip. The propagation of microcracks is controlled by the stress intensity factor at the microcrack tips, resulting from both local tensions, which generate the microcracks, and the overall stress field. The confining stress, which is orthogonal to the direction of maximum compression, adds a negative stress intensity factor, which stops the propagation of the extensile microcracks (Zheng 1989) (Figure 4.38).

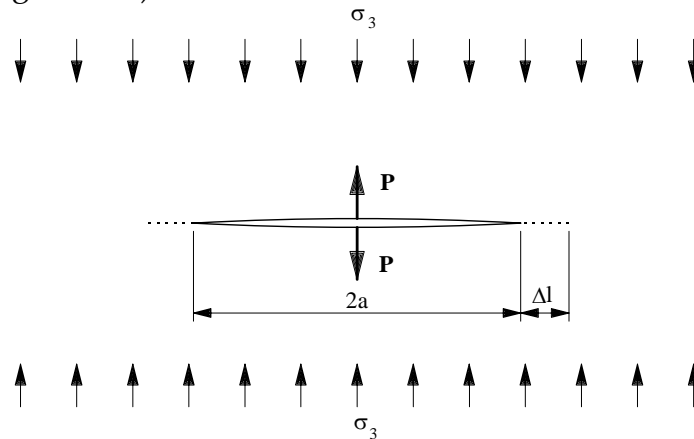


Figure 4.38 Stress intensity factors due to local tension P and confining stress, σ_3
 ($K_I = P/\sqrt{\pi l}$ and $K_I = \sigma_3\sqrt{\pi l}$)

This negative stress intensity factor increases (in the negative sense) in proportion to the increase in confining stress. As a result, crack lengths are reduced by an increase in confining stress. Using a centrally loaded crack model from linear elastic fracture mechanics, a simple equation for the crack length under confining stress, relative to an unconfined crack, can be expressed as follows (Zheng 1989):

$$L = \frac{2}{\pi} \left(\frac{\sigma_t \beta}{K_{IC}} \right)^2 \quad (4.3)$$

for $\sigma_r = 0$, and

$$L = \frac{2}{\pi} \left(\frac{\sqrt{K_{IC}^2 - 4\beta\sigma_r\sigma_t} - K_{IC}}{2\sigma_r} \right)^2 \quad (4.4)$$

for $\sigma_r \neq 0$

where: L = microcrack length
 K_{IC} = fracture toughness of concrete
 σ_r = confining stress
 σ_t = local tensile stress responsible for the microcrack generation
 β = efficient depending on the geometry and boundary conditions of the microcracks.

Because the microcracks are produced by local tensile stresses, the driving forces from the local tensile stresses decrease as the microcrack length increases. On the other hand, the negative driving forces applied by the confining stress increase as the microcrack length increases. The combined effect of these two arguments is a great reduction in microcrack length under high confining stress.

Based on stereological analysis, L_A , the length of line per unit area also decreases with increasing confining stresses. Figures 4.39 and 4.40 show the relationship between L_A and confinement condition for normal and high-strength concrete.

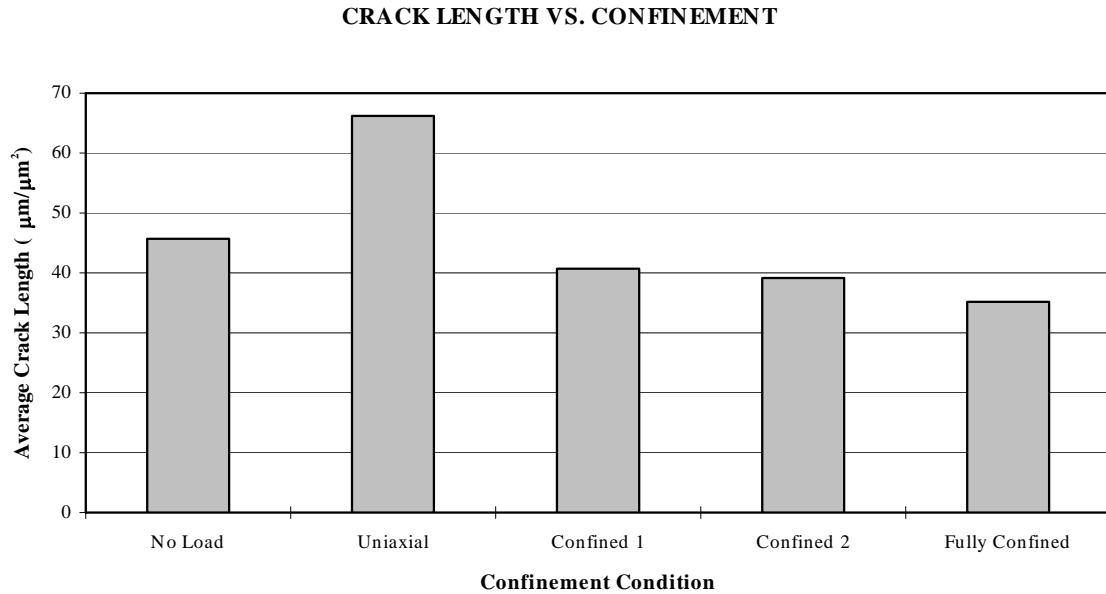


Figure 4.39 Stereological measurement of crack length as a function of confinement condition for normal-strength concrete specimens

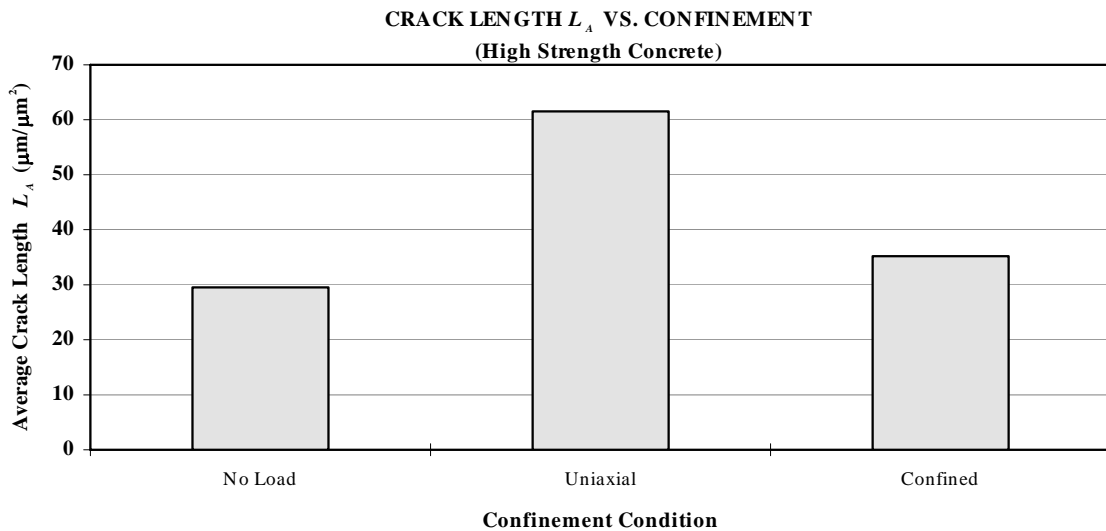


Figure 4.40 Stereological measurement of crack length as a function of confinement condition for high-strength concrete specimens

4.6 MICROCRACK BRANCHING

Cracks with frequent branching are often observed in the fracture process of brittle and quasi-brittle materials such as ceramics and concrete. The crack branching patterns of materials are very complex and irregular; however, quantitative analysis of branching patterns could reveal some important information about the stress applied during crack propagation, as well as material characteristics such as surface energy and the elastic constant (Nakasa and Nakatsuka 1991, 1994). Fractal analysis has also been applied to complex branching patterns (Mandelbrot 1977).

For crack branching analysis, a computer program has been developed to measure the number of 3-way and 4-way crack-branching nodes similar to the ones shown in Figure 4.41 (see Appendix B).

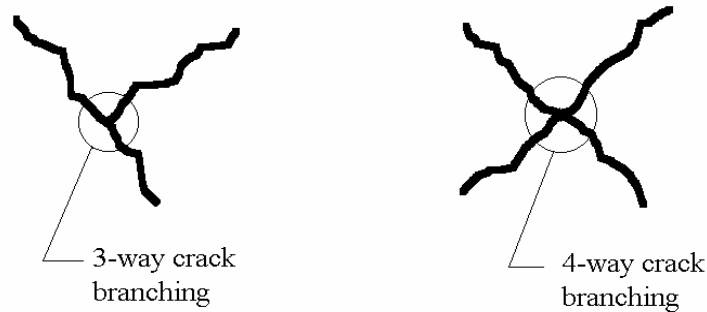


Figure 4.41 3-way and 4-way crack branching nodes

Figures 4.42 and 4.43 show that as the confining stress increases, the number of crack branching nodes decreases. This is expected by the fact that since the propagation of microcracks is controlled by the stress intensity factor at the microcrack tips, as the confining stress increases, the negative stress intensity factor imposed by confinement increases proportionately. This limits the energy required for cracks to grow and branch off. The amount of branching in the high-strength concrete is considerably less than the number of cracks in the normal-strength concrete. This can be attributed to the fact that high-strength concrete is much more brittle than normal-strength concrete. As a result, when

fracture occurs in high-strength concrete, the crack propagation is associated with less branching.

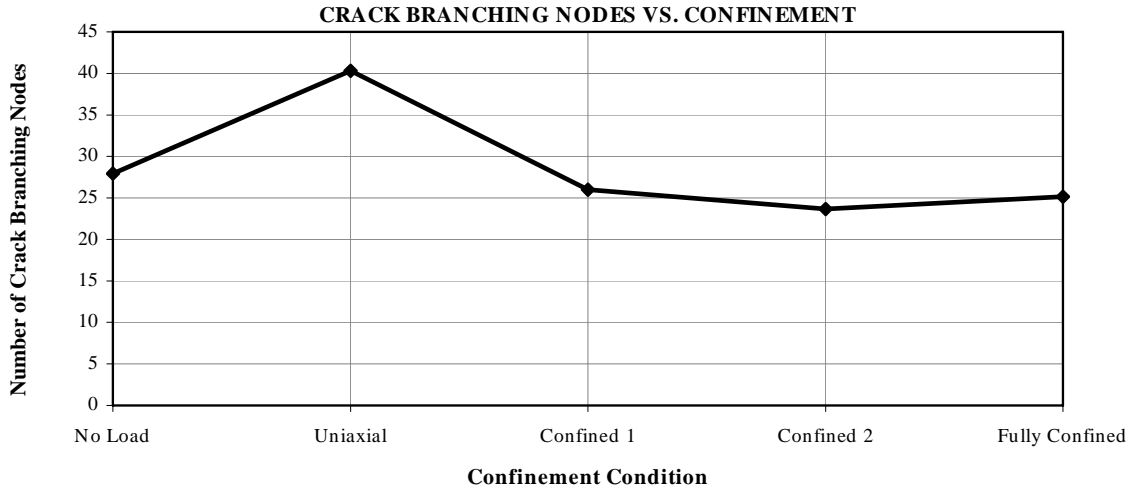


Figure 4.42 Crack-branching nodes as a function of confinement for normal-strength concrete

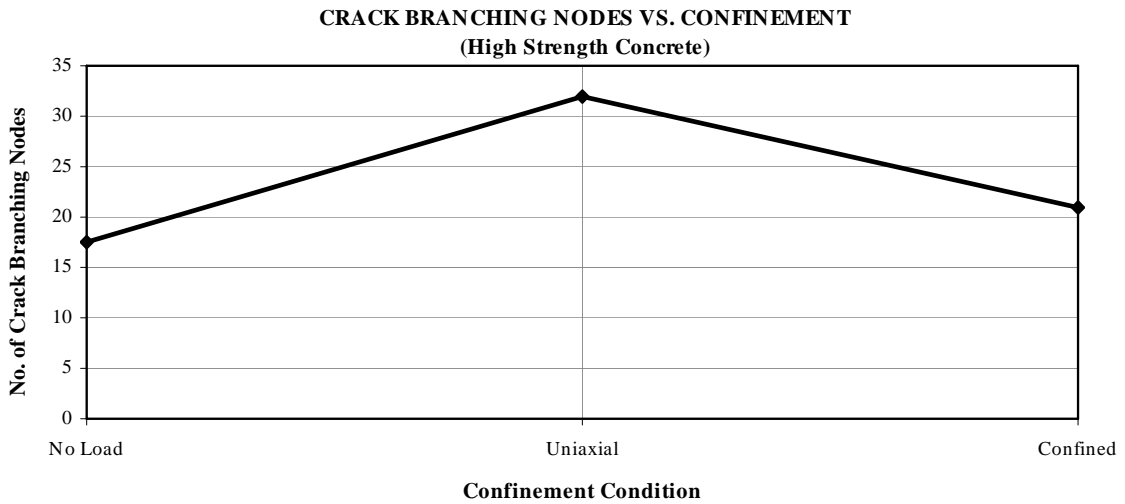


Figure 4.43 Crack-branching nodes as a function of confinement for high-strength concrete

4.7 INTERFACIAL CRACKS

Investigations have shown that very fine cracks at the interface between coarse aggregate and cement paste exist even prior to application of the load on concrete (Hsu et al. 1963). The transition zone, which is the region between hydrated cement paste and coarse aggregate, is a thin shell with a thickness of 10 to 50 μm , and is considered to be weaker than the two main components of concrete: cement paste and aggregate. Crack initiation and propagation are the dominant mechanisms responsible for the nonlinear response of concrete subjected to uniaxial compressive loading. Cracks may initiate in the matrix, aggregates, or in the matrix-aggregate interface.

Interfacial cracks remain stable up to about 30 percent or more of the ultimate strength and then begin to increase in length, width, and number. The overall stress under which they develop is sensitive to the water/cement ratio of the paste. This is the stage of slow crack propagation. At 70 to 90 percent of the ultimate strength, cracks open through the cement paste and bridge the interfacial cracks and the continuous crack pattern is formed (Neville 1981). Because of slow chemical interaction between the cement paste and aggregate, at later ages the transition zone strength improves more than the bulk cement paste strength.

Studies conducted using microscopic analysis (Hsu et al. 1963; Shah and Chandra 1970; Shah and Sankar 1987) have revealed that cracks frequently initiate at the interface and then propagate into the matrix where mortar cracks join to form a continuous crack path prior to ultimate load. In order to analyze the phenomenon of interfacial cracking, an attempt has been made in this section to characterize these cracks. Using advanced computerized imaging, a computer program has been developed to identify interfacial cracks and distinguish them from matrix cracks (see Appendix B). Figure 4.44 shows the flow chart for the computer program.

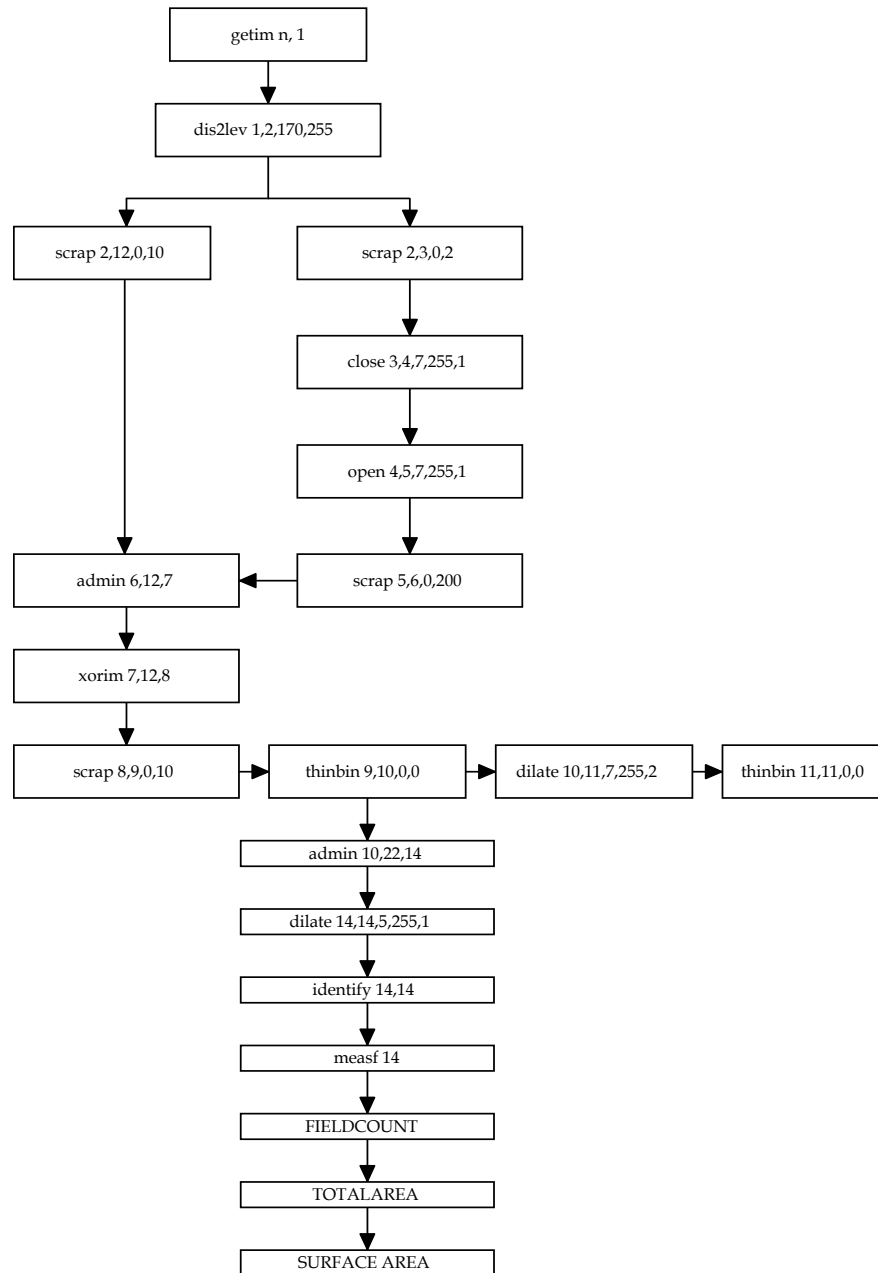


Figure 4.44 The flow chart for interfacial crack identification computer program

The step-by-step procedure for the computer program is outlined below. Figure 4.45 is a SEM image of a concrete specimen which was subjected to a uniaxial loading.

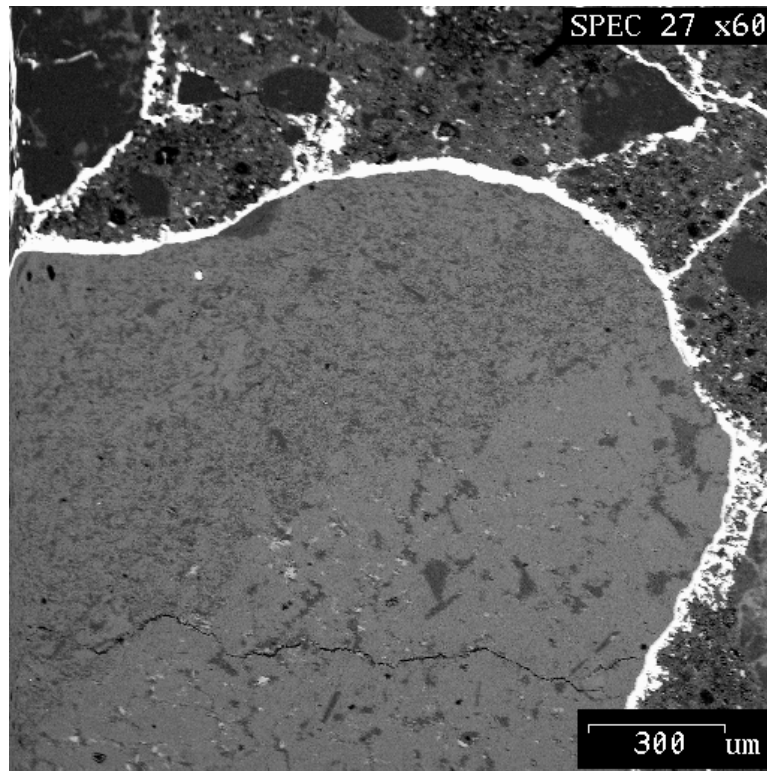


Figure 4.45 Interfacial crack in the normal concrete specimen subjected to uniaxial loading

Using the same criteria outlined in Section 3.4.4 of Chapter 3 for Wood's metal identification, a binary image showing the untreated crack network is produced. In order to eliminate objects on the basis of their area in pixel units, the *scrap* command is invoked for two different *areahigh* values of 2 and 10, indicating the upper limit for the area range (in pixels). Figures 4.46 and 4.47 represent the scraped images of Figure 4.45 with the areahighs of 10 and 2, respectively.

The *close* command first dilates objects in the binary image using a structuring element, defined by shape, i.e. an octagon; it then erodes them, using the same structuring element. This procedure merges adjacent objects. The *close* command is used on Figure 4.47, which produces Figure 4.48.

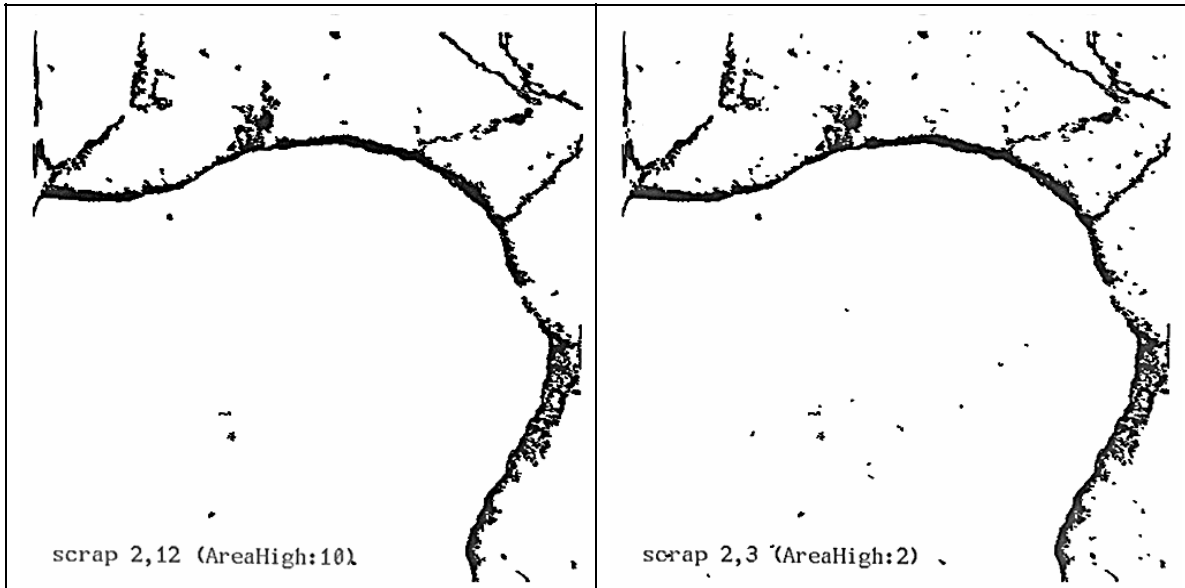


Figure 4.46 Scrap with the higher upper limit for the area range

Figure 4.47 Scrap with the lower upper limit for the area range

The *open* command initially erodes the object in a binary image by means of a structuring element defined by shape, similar to the one used in the *close* command; it then dilates it by means of the same structuring element. This procedure eliminates small objects without strongly affecting larger ones. The *open* command is used on the image in Figure 4.48 to produce Figure 4.49.

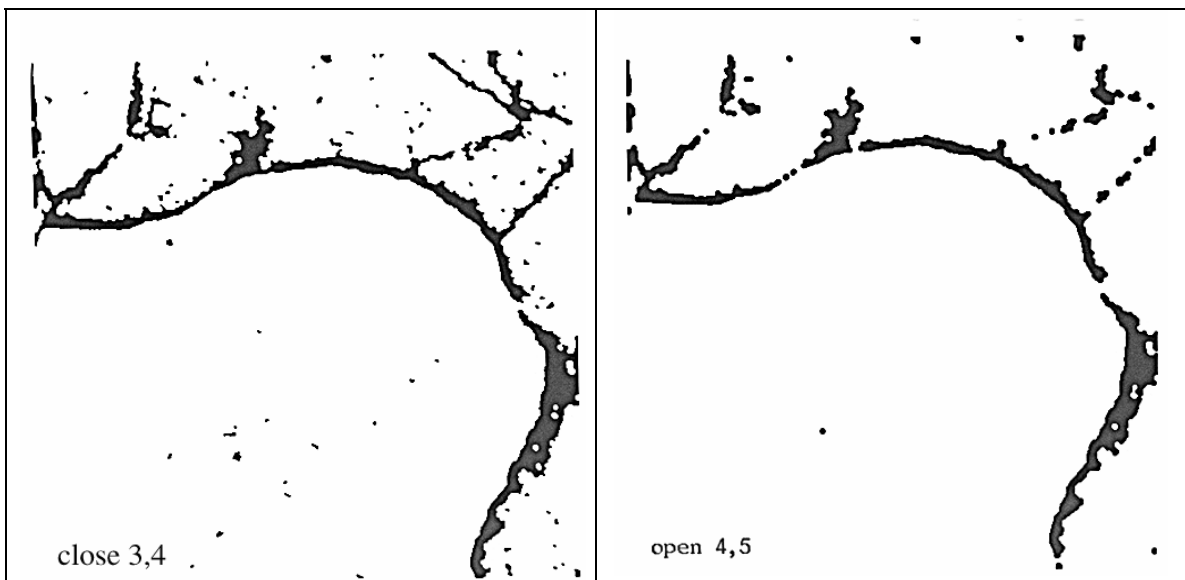


Figure 4.48 Close the image in Figure 4.47

Figure 4.49 Open the image in Figure 4.48

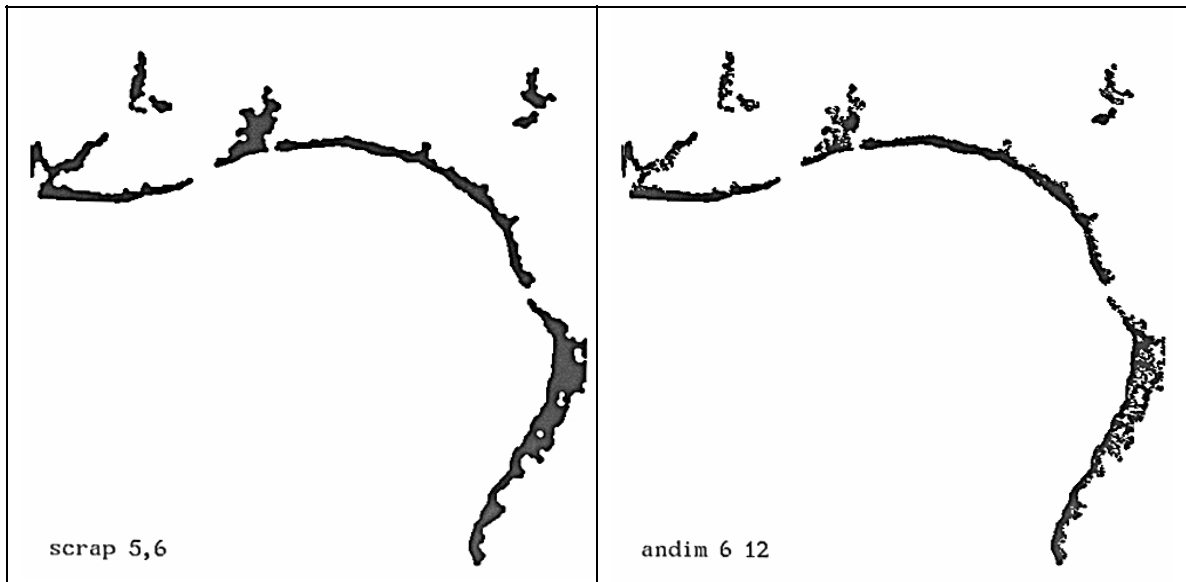


Figure 4.50 Scrap the image in Figure 4.49

Figure 4.51 Correlate every pixel which is both in Figure 4.46 and 4.50

The loose objects in Figure 4.49 are scrapped and Figure 4.50 is produced. At this point every pixel which is both in Figures 4.50 and 4.46 is correlated, which results in the image shown in Figure 4.51. This task is achieved by invoking the *andim* command.

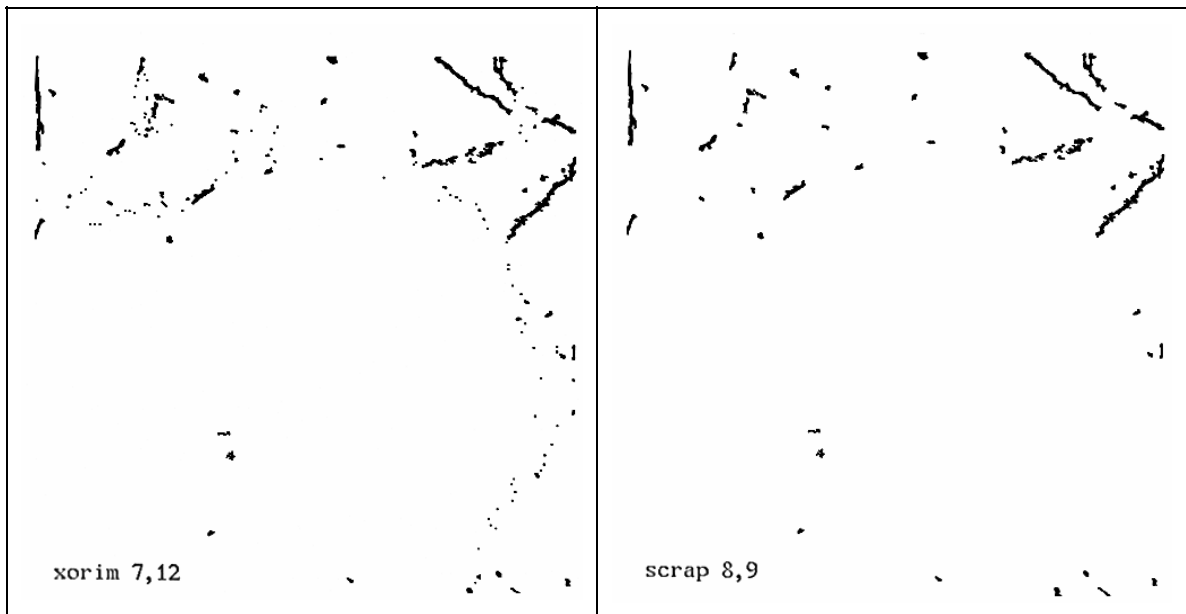


Figure 4.52 Correlating every pixel that is either in Figure 4.46 or 4.49 but not common to them

Figure 4.53 Scrap the image in Figure 4.52

Figure 4.52 is subjected to the *xorim* command. *Xorim* (exclusive or) correlates every pixel that is either in Figure 4.51 or 4.46 but not common to Figure 4.51 and 4.46, and the result is outputted in Figure 4.52. The *scrap* command is applied to the image in Figure 4.52 to produce Figure 4.53.

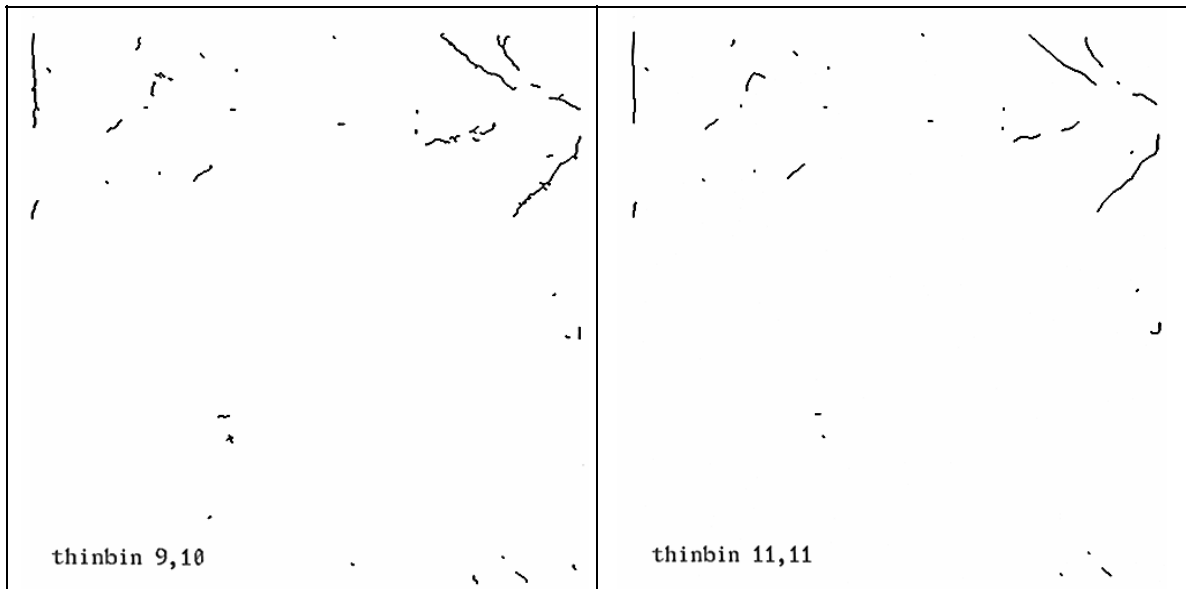


Figure 4.54 Scrap Figure 4.52

Figure 4.55 Crack smoothing of the image in Figure 4.54

Figure 4.53 was subjected to binary thinning and Figure 4.54 is the result. The crack network in Figure 4.54 is dilated and then thinned again to produce Figure 4.55, which is an image of the cracks after they have been smoothed. Figures 4.54 and 4.55 represent the cracks in the concrete matrix, discounting the interfacial cracks. Stereological measurements can be performed on the image in Figure 4.54 to investigate the crack behavior in the cement paste.

Measurements were performed on the total area of the cracks and the area of the interfacial cracks in the SEM images, and the percentage of interfacial cracks obtained is presented in Table 4.5.

Figure 4.56 shows the percentage of interfacial microcracks as a function of the confining stress for normal-strength concrete. As shown, there is a sharp reduction in the amount of interfacial microcracks as the confining stress

increases. The greatest reduction occurred when the concrete specimen was fully confined.

Table 4.5 Percentage of interfacial microcracks

Concrete Type	EXPERIMENT	AREA	I.F. AREA	% AREA
Normal Strength Concrete	No-Load	30569	8510	27.8%
	Uniaxial	68079	17109	25.1%
	Confined 1	73781	17549	23.8%
	Confined 2	47910	9954	20.8%
	Fully Confined	40728	3006	7.4%
High Strength Concrete	No-Load	5885	450	7.6%
	Uniaxial	16283	1103	6.8%
	Confined	3041	204	6.7%

Figure 4.57 shows the percentage of interfacial cracks as a function of confinement for the high-strength concrete specimen. As in normal-strength concrete, interfacial cracks were heavily influenced by the confining stress.

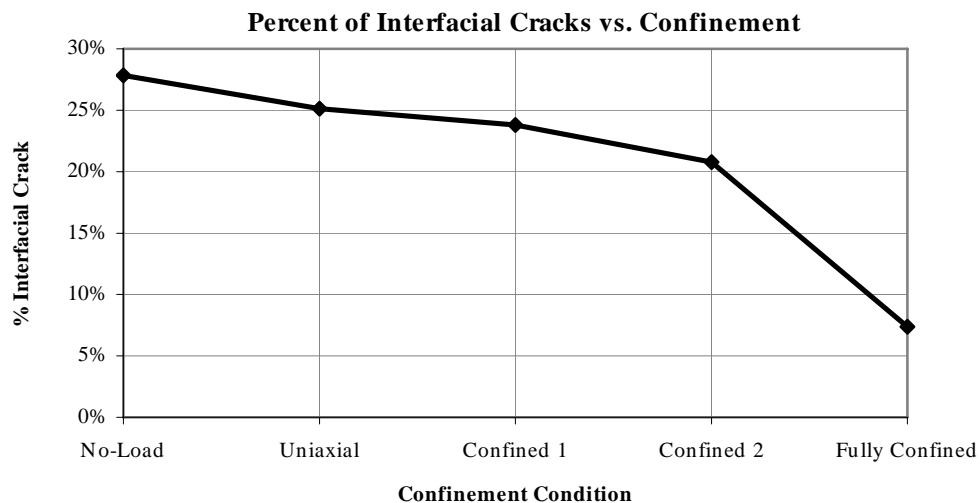


Figure 4.56 Effect of confinement on interfacial microcracks of normal-strength concrete

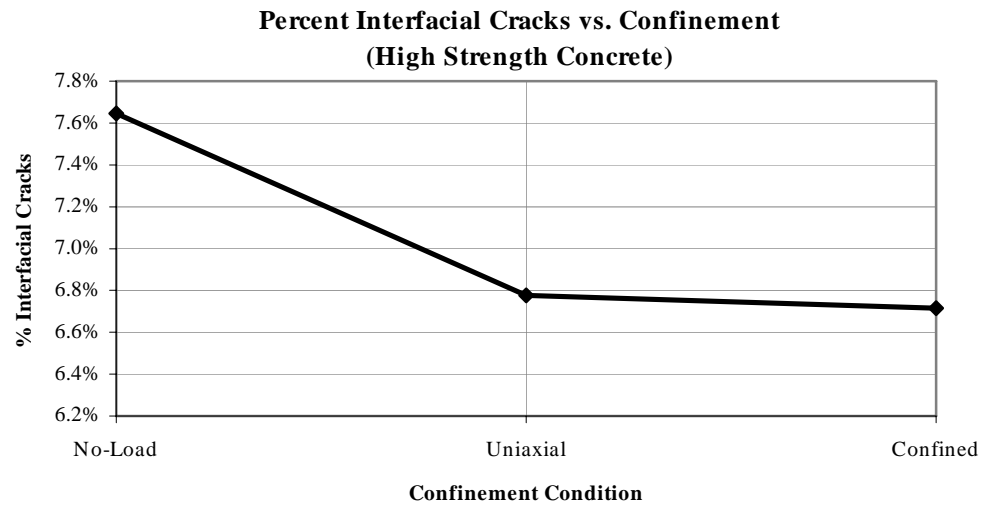


Figure 4.57 Effect of confinement on the interfacial microcracks of high-strength concrete

Chapter 5

MICROMECHANICAL MODELS FOR CONCRETE

5.1 INTRODUCTION

In this chapter three micromechanical models will be examined. The first two models are the differential scheme and the Mori-Tanaka model which predict the elastic modulus after the load is applied. The third model is a crack growth model which predicts the fracture of materials for a given initial pre-load system of cracks and different loading conditions. The experimental results presented in Chapter 4 will be compared to the theoretical models mentioned above.

5.2 ELASTIC MODULUS MODELS

There are several methods of predicting the effective macroscopic elastic moduli of a microscopically heterogeneous material. For the broad class of materials that consist of *inclusions* dispersed in a continuous matrix, the effective moduli depend on the moduli of the two components: the volumetric concentration of the inclusions, and the shape and orientation of the inclusions (Zimmerman 1991). Two of these methods are the differential scheme (McLaughlin 1977; Norris 1985) and the Mori-Tanaka (1973) method. Both models take the microgeometry of the materials into account for estimating the effect of pores and cracks on the elastic moduli. In concrete, the shapes of the inclusions can be estimated by two important idealized pore shapes, namely the sphere and the *penny-shaped* crack (Mehta and Monteiro 1993).

Both of these methods will be applied to predict the elastic modulus of concrete specimens under different loading conditions. The initial elastic modulus of each of the samples is obtainable from the stress-strain diagrams. In each experiment the loads were applied up to 90% of the ultimate strength, and the compressive stress-induced microcracks were preserved by injecting Wood's metal into the specimens while they were under sustained loads. For each experiment, the crack density was determined (see Chapter 4).

5.2.1 DIFFERENTIAL SCHEME

The effective macroscopic elastic moduli of a material can be predicted by means of two-dimensional and three-dimensional differential scheme analysis. Equation 5.1 is based on the two-dimensional analysis proposed by Salganik (1973):

$$E = E_0 e^{-\pi \Gamma_{2D}} \quad (5.1)$$

Equation 5.2 is based on the three-dimensional analysis (Zimmerman 1991):

$$E = E_0 e^{-16 \Gamma_{3D}^9} \quad (5.2)$$

Where: E = Final elastic modulus
 E_0 = Initial elastic modulus
 Γ_{2D} = Crack density in two dimensions
 Γ_{3D} = Crack density in three dimensions

The initial and final moduli of elasticity for Experiment #2, which is a uniaxial test, can be obtained from the stress-strain diagram:

$$E_0 = 2.625 \times 10^6 \text{ psi } (18.1 \times 10^3 \text{ MPa})$$

$$E = 2.375 \times 10^6 \text{ psi } (16.4 \times 10^3 \text{ MPa}).$$

From Table 4.3, the crack density for the uniaxial specimen is, $\Gamma=0.0919$; and for the reference (no-load) specimen, $\Gamma=0.0444$. The effective crack density is the difference between the crack density prior to and after the test. Hence, $\Delta\Gamma=0.0475$.

By applying Salganik's two-dimensional differential scheme solution (Equation 5.1), the final modulus of elasticity can be calculated:

$$E = 2.625 \times 10^6 \times e^{-\pi(0.0475)} = 2.261 \times 10^6 \text{ psi } (15.6 \times 10^3 \text{ MPa})$$

Salganik's method produces a very accurate prediction of the modulus of elasticity, within 5% of the measured value.

Since the crack density measurements were performed in two dimensions, they should be converted to three-dimensional crack density for the three-dimensional differential scheme analysis (similar to Schlueter et al. 1991).

When a plane cuts through a concrete sample, it produces a section which contains line cracks. With respect to two-dimensional measurements, the length of these lines is considered to be the crack length, $2a$. However, in three-dimensional terms, these apparent lengths are not the true measurements of the cracks. Assuming the cracks in three dimensions are idealized to conform to the penny-shaped model shown in Figure 5.1, we can establish the relationship between the lengths of cracks in three dimensions ($2a_{act.}$) and their two dimensional lengths ($2a_{meas.}$).

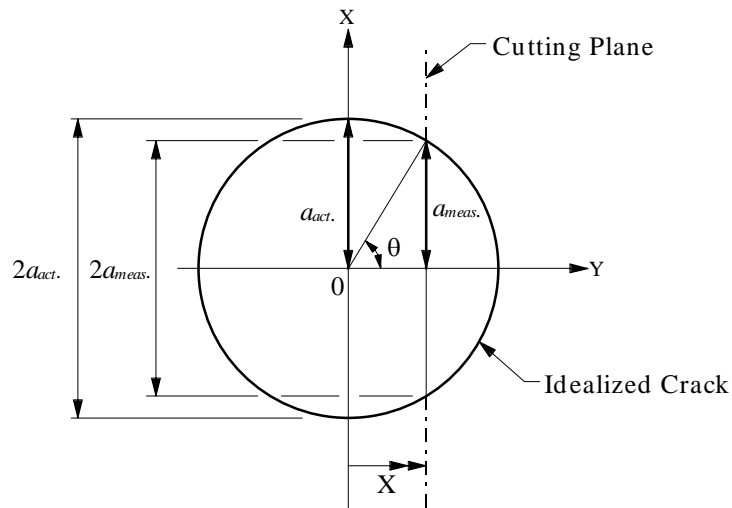


Figure 5.1 Schematic diagram of an idealized crack

For an idealized circular penny-shaped crack, we can write:

$$y^2 + x^2 = a_{act.}^2$$

or

$$y = \sqrt{a_{act.}^2 - x^2} = a_{meas.}$$

The mean value of $a_{meas.}$, $\overline{a_{meas.}}$, can be established from

$$\overline{a_{meas.}} = \frac{\int_0^{a_{act.}} \sqrt{a_{act.}^2 - x^2} dx}{\int_0^{a_{act.}} dx = a_{act.}}$$

Hence

$$\overline{a_{meas.}} = \int_0^{a_{act.}} \sqrt{1 - \left(\frac{x}{a_{act.}}\right)^2} dx$$

let $\frac{x}{a_{act.}} = t$, then $dx = a_{act.} dt$. Substituting in the above equation,

$$\overline{a_{meas.}} = a_{act.} \int_0^1 \sqrt{1 - t^2} dt \quad (5.3)$$

But

$$t = \frac{x}{a_{act.}} = \cos \theta$$

$$t^2 = \cos^2 \theta$$

and

$$1 - t^2 = \sin^2 \theta$$

$$\sqrt{1 - t^2} = \sin \theta$$

Substituting the above in Equation 5.3 will yield:

$$a_{meas.} = a_{act.} \int_0^{\pi/2} \sin \theta \sin \theta d\theta = a_{act.} \int_0^{\pi/2} \sin^2 \theta d\theta = a_{act.} \left(\frac{2\theta - \sin 2\theta}{4} \right) = \frac{\pi}{4} a_{act.}$$

$$a_{act.} = \frac{4}{\pi} a_{meas.} = 1.273 a_{meas.} \quad (5.4)$$

Equation 5.4 gives the actual length of a crack in three dimensional form as derived from the measured length in two dimensions. The two-dimensional and three dimensional crack densities were analyzed, and in some cases a relationship was developed between them (Hadley 1976; Batzle et al. 1980; Abdel-Gawad 1987; and He and Aherns 1994). However, the best result is given by stereological analysis, as explained below.

The number of cracks per unit volume, N_V , can be obtained from the following equation (Underwood 1968):

$$N_V = \frac{2N_A^2}{\pi N_L} \quad (5.5)$$

where N_A represents the number of cracks in two dimensions (Table 4.1) and N_L is the number of intersections of features, i.e. cracks, per unit length of test line (for more detail, refer to Chapter 3).

The crack radius, a , is defined as the ratio of the number of interceptions of features per unit length of test line, N_L , over the number of interceptions of features per unit test area, N_A (Underwood 1968). Therefore,

$$a = \frac{N_L}{N_A} \quad \text{or} \quad N_L = aN_A \quad (5.6)$$

Substituting Equation 5.6 in Equation 5.5 yields:

$$N_V = \frac{2N_A^2}{\pi(aN_A)} = \frac{2}{\pi} \frac{N_A}{a} \quad (5.7)$$

The three dimensional crack density is defined as:

$$\Gamma_{3D} = \frac{Na^3}{V} = N_V a^3 \quad (5.8)$$

substituting Equation 5.7 in Equation 5.8 gives:

$$\Gamma_{3D} = \frac{2N_A}{\pi a} a^3 = \frac{2}{\pi} N_A a^2 = \frac{2}{\pi} \Gamma_{2D} \quad (5.9)$$

Using Equation 5.9, the two-dimensional crack density can be converted to a three-dimensional one. Hence,

$$\Gamma_{3D} = \frac{2}{\pi} \Gamma_{2D} = \frac{2}{\pi} (0.0475)(1.273)^2 = 0.0490$$

The final elastic modulus can be estimated from Equation 5.2:

$$E = 2.625 \times 10^6 \times e^{-16(0.0490)/9} = 2.406 \times 10^6 \text{ psi } (16.6 \times 10^3 \text{ MPa})$$

The three-dimensional analysis result is 2% above the actual measured value. The two-dimensional analysis gives better results.

The initial and final effective moduli of elasticity for Experiment #5, which is a fully confined test, can be obtained from the stress-strain diagram:

$$E'_0 = 1.875 \times 10^6 \text{ psi } (12.9 \times 10^3 \text{ MPa})$$

$$E' = 1.650 \times 10^6 \text{ psi } (11.4 \times 10^3 \text{ MPa}).$$

From Table 4.3, the crack density for the fully confined specimen is, $\Gamma=0.0262$; and for the reference (no-load) specimen, $\Gamma=0.0444$. The effective crack density is the difference between the crack density prior to and after the test. Hence, $\Delta\Gamma=0.0182$.

Applying Salganik's two-dimensional differential scheme solution (Equation 5.1), the final modulus of elasticity can be predicted as:

$$E_{Confined} = 1.875 \times 10^6 \times e^{-\pi(0.0182)} = 1.771 \times 10^6 \text{ psi } (12.2 \times 10^3 \text{ MPa})$$

Salganik's method prediction of modulus of elasticity is within 10% of the measured value.

Converting the two-dimensional crack density into the three-dimensional one, using Equation 5.9 yields:

$$\Gamma_{3D} = \frac{2}{\pi} \Gamma_{2D} = \frac{2}{\pi} (0.0182)(1.273)^2 = 0.0188$$

The final elastic modulus can be estimated from Equation 5.2

$$E_{Confined} = 1.875 \times 10^6 \times e^{-16(0.0188)/9} = 1.813 \times 10^6 \text{ psi } (12.5 \times 10^3 \text{ MPa})$$

The three dimensional analysis result is 9% above the actual measured value.

5.3.1 THE MORI-TANAKA METHOD

Mori and Tanaka (1973) proposed the following equation to predict the elastic modulus of a material containing cracks:

$$\text{Mori-Tanaka method:} \quad E = E_0 / (1 + \beta \Gamma) \quad (5.10)$$

$$\text{where:} \quad \beta = 16(10 - 3\nu_0)(1 - \nu_0^2) / 45(2 - \nu_0)$$

and $\nu_0 = \text{Poisson's ratio}$

For concrete, typically $\nu_0 = 0.20$, so:

$$\beta = 16[10 - 3(0.20)](1 - 0.20^2) / 45(2 - 0.20) = 1.78$$

and for the Mori-Tanaka method:

$$E = \frac{2.625 \times 10^6}{1 + (1.78)(0.0768)} = 2.309 \times 10^6 \text{ psi } (15.9 \times 10^3 \text{ MPa})$$

The modulus of elasticity predicted by the Mori-Tanaka model is within 3% of the measured value. For the fully confined specimen,

$$E_{\text{Confined}} = \frac{1.875 \times 10^6}{1 + (1.78)(0.0182)} = 1.816 \times 10^6 \text{ psi } (12.5 \times 10^3 \text{ MPa})$$

The predicted modulus of elasticity is within 10% of the measured value for the fully confined condition.

Table 5.1 represents the summary of the predicted modulus of elasticity obtained from the differential scheme and Mori-Tanaka method.

Table 5.1 Modulus of elasticity obtained from micromechanical Models

Concrete Specimen	Measured E	2D Differential	3D Differential	Mori-Tanaka Method
Uniaxial	2.375×10 ⁶ psi (15.6×10 ³ MPa)	2.261×10 ⁶ psi (15.6×10 ³ MPa)	2.406×10 ⁶ psi (16.6×10 ³ MPa)	2.309×10 ⁶ psi (15.9×10 ³ MPa)
Confined	1.650×10 ⁶ psi (11.4×10 ³ MPa)	1.771×10 ⁶ psi (12.2×10 ³ MPa)	1.813×10 ⁶ psi (12.5×10 ³ MPa)	1.816×10 ⁶ psi (12.5×10 ³ Pa)

The differential scheme and the Mori-Tanaka model consider the change in the overall moduli when a small increment of the inclusion phase is introduced in a material. The corresponding change in the field variables is neglected by the Mori-Tanaka model, whereas in the differential scheme the change in the field variables is related to the change of the volume fraction of the inclusion. It has been shown that, as the volume fraction goes to zero, the two methods agree asymptotically, although their specific predictions may be different, depending on the problem (Nemat-Nasser and Hori 1993).

5.3 CRACK GROWTH SIMULATION MODEL

Du (1994) has developed a micromechanical model by which, given the initial crack conditions in an unloaded specimen, the final cracking state can be predicted for different loading conditions. The experimental results obtained and discussed in Chapter 4 will be compared to the theoretical results obtained using Du's crack-growth model.

Du's model employs three commonly used fracture criteria. They are:

- a) The maximum stress criterion, σ -criterion;
- b) The maximum energy release rate criterion, G -criterion;
- c) The minimum strain energy density criterion, S -criterion.

The criterion most commonly used for concrete is the maximum energy release rate criterion.

5.3.1 The Maximum Energy Release Rate Criterion, G -Criterion

The energy release rate is usually defined as the energy released from the body per unit crack advance. A more precise definition (Moran and Sih 1987) involves the work input into the crack tip. Irwin (1956) defined an energy release rate, G , which is a measure of the energy available for an increment of crack extension. Considering the plate, shown in Figure 5.2, with a thickness B , and containing a crack with a length of $2a$.

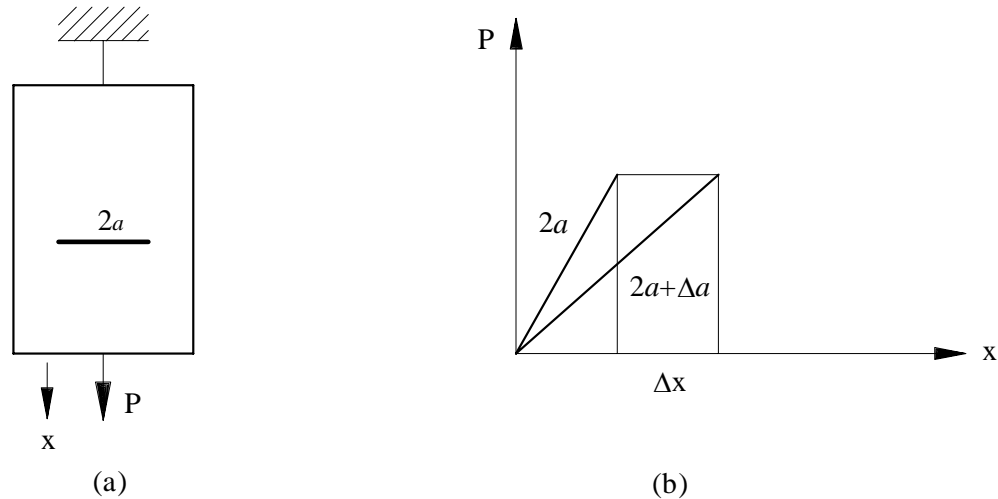


Figure 5.2 (a) Plate with crack $2a$; (b) Load-displacement diagram

If the plate is subjected to a constant load P , the energy released can be expressed by crack growth Δa as (Mehta and Monteiro 1993):

$$GB\Delta a = P\Delta x - \Delta U_e$$

where ΔU_e is the change in elastic energy due to crack growth Δa . In the limit:

$$GB = P \frac{dx}{da} - \frac{dU_e}{da} \quad (5.11)$$

the strain energy U_e in terms of compliance is given by:

$$\Delta U_e = \frac{cP^2}{2}$$

and Equation 5.11 becomes:

$$G = \frac{P^2}{2B} \frac{dc}{da} \quad (5.12)$$

Where: G = energy release rate
 P = applied load
 B = plate thickness
 c = compliance (displacement/load)
 a = half-crack length

Irwin (1957) defined the quantity G_c as the work required to produce a unit increase in crack area, referred to as *critical energy release rate*. G_c is a material property and is determined experimentally. In order to determine whether or not a crack will propagate, the value of energy release per unit increase crack area, G , is computed. If the energy release rate is lower than the critical energy release rate ($G < G_c$), the crack is stable. Conversely, if $G > G_c$, the crack will propagate. A condition in which the energy release rate equals the critical energy release rate ($G = G_c$) is known as metastable equilibrium.

The stress intensity factor, K_I , is defined as:

$$K_I = \sigma \sqrt{a} f(g) \quad (5.13)$$

Where: K_I = stress intensity factor for mode I (stress $\sqrt{\text{length}}$)
 σ = applied stress
 $f(g)$ = a function depending on the specimen and crack geometry

These two parameters, the energy release rate and the stress intensity factor, describe the behavior of cracks. The former quantifies the net change in potential energy that accompanies an increment of crack extension; the latter characterizes the stresses, strains, and displacements close to the crack tip. The energy release rate describes global behavior, whereas the stress intensity factor is a local parameter. For linear elastic materials, K_I and G_c are uniquely related. Considering only mode I and plane stress condition, for linear elastic behavior:

$$G = \frac{K_I^2}{E} \quad (5.14)$$

The *critical stress intensity factor*, K_{Ic} , commonly known as *fracture toughness*, is assumed to be a material property.

The G -criterion, usually called the maximum energy release rate, states that:

- a) Crack initiation takes place at the crack tip and in a direction with respect to the original crack plane.
- b) Crack extension takes place in the direction along which the strain energy release rate is maximum.
- c) Crack initiation occurs when the maximum strain energy release rate in a direction reaches a critical value.

5.3.2 Crack Growth and propagation

The Du model uses the displacement discontinuity method which allows the fracture mechanics parameters to be readily computed for a given crack problem. By assuming a virtual crack increment, the crack initiation direction can be determined by one of the three fracture initiation criteria discussed in the previous section. The crack propagation path can be determined by assuming several crack increments. After each crack increment, the computer program recalculates the fracture parameters and the corresponding initial angle of crack propagation is determined. Figure 5.3 is the flow chart of the Du model computer program.

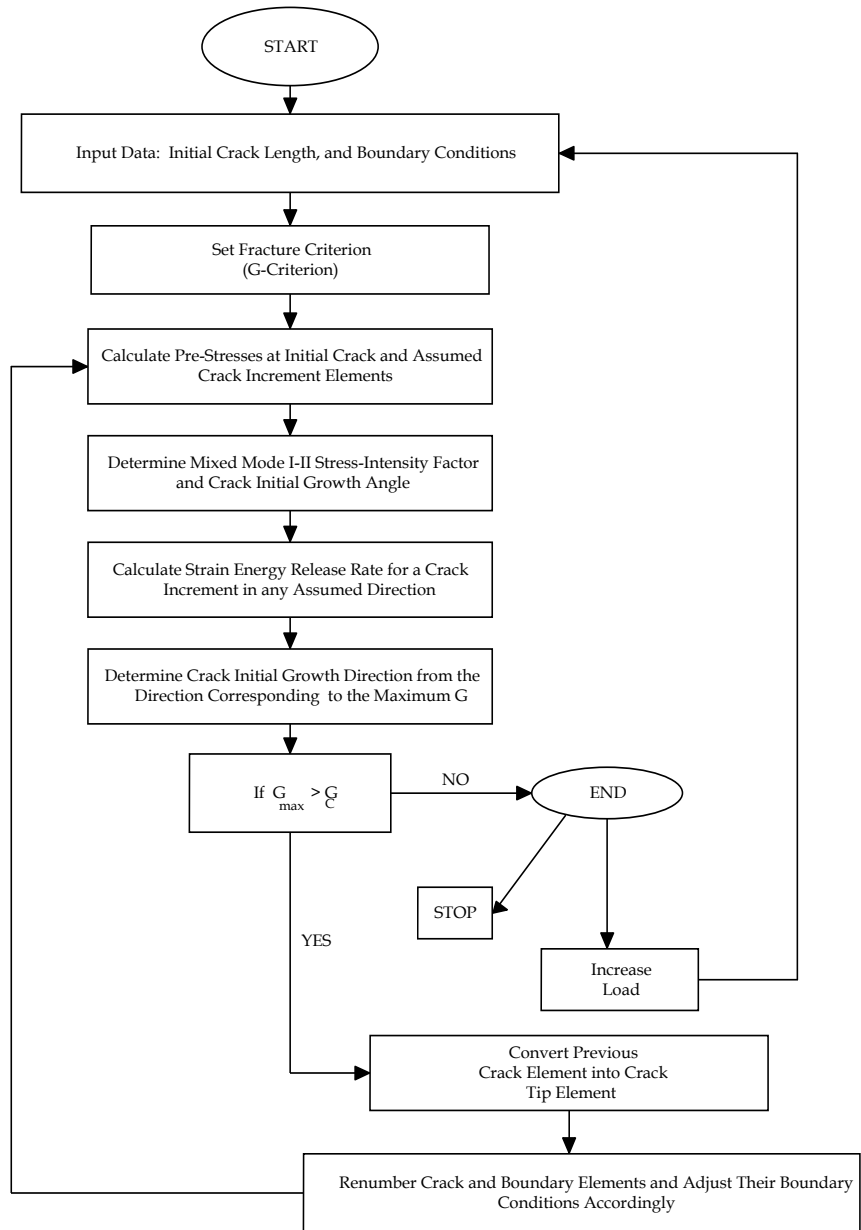


Figure 5.3 Computer flow chart for the Du model calculations

5.3.3 Review of Analytical Micromechanical Model

The purpose of the Du model is to numerically simulate the behavior of stochastic distributions of heterogeneous microcracks. This behavior is difficult to model using analytical models. Du's micromechanical model is based on the idea that frictional sliding along pre-existing cracks results in the formation of tension cracks at their tips. The basis for the model is the *displacement discontinuity model* of Crouch and Starfield (1983). This model is based on the analytical solution to the problem of a constant discontinuity in displacement over a finite line segment in the x,y plane on an infinite elastic solid. A displacement discontinuity can be visualized physically as a line crack whose opposing surface have been displaced relative to one another. In the case under consideration here, surfaces are displaced relatively by a constant amount along the entire crack. However, in general, one could consider an arbitrary distribution of relative displacement.

This method is based on the notion that one can make a discrete approximation of a continuous distribution of displacement discontinuity along a crack. That is, a crack can be divided into a series of N elements (boundary elements) and the displacement discontinuity assumed to be constant over each one. On the basis of the analytical solution for a single, constant element displacement discontinuity, we derive a numerical solution to the problem by summing up the effects of all N elements. When the distribution of displacement discontinuity along the crack is not known, the distribution of traction applied to the crack surfaces must be known in order to define the problem properly. The values of the element displacement discontinuities necessary to produce these tractions, are then sought, element by element along the crack (Crouch and Starfield 1983).

5.3.4 Distribution of Microcracks in the Material

The microcracks yielded by Experiment #1, the no-load experiment, were used as the initial input microcracks in the Du model. Figure 5.4 is the histogram of the microcracks in that experiment.

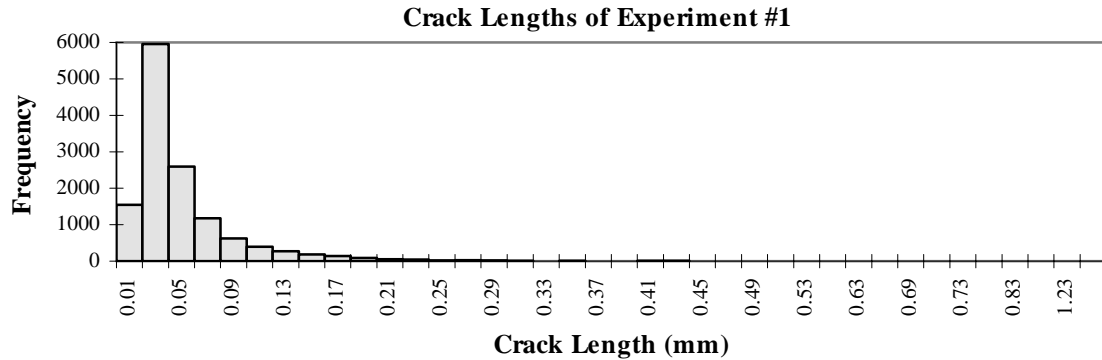


Figure 5.4 Histogram of entire microcrack length distribution for the no-load experiment on normal-strength concrete

Table 5.2 is the tabulation of the microcracks used in the model.

Table 5.2 The microcrack lengths used in the Du model

NORMAL-STRENGTH CONCRETE	
Crack Length (mm)	Frequency
0.4	26
0.5	18
0.6	4
0.7	4
0.8	3
0.9	1
1.0	1
1.3	1
1.5	1
Total	59

Crack lengths smaller than 0.4 mm are ignored and, because crack apertures are negligibly small, line cracks were assumed.

The Du model uses the Monte Carlo technique to generate a distribution of line cracks. Monte Carlo simulation is used for problems involving random variables with known (or assumed) probability distribution.

Because of the assumption of a uniformly random distribution of initial crack locations and orientation, an algorithm has been developed to generate a similar distribution. For each crack generated, three random numbers are initially picked to determine the crack position (x,y) , orientation, and according to Table 5.2, a non-random crack generation is implemented to generate a distribution of crack length L (Kemeny 1991). The crack orientations are between 0° and 90° . A tree-cutting algorithm is used to eliminate cracks that intersect. Figure 5.5 is an illustration of the cracks generated in a concrete specimen with rectangular boundaries.

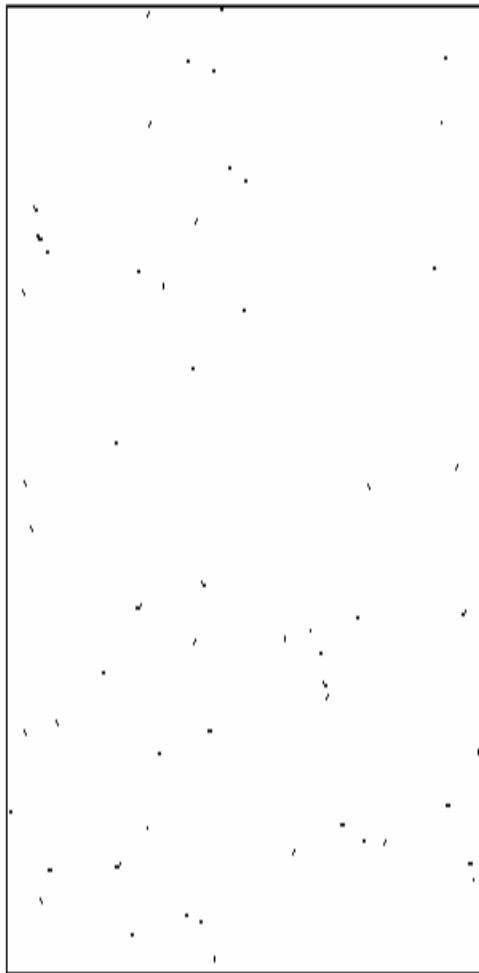


Figure 5.5 The random cracks generated in concrete specimen

5.3.5 Parameters Used in the Crack Growth Model

The CEB-FIP model code 1990 recommends the use of the following expression for the energy release rate:

$$G_f = \alpha_f (f_{cm} / f_{cmo})^{0.7} \quad (5.15)$$

where α_f is a coefficient which depends on the maximum aggregate size d_{max} , which for 3/8 inch (10 mm) MSA is 0.02 Nmm/mm², and f_{cmo} is equal to 10 MPa (Mehta and Monteiro 1993). f_{cm} is the average 28-day compressive strength. The strength data that is available is the strength after more than 2 years (840 days). In order to obtain the 28-day compressive strength of the concrete specimen, the CEB-FIP model code (1990) suggests the following relationship:

$$f_{cm}(t) = \exp \left[s \left(1 - \left(\frac{28}{t/t_1} \right)^{1/2} \right) \right] f_{cm} \quad (5.16)$$

where $f_{cm}(t)$ = mean compressive strength at age t days

f_{cm} = mean 28-day compressive strength

s = coefficient depending on the cement type, such as $s=0.25$ for normal hardening cement

t_1 = 1 day

$$51.7 \text{ MPa (7,500 psi)} = \exp \left[0.25 \left(1 - \left(\frac{28}{840} \right)^{1/2} \right) \right] f_{cm}$$

$$f_{cm} = 42.14 \text{ MPa (6,100 psi)}$$

By substituting in equation 5.15,

$$G_f = (0.02 \times 10^3 \text{ Nm}^{-1}) \left(\frac{42.14 \text{ MPa}}{10 \text{ MPa}} \right)^{0.7} = 54.7 \text{ Nm}^{-1}$$

Irwin (1957) showed that the energy release rate and the stress intensity factor approaches are equivalent. For linear elastic behavior, considering only mode I and plane stress condition:

$$G_I = \frac{K_I^2}{E} \quad (5.17)$$

For $E=2.625 \times 10^6$ psi (18.1 GPa),

$$K_I = \sqrt{G_f \cdot E} = \sqrt{(54.7 \text{ Nm}^{-1})(18.1 \times 10^9 \text{ Pa})} \approx 1 \text{ MPa}\sqrt{\text{m}}$$

A Poisson's ratio, ν , value of 0.2, and a coefficient of friction, μ , value of 0.35 are assumed for the concrete specimen. The representative parameter values for the concrete specimen are shown in Table 5.3:

Table 5.3 Material properties for Concrete specimen

Crack Orientation	Random
Crack Location	Random
Crack Length, $2a$	0.4-1.5 mm
Poisson's Ratio, ν	0.2
Young's Modulus, E	18.1 GPa
Fracture Toughness, K_{IC}	1 MPa $\sqrt{\text{m}}$
Crack Density, Γ	0.0444
Friction Coefficient, μ	0.35
Crack Initial Angle, θ	4.9°

All representative parameter values for concrete were taken from Table 5.3 except the crack lengths which were taken from Table 5.2. Figure 5.6 shows the concrete specimen's cross section with the boundary dimensions for the input algorithm.

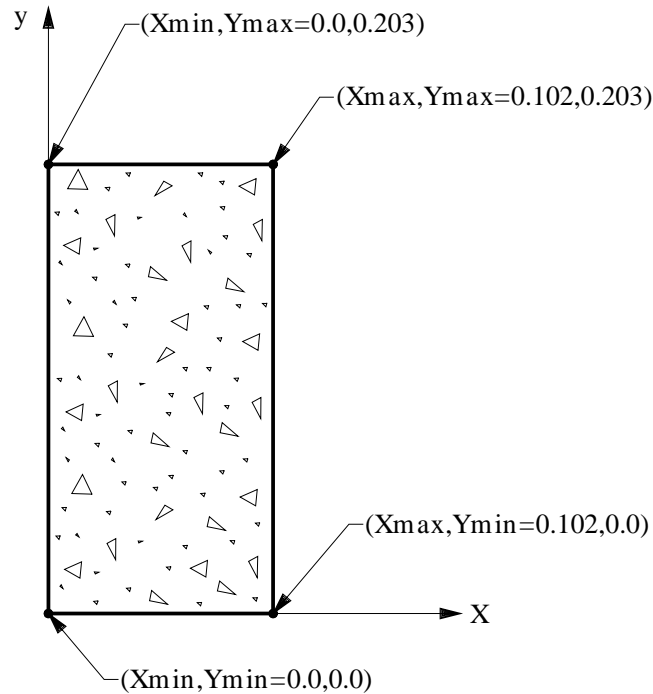


Figure 5.6 Concrete specimens boundary input in algorithm

The algorithm above generates the crack pattern, which represents the preload cracking status.

5.3.6 Program Overview

As mentioned earlier, the Du model was developed by making a series of modifications to the code of the displacement discontinuity method of Crouch and Starfield (1983). The computer program is called MCP (Multiple Crack Propagation Program). It is a two dimensional boundary element code which simulates the multiple crack growth, interaction, and coalescence in materials. MCP is a command-driven (rather than menu-driven) computer program.

The input file is prepared from the rectangular boundary of the concrete specimen's cross section, shown in Figure 5.7, and its information is kept in a file named *Bouninput.dat1*.

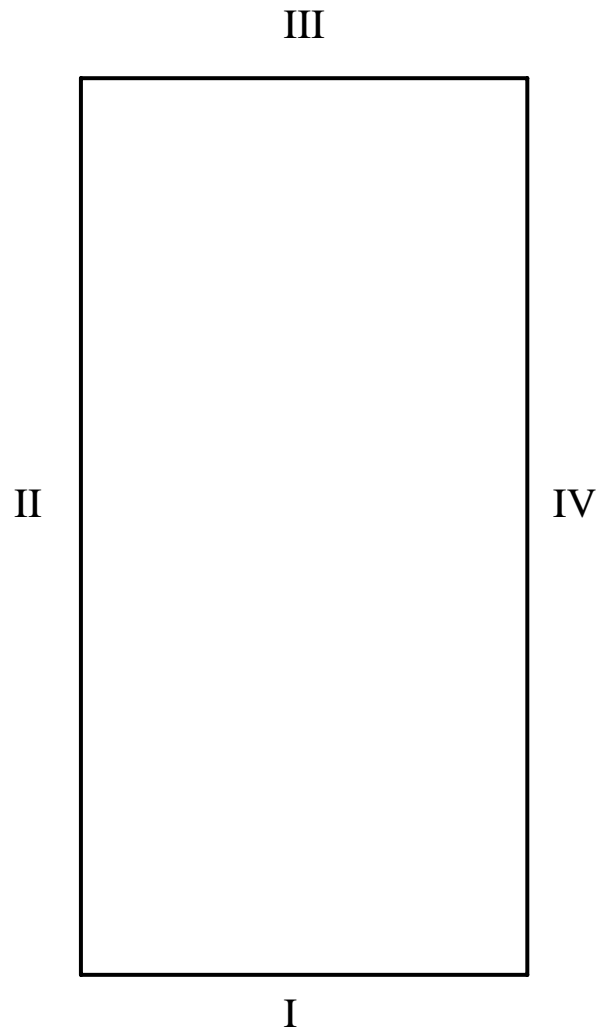


Figure 5.7 Rectangular boundary

The parameters which are read into the program from *Bouninput.dat1* are:
Numbs, Xlow, Ylow, Xlow, Yhigh, An low, An high, Kode, BVS, BVN, Al low, Al.high.

Where *Numbs* = number of straight line boundary segment used to define boundary contours.

(X_{low}, Y_{low}) and (X_{high}, Y_{high}) are the beginning and ending coordinates of boundaries I, II, III, IV.

$Kode = 1$ indicates that σ_s and σ_n are prescribed.

$BVS =$ resultant shear strength (σ_s) or shear displacement (u_s)

$BVN =$ resultant normal-strength (σ_n) or normal displacement (u_n)

$An_{low} =$ minimum angle = 0°

$An_{High} =$ maximum angle = 180°

$Al_{low} =$ minimum crack length

$Al_{High} =$ maximum crack length

For program running procedures, refer to Appendix B.

5.3.7 The Crack Growth Simulation Model Results

Using the random crack distribution shown in Figure 5.5, and employing the Du model, with the axial displacement of 0.00001 meters for 50 iteration, will produce the image shown in Figure 5.8. The material properties used are tabulated in Table 5.3. The material in the model was subjected to an axial strain of 0.25%.

$$\left(\varepsilon_a = \frac{(0.00001 \text{ meter})(50 \text{ iterations})}{0.203 \text{ meter}} = 0.0025 = 0.25\% \text{ strain} \right)$$

The crack density in Figure 5.8 was measured to be $\Gamma_{uniaxial} = 0.2173$.

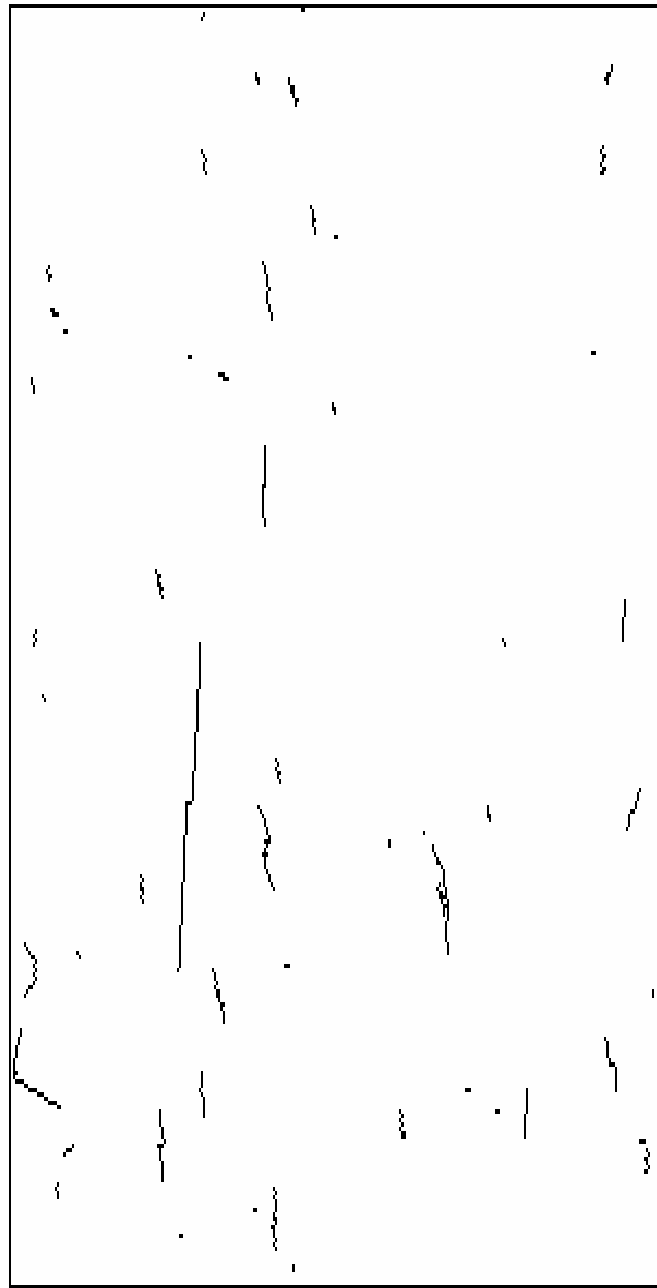


Figure 5.8 Crack propagation simulation for uniaxial loading

The same no-load model in Figure 5.5 was then subjected to a confined test, with the same number of iteration and axial strain. The result is shown in Figure 5.9. It is evident that the number of cracks propagating from the original cracks, and also the number of post-load generated cracks was reduced. The resulting

crack density was measured to be $\Gamma_{confined} = 0.1878$. There was about 15% reduction in crack density due to presence of confining stress.

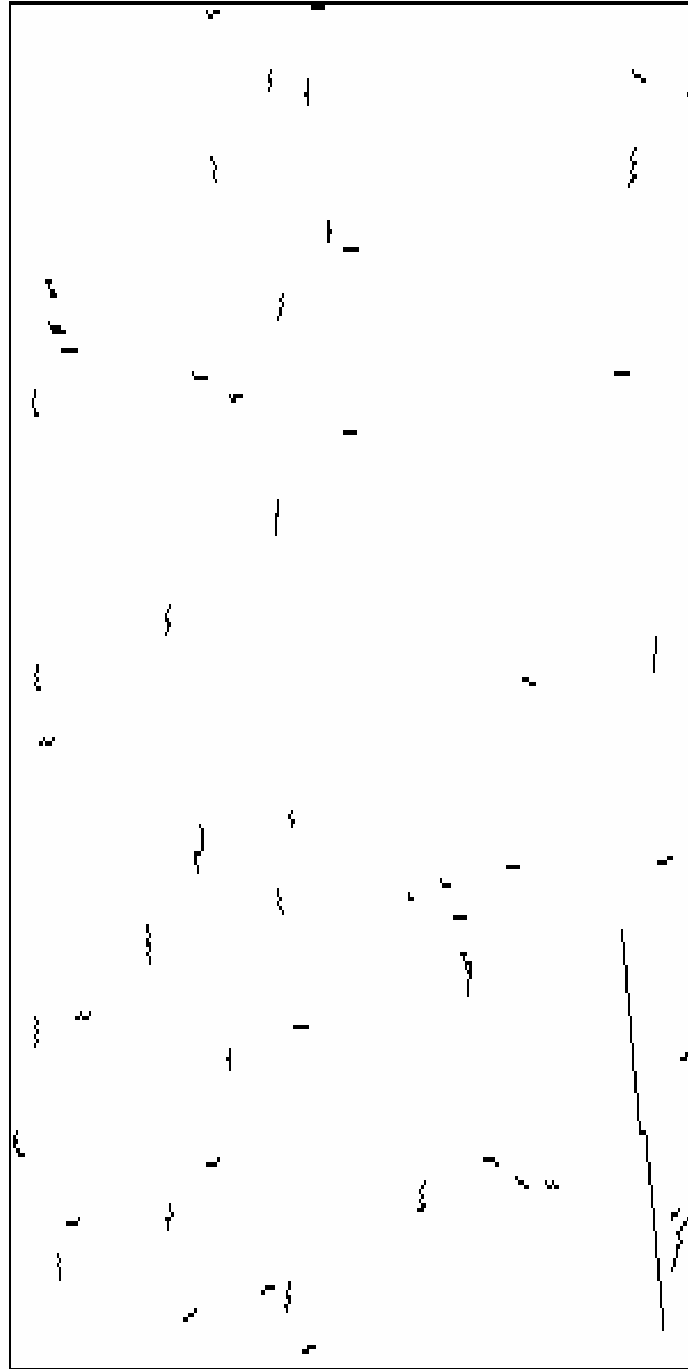


Figure 5.9 Crack propagation simulation for fully confined condition

The Du model results are consistent with the experimental results which were presented in Chapter 4. The experimental results showed that the crack density reduced when confining stress was used. The Du model also showed the same behavior. Experimental measurements indicated that the average crack length distribution strongly depends on the confining stress. The results obtained from the Du model, also indicates that the average crack length decreased when confinement was used. Most cracks in the Du model have an orientation subparallel to the direction of maximum applied stresses. The definite crack orientation in the Du model is due to the fact that there are no aggregates in the model and it is similar to testing a mortar specimen. The application of the Du model to concrete crack growth simulation should be enhance to include hard inclusions, i.e. aggregates, in the model.

Chapter 6

SUMMARY, CONCLUSION, AND RECOMMENDATIONS

6.1 SUMMARY OF WORK PERFORMED

As a central part of this study, a special experimental technique was developed which made possible the preservation of the compressive stress-induced microcracks in concrete as they exist under applied loads. This technique involved injecting a molten-metal alloy into the induced cracks and solidifying it before unloading.

A total of eight experiments were performed, five on normal-strength, and three on high-strength concrete specimens. The specimens were loaded up to 90% of their ultimate strength. For the normal-strength concrete specimens, a no-load experiment was conducted initially to determine the fracture status of the specimen prior to loading. In the second experiment, the specimen was subjected to uniaxial compression. The third and fourth experiments were partially confined experiments. Confining stress was used to generate triaxial compression and was supplied by stainless steel wires wound around the concrete specimens. In the partially confined experiments, the wire was wound one-third of the way from each end of the specimen. The fifth experiment used a fully confined specimen which had wire wound around its entire length. The experiments on the high-strength concrete specimens were no-load, uniaxial, and partially confined experiments.

After each experiment, four specimens, parallel to the direction of maximum applied stresses, were extracted from the concrete cylinders. These specimens were polished and prepared for scanning electron microscope (SEM) observations. Fifty five images were taken from each specimen, bringing the total number of images to over 2,220. The images were analyzed by an advanced-computerized image analyzer.

The concept of stereology, which deals with the interpretation of three-dimensional structures by means of their two-dimensional sections, was applied to analyze the images. Two-dimensional measurements were also performed to determine crack length and orientation. The experimental results obtained were also compared to some of the existing micromechanical models.

6.2 SUMMARY OF FINDINGS AND CONCLUSIONS

Concrete has the inherent quality of being heavily cracked even before a load is applied. When concrete specimens were subjected to compressive loading, microcracks were generated by several different mechanisms and had an orientation that was generally within 15 degrees of the direction of the maximum compression. The microcracks observed were generally short. The average crack length was from 49.6 microns for the fully confined specimen, to 51.8 microns for the uniaxial specimen. Microcrack orientation, density, length, and branching were strongly influenced by the amount of confining stress to which they were subjected. The average orientation of the microcracks, which was computed from the absolute values of angles from the vertical--i.e., the direction of maximum compression--increased as the confining stress increased. The microcrack density distribution, which represents the number of microcracks per unit of observation area, decreased as the confining stress increased. The specimen subjected to uniaxial compression had the highest crack density, and the specimen loaded under fully confined condition had the lowest value. In the partially confined specimens, the crack length and density were observed in both confined and unconfined portions of the specimen. The crack densities in the center and edge were smaller in the confined portion than in unconfined portion. The number of cracks per observer area also decreased with confinement. The surface area of the crack, S_v , which is a stereological measurement, was strongly influenced by the confining stress; and as the confining stress increased, crack surface area decreased. Crack lengths were also assessed stereologically, and they showed that with increasing confinement, crack lengths decreased. Similar behavior was observed with the percent crack area measurements and in terms of the absolute number of cracks per unit of observed area. The average length was longest in the uniaxial experiment, and shortest in the fully confined experiment. In the partially confined specimens, both the crack length and

density in the center and edge of the sample were smaller in the confined portion than in the unconfined portion. In the same specimens, the average crack length was smaller in the center portion of the specimen than along the edge. As the confinement increased, crack branching in the specimens decreased. The number of branching nodes in the normal-strength concrete was much higher than in the high-strength concrete. As high-strength concrete is more brittle, fracture in high-strength concrete is associated with less branching than in normal-strength concrete. Interfacial cracks, the cracks in the interface of aggregate and cement paste, were strongly influenced by the amount of confinement. Interfacial microcracks decreased as the amount of confinement increased.

Three micromechanical models were used to compare the experimental results against the theoretical models. They were: the differential scheme, the Mori-Tanaka model, and a crack-growth simulation model. The first two models determine the final modulus of elasticity of a material, based on its initial modulus and the crack density. The final modulus of elasticity was computed on the basis of the initial modulus of elasticity, obtained from the stress-strain diagram, and the measured crack densities. They were in close agreement with the measured modulus at the end of the experiments. The analysis in the differential scheme was performed in both two and three dimensions. The uniaxial and fully confined specimens were compared to the theoretical models. The predicted elastic moduli were in agreement with the measured values, and the differences varied between 2 and 8 percent. The crack growth simulation model used the initial pre-load crack pattern and the elastic constants of the concrete specimens to generate crack growth with increasing compressive loads. As with the previous models, the uniaxial and fully confined specimens were examined against the crack growth model. The differences in crack densities obtained from the crack growth model for the uniaxial and fully confined loadings were identical to the results obtained from the experiments.

The molten-metal-injection technique used in this research is an efficient, cost effective, and reliable method for the preservation of microcracks in concrete as they exist under load.

6.3 RECOMMENDATIONS FOR FUTURE RESEARCH

Using the molten-metal-injection technique, it is possible to observe crack propagation in concrete under compressive loading. The concrete specimens should be loaded at 20% increments of their ultimate strength up to the failure of the sample. This way, crack length, density, orientation, and interaction can be observed at different stages of loading; and the propagation of cracks can be quantified with the increase in load.

The molten-metal-injection technique should be extended to structural lightweight concrete in order to study the fracture of the aggregates in concrete. Lightweight aggregate concrete is made with lightweight-cellular aggregates so that its unit weight is less than normal-weight concrete. In lightweight aggregate concrete, fracture passes through the cellular aggregate particles because both the transition zone and the cement paste are generally stronger, whereas in normal-weight concrete, since the aggregate particles are dense and strong, fracture is usually in the transition zone or the bulk cement paste, not through the aggregate.

Another potential application of the molten-metal-injection technique is to the study of concrete made with pozzolanic materials. Pozzolans are siliceous, or siliceous and aluminous, materials. When added to the concrete mix, they greatly enhance the properties of concrete. Concrete made with pozzolans are generally stronger and more durable. Using the molten-metal-injection technique, the effects of different kinds of pozzolanic materials on the micromechanical behavior of concrete could be investigated. This could prove to be a very useful study.

Air voids in concrete, either of the entrapped or entrained type, are capable of adversely affecting its strength and permeability. The Wood's metal technique could be employed to quantify the porosity of concrete and to study the effect of air voids on the overall behavior of the material.

The type and size of aggregates used has a great effect on the strength and behavior of concrete. The smaller the aggregate, the stronger the concrete. The molten-metal-injection technique can be used to study the effects of different types and sizes of aggregates on fracture of concrete.

The design of the cell apparatus should be modified to develop an apparatus capable of testing concrete in tension, i.e. 3-point load or the Brazilian test. Tensile cracks could then be preserved as they exist under load, and their behavior analyzed.

The crack simulation growth model used in Chapter 5 does not take aggregates into account. A viable model for crack growth in concrete should incorporate aggregates into the simulation. This could be achieved by randomly distributing pockets of a higher modulus within the modeled matrix to simulate the aggregates in concrete.

REFERENCES

- Abdel-Gawad, M., Bulau, J., and Tittman, B. (1987). "Quantitative Characterization of Microcracks at Elevated Pressure." *Journal of Geophysical Research*, 92(B12), 12911-12916.
- ACI Committee 363 (1984). "State of the Art Report on High Strength Concrete." *ACI Journal*, 81(4), 364-411.
- Anderson, T. L. (1991). *Fracture Mechanics Fundamentals and Applications*, CRC Press, Boca Raton, Florida.
- "Standard Test Methods for Microscopical Determination of Parameters of the Air-Void System in Hardened Concrete: ASTM C 457-90." (1993). *ASTM annual book of standards*, 4.02, Concrete and Aggregates, ASTM, Philadelphia, Pa. 234-246.
- Barquins, M. and Petit, J. P. (1992). "Kinetic instabilities during the propagation of a branch crack: effects of loading conditions and internal pressure." *Journal of Structural Geology*, 14(8/9), 893-903.
- Batzle, M. L., Simmons, G., and Seigfried, R. W. (1980). "Microcrack Closure in Rocks Under Stress: Direct Observation." *Journal of Geophysical Research*, 85(B12), 7072-7090.
- Buyukozturk, O., Nilson, A. H., and Slate, F. O. (1971). "Stress-Strain Response and Fracture of Concrete Model in Biaxial Loading." *Journal of American Concrete Institute, Proceedings*, 68(5), 590-599.
- Buyukozturk, O., Nilson, A. H., and Slate, F. O. (1972). "Deformation and Fracture of a Particulate Composite." *Journal of Engineering Mechanics Division, Proceedings of American Society of Civil Engineers*, 98(EM3), 581-593.

- Carino, N.J. and Slate, F. O. (1976). "Limiting Tensile Strain Criterion for Failure of Concrete," *Journal of American Concrete Institute, Proceedings*, 73, 160-65.
- Carrasquillo, R. L., Nilson, A. H., and Slate, F. O. (1981). "Properties of High Strength Concrete Subject to Short-Term Loads," *ACI Journal*, 78(3), 171-178.
- Carpinteri, A. and Ingraffea, A. R. (1984). *Fracture Mechanics of Concrete: Material Characterization and Testing*, Martinus Nijhoff Publishers, The Hague.
- Carrasquillo, R. L., Nilson, A. H., and Slate, F. O. (1981). "Properties of High Strength Concrete Subject to Short-Term Loads," *ACI Journal*, 171-178.
- Chen, W. F. (1982). *Plasticity in Reinforced Concrete*, McGraw-Hill Book Company, New York, 30-33.
- Crouch, S. L. and Starfield, A. M. (1983). "Boundary Element Method in Solid Mechanics," George Allen & Unwin, London.
- Czernin, W. (1962). *Chemistry and Physics of Cement for Civil Engineers*, Chemical Publishing Co., New York.
- Diamond, S. and Mindess, S. (1980). "Scanning Electron Microscope Observations of the Cracking in Portland Cement Paste," *Proceedings, Seventh International Symposium on the Chemistry of Cement*, 3, Paris.
- Diamond, S. and Mindess, S. (1980) "A Preliminary SEM Study of Crack Propagation in Mortar", *Cement and Concrete Research*, 10 (4), 509-519.
- Du, W. and Kemeny, J. M. (1993). "Modelling Borehole Breakout by Mixed Mode Crack Growth, Interaction, and Coalescence," *International Journal of Rock Mechanics and Mining Science and Geomechanics Abstracts*, 30(7), 809-812.

- Du, W. (1994). "Numerical modeling of mixed mode multiple crack propagation and its application to the simulation of non-linear rock deformation and borehole breakout," *Ph.D. Thesis*, University of Arizona.
- Eitel, W. (1941). "Recent Results of Cement Research," *Angewandte Chemie*, 54(15/16), 185-192.
- Eitel, W. (1942). "Electron Microscopic Cement Research," *Zement*, 31, 489-495.
- Gettu, R., Bazant, Z. P., and Karr, M. E. (1990). "Fracture Properties and Brittleness of High Strength Concrete," *American Concrete Institute Journal of Materials*, 87(6), 608-618.
- Goldstein, J. I., Newbury, D. E., Echlin, P. E., Joy, D. C., Romig, D. A., Lyman, C. E., Fiori, C., and Lifshin, E. (1992), "Scanning Electron Microscopy and X-Ray Microanalysis," Plenum Press, New York.
- Griffith, A. A. (1920). "The phenomena of rupture and flow in solids," *Philosophical Transactions of the Royal Society of London, Series A221*, 163-198.
- Griffith, A. A. (1924). "The theory of rupture," *Proceedings of First International Congress of Applied Mechanics, Delft*, 55-63.
- Grudemo, A. (1960). "The Microstructure of Hydrated cement Paste," *Proceedings, Fourth International Symposium on the Chemistry of Cement*, 2, 615-658, Washington, D.C.
- Hadley, K. (1976). "Comparison of Calculated and Observed Crack Densities and Seismic Velocities in Westerly Granite," *Journal of Geophysical Research*, 81(20), 3484-3494.
- Hamstad, M. A. (1986). "A review: Acoustic emission, a tool for composite materials studies," *Exper. Mech.*, 26(1), 7-13.

- He, H. and Ahrens, T. J. (1994). "Mechanical Properties of Shock-damaged Rocks," *International Journal of Rock Mechanics and Mining Science and Geomechanics Abstracts*, 31(5), 525-533.
- Hognestad, E., Hanson, N. W., and McHenry, D. (1955). "Concrete Stress Distribution in Ultimate Stress Design," *Journal of the American Concrete Institute, Proceedings*, 455-479.
- Hsu, T. T. C. (1963). "Mathematical Analysis of Shrinkage Stresses in a Model of Hardened Concrete," *Journal of the American Concrete Institute, Proceedings*, 60, 3, 371-390.
- Hsu, T. T. C. and Slate, F. O. (1963). "Tensile Bond Strength Between Aggregate and Cement Paste or Mortar," *Journal of the American Concrete Institute, Proceedings*, 60(4), 465-486.
- Hsu, T. T. C., Slate, F. O., Sturman, G. M., and Winter, G. (1963). "Microcracking of Plain Concrete and the Shape of the Stress-Strain Curve," *Journal of the American Concrete Institute, Proceedings*, 60(14), 209-224.
- Huang, J. and Li, V. C. (1989). "A Meso-Mechanical Model of the Tensile Behavior of Concrete-Part I: Modelling of Pre-Peak Stress-Strain Relation," *Composites*, 20(4), 361-369.
- Inglis, C. E. (1913). "Stresses in a plate due to the presence of cracks and sharp corners," *Transactions of the Institute of Naval Architects*, 55, 219-241.
- Irwin, G. R. (1956). "Onset of Fast Crack Propagation in High Strength Steel and Aluminium Alloys," *Sagamore Research Conference Proceedings*, 2, 289-305.
- Irwin, G. R. (1957). "Analysis of Stresses and Strains near the End of a Crack Transversing a Plate," *Trans ASME, Journal of Applied Mechanics*, 24, 361-364.

- Jones, R. (1952). "A Method of Studying the Formation of Cracks in a Material Subject to Stresses," *British Journal of Applied Physics*, London, 229-232.
- Kemeney, J. M. (1991). "A Model for Non-linear Rock Deformation Under Compression Due to Sub-critical Crack Growth," *International Journal of Rock Mechanics and Mining Science and Geomechanics Abstracts*, 28(6), 459-467.
- Kranz, R. L. (1983). "Microcracks in Rocks: A Review," *Tectonophysics*, 100, 449-480.
- Kupfer, H. B. and Gerstle, K. H. (1973). "Behavior of Concrete under Biaxial Stresses," *Journal of Engineering Mechanics*, Div. ASCE, 99(EM4), Proc. pap. 9917, 852-866.
- Lajtai, E. Z. (1974). "Brittle Fracture in Compression," *International Journal of Fracture*, 10(4), 525-536.
- Le Chatelier, H. (1882). "Experimental Researches on the Constitution of Hydraulic Mortars," translated by J. L. Mack, McGraw, New York, 1905. Also: *Compt. rend.*, 94 (1882) 13; and *Journal of Chemical Ind.*, 1 (1882) 151.
- L'Hermite, R. (1954). "Present Day Ideas in Concrete Technology. Part 3: The Failure of Concrete," *RILEM Bulletin*, 27-38.
- Liu, T. C. Y., Nilson, A. H., and Slate, F. O. (1972). "Stress-Strain Response and Fracture of Concrete in Uniaxial and Biaxial Compression," *Journal of American Concrete Institute, Proceedings*, 69(5), 291-295.
- Maji, A. K., Ouyang, C., and Shah, S. P. (1990). "Fracture Mechanics of Quasi-Brittle Materials Based on Acoustic Emission," *Journal of Materials Research*, 5(1), 206-217.
- Maji, A. K. and Shah, S.P. (1990). "Measurement of Mixed-mode crack Profiles by Holographic Interferometry," *Experimental Mechanics*, 30(N2), 201-207.

- Mandelbrot, B. B. (1977). "The Fractal Geometry of Nature," W.H. Freeman, New York.
- Martz, H. E., Schneberk, D. J., Roberson, G. P., and Monteiro, P. J. M. (1993). "Computerized Tomography Analysis of reinforced Concrete," *ACI Materials Journal*, 90(3), 259-264.
- Maso, J. C., (1980). "Proceedings of the Seventh International Congress on the Chemistry of Cements," 1, Editions Septima, Paris.
- Massat, M., Ollivier, J. P., and Ringot E. (1988). "Microscopic Analysis of Microcracking Damage in Concrete and Durability," *Laboratoire Materiaux et Durabilite des Constructions (INSA-UPS)*, Toulouse, France.
- McLaughlin, R. (1977). "A study of the differential scheme for composite materials," *International Journal of Engineering Science*, 15, 237.
- Mehta, P. K. and Monteiro, P. J. M. (1993). "Concrete- Structure, Properties, and Material," Prentice Hall, Second Edition, 494-500.
- Mindess, S. and Diamond, S. (1980). "The Cracking and Fracture of Mortar," *Proceedings of a session sponsored by the committee on property of materials of the ASCE Engineering Mechanics Division*, Hollywood, Florida.
- Mobasher, B., Castro-Montero A., and Shah, S. P. (1990). "A Study of Fracture in Fiber-reinforced Cement-based Composites Using Laser Holographic Interferometry," *Experimental Mechanics*, 30(N3), 201-207.
- Monteiro, P. J. M. and King, M. S. (1988). "Experimental Studies of Elastic Wave Propagation in High-Strength Mortar," *ASTM Journal, Cement, Concrete, and Aggregates*, CCAGDP, 10(2), 68-74.
- Monteiro, P. J. M., Helene, P. R. L., and Kang, S. H. (1993). "Designing concrete mixtures for strength, elastic modulus and fracture energy," *Materials and Structures*, RILEM, 26, 443-452.
- Moran B. and Sih, C. F. (1987). "A General Treatment of Crack Tip Contour Integrals," *International Journal of Fracture*, 35, 295-310.

- Mori, T. and Tanaka, K. (1973). "Average stress in matrix and average elastic energy of materials with misfitting inclusions," *Acta Metall.*, 21, 571-574.
- Nakasa, K. and Nakatsuka, J. (1991). "Crack Initiation, Propagation and Branching in a Disk of Brittle Material Under Axisymmetric Tension." *Engineering Fracture Mechanics*, 39(4), 661-670.
- Nakasa, K. and Nakatsuka, J. (1994). "Analysis of crack branching morphology in a disk of brittle material under axisymmetric tension by using branching dimension," *Engineering Fracture Mechanics*, 47(3), 403-415.
- Nemat-Nasser, S. and Hori, M. (1993). "Micromechanics: overall properties of heterogeneous materials," Elsevier Science Publisher B.V., The Netherlands, 345-358.
- Neville, A. M. (1981). "Properties of Concrete," Longman Science & Technical, New York.
- Noris, A. N. (1985). "A differential scheme for the effective moduli of composites," *Mech. Mater.*, 4, 1.
- Orr, C, Jr. (1969/70). "Application of Mercury Penetration to Material Analysis, Powder Technology," Elsevier Sequoia S.A., Lausanne, 117-123.
- Ouyang, C., Landis, E., and Shah, S. P. (1991). "Damage Assessment in Concrete Using Quantitative Acoustic Emission," *ASCE Journal of Engineering Mechanics*, 117(11), 2681-2698.
- Pyrak, L. J. (1988). "Seismic Visibility of Fractures." *Ph.D. Thesis*, Department of Material Science and Mineral Engineering, University of California at Berkeley.
- Radczewski, O. E., Müller, H. O., and Eitel, W. (1939). "Ultra-Microscopic Examination of Hydration of Lime," *Zement*, 28(49), 693-697.

- Regnault, P. and Bruhwiler, E. (1990). "Holographic Interferometry for the Determination of Fracture Process Zone in Concrete," *Engineering Fracture Mechanics*, 35(1/2/3), 29-38.
- Richart, F. E., Brandtzaeg, A. , and Brown, L. (1929). "A Study of the Failure of Concrete Under Combined Compressive Stresses," *Bulletin No. 185, University of Illinois Engineering Experiment Station, Urbana*, 102.
- Ringot, E (1988). "Automatic quantification of microcracks network by stereological method of total projections in mortars and concretes," *Cement and Concrete Research*, 18, 35-43.
- Rossi, P. and Le Maou, F. (1989). "New Methods for Detecting Cracks in Concrete Using Fibre Optics," *RILEM Materials and Structures*, 437-442.
- Russ, John C. (1986). "Practical Stereology," Plenum Press, New York.
- Salganik, R. L. (1973). "Mechanics of Bodies with Many Cracks," *Mechanics of Solids*, 8(4), 135-143.
- Saltikov, S. A. (1967). "A Stereological Method for Measuring the Specific Surface Area of Metallic Powders, Stereology, edited by H. Elias, *Proc. Second International Congress for Stereology*, Chicago; Springer Verlag, New York.
- Saltikov, S. A. (1945). "Stereometric Metallography," second edition, Metallurgizdat, Moscow.
- Sammis, C. G., and Ashby, M. F. (1986). "The Failure of Brittle Porous Solids Under Compressive Stress States," *Acta Metall.*, 34(3), 511-526.
- Schlueter, E., Cook, N. G. W., Zimmerman, R. W., and Witherspoon, P. A. (1991). "Predicting permeability and electrical conductivity of sedimentary rocks from microgeometry," *Rock Mechanics as a Multidisciplinary Science*, Roegiers (ad.), Rotterdam, 355-364.
- Shah, S. P. and Chandra, S. (1970). "Fracture of concrete subjected to cyclic and sustained loading," *ACI Journal*, Proceedings 67(10), 816-825.

- Shah, S. P. and Sankar, R. (1987). "Internal cracking and strain softening response of concrete under uniaxial compression," *ACI Materials Journal*, 84(3), 200.
- Slate, F. O. and Olsefski, S. (1963). "X-Rays for Study of Internal Structure and Microcracking of Concrete," *Journal of the American Concrete Institute*, Proceedings, 60(31), 575-588.
- Smith, C. S. and Guttman, L. (1953). "Measurement of Internal Boundaries in Three Dimensional Structures by Random Sectioning," *Trans. AIME*, 197.
- Stroeven, P. (1973). "Some Aspects of Micromechanics of Concrete," PhD Thesis, Stevin Laboratory, Technological University of Delft.
- Stroeven, P. (1976). "Application of various stereological methods to the study of the grain and the crack structure of concrete," *Journal of Microscopy*, 107(3), 313-321.
- Stroeven, P. (1976). "Morphometry of plain and fibre reinforced concrete by means of image analysis techniques," *Proceedings of the second International conference on Mechanical Behavior of Materials*, Boston, Massachusetts, 1675-1679.
- Stroeven, P. (1979). "Geometric probability approach to the examination of microcracking in plain concrete," *Journal of Materials Science*, 14, 1141-1151.
- Stroeven, P. (1991). "Fractals and Fractography in Concrete Technology," *International Symposium on Brittle Matrix Composites*, 3rd, Warsaw, Poland, 1-10.
- Stroeven, P. (1992). "Some mechanical effects of interface debonding in plain concrete, Interfaces in Cementitious Composites," *Proceedings of the RILEM International Conference*, Edited by J.C. Maso, Toulouse, France, 187-196.
- Tavasci, B. (1942). "Structure of Hydrated Portland Cement," *Zement*, 30(4), 43-48 & 55-58.

- Underwood, E. E. (1968). "Quantitative Stereology," Addison-Wesley Publishing Company, New Jersey.
- Whitehurst, E. A. (1966). "Evaluation of Concrete Properties from Sonic Tests," Monograph No. 2, *American Concrete Institute*, Detroit, Michigan.
- Wittmann, F. H. (1983). "Fracture Mechanics of Concrete," Lausanne, Switzerland, Elsevier Science Publishers B.V., Amsterdam.
- Wittmann, F. H. (1986). "Fracture Toughness and Fracture Energy of Concrete," *Proceedings of the International Conference on Fracture Mechanics of Concrete*, Lausanne, Switzerland, October 1-3, Elsevier Science Publishers B.V., Amsterdam.
- Yadev, G.D., Dullien, F. A. L., Chatzis, I., and Macdonald, I. F. (1984). "Microscopic Distribution of Wetting and Non-Wetting phases in Sandstone During Immiscible Displacements," *Paper SPE 13212, presented at the 1984 SPE Annual Technical Conference and Exhibition*, Dallas, Texas.
- Zheng, Z. (1989). "Compressive stress-induced microcracks in rocks and applications to seismic anisotropy and borehole stability," *PhD Thesis*, Department of Material Science and Mineral Engineering, University of California, Berkeley.
- Zimmerman, R. W. (1985). "The Effect of Microcracks on the Elastic Moduli of Brittle Materials," *Journal of Material Science Letters*, 4, 1457-1460.
- Zimmerman, R. W. (1991). "Elastic moduli of a solid containing spherical inclusions," *Mechanics of Materials*, 12, 17-24.

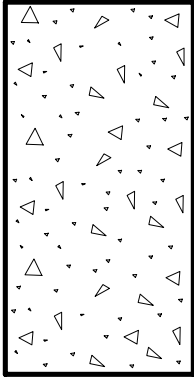
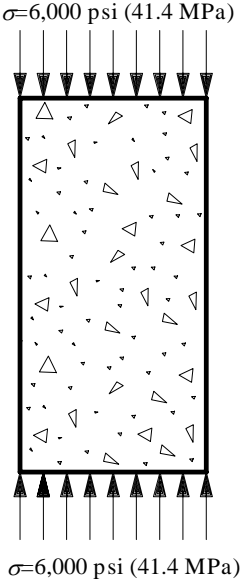
APPENDICES

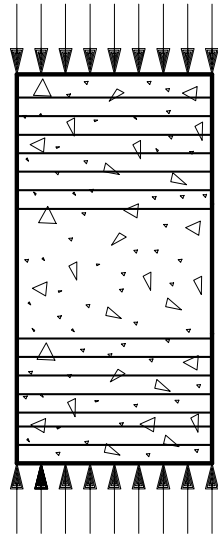
APPENDIX A EXPERIMENTS CONDUCTED

APPENDIX B IMAGE ANALYZER COMPUTER PROGRAMS

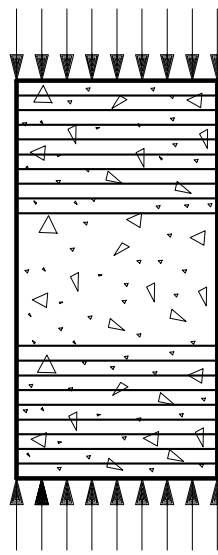
APPENDIX C TEST CELL DESIGN

APPENDIX A: EXPERIMENTS CONDUCTED

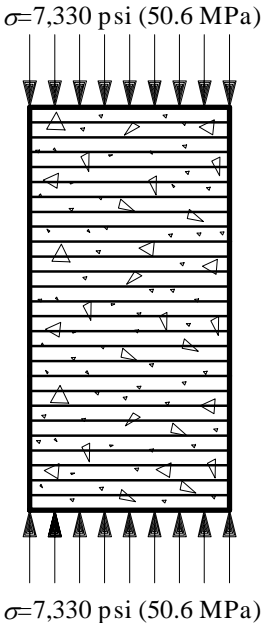
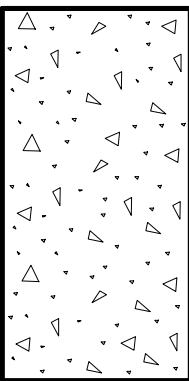
EXPERIMENT #1	
	<p>Loading Condition: NO-LOAD</p> <p>Applied Stresses: 0</p> <p>Concrete Type: NORMAL STRENGTH</p> <p>Specimen Size: 4"Ø×8" High</p> <p>Ultimate Strength: 7,500 psi (94,600 #)</p> <p>Date of Cast: November 16, 1989</p> <p>Date Tested: March 4, 1992</p> <p>Confinement: NONE</p> <p>Experiment Date: April 5, 1992</p>
EXPERIMENT #2	
	<p>Loading Condition: UNIAXIAL</p> <p>Applied Stresses: 6,000 psi</p> <p>Concrete Type: NORMAL STRENGTH</p> <p>Specimen Size: 4"Ø×8" High</p> <p>Ultimate Strength: 7,500 psi (94,600 #)</p> <p>Date of Cast: November 16, 1989</p> <p>Date Tested: March 4, 1992</p> <p>Confinement: NONE</p> <p>Experiment Date: October 29, 1992</p>

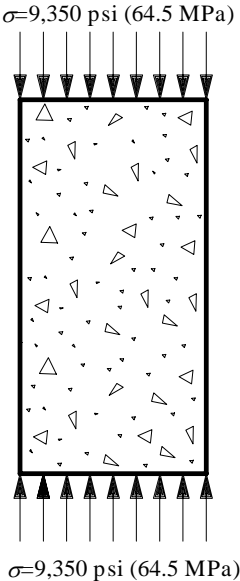
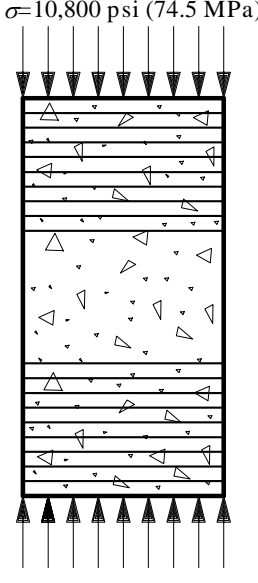
EXPERIMENT #3 $\sigma=5,000$ psi (34.5 MPa) $\sigma=5,000$ psi (34.5 MPa)Loading Condition: **TRIAXIAL**Applied Stresses: **5,000 psi**Concrete Type: **NORMAL STRENGTH**Specimen Size: **4"Ø×8" High**Ultimate Strength: **7,500 psi (94,600 #)**Date of Cast: **November 16, 1989**Date Tested: **March 4, 1992**Confinement: **CONFINED 1/3 FROM EACH END**Experiment Date: **September 17, 1992**

(Pitch of Winding: 10 Threads/Inch, Pre-Tension: 150 lbs)

EXPERIMENT #4 $\sigma=6,000$ psi (41.4 MPa) $\sigma=6,000$ psi (41.4 MPa)Loading Condition: **TRIAXIAL**Applied Stresses: **6,000 psi**Concrete Type: **NORMAL STRENGTH**Specimen Size: **4"Ø×8" High**Ultimate Strength: **7,500 psi (94,600 #)**Date of Cast: **November 16, 1989**Date Tested: **March 4, 1992**Confinement: **CONFINED 1/3 FROM EACH END**Experiment Date: **September 22, 1992**

(Pitch of Winding: 20 Threads/Inch, Pre-Tension: 150 lbs)

EXPERIMENT #5	
 <p>$\sigma = 7,330 \text{ psi (50.6 MPa)}$</p> <p>$\sigma = 7,330 \text{ psi (50.6 MPa)}$</p>	<p>Loading Condition: TRIAXIAL</p> <p>Applied Stresses: 7,330 psi</p> <p>Concrete Type: NORMAL STRENGTH</p> <p>Specimen Size: 4"Ø×8" High</p> <p>Ultimate Strength: 7,500 psi (94,600 #)</p> <p>Date of Cast: November 16, 1989</p> <p>Date Tested: March 4, 1992</p> <p>Confinement: FULLY CONFINED</p> <p>Experiment Date: April 5, 1992</p> <p>(Pitch of Winding: 20 Threads/Inch, Pre-Tension: 150 lbs)</p>
EXPERIMENT #6	
	<p>Loading Condition: NO-LOAD</p> <p>Applied Stresses: 0</p> <p>Concrete Type: HIGH STRENGTH</p> <p>Specimen Size: 4"Ø×8" High</p> <p>Ultimate Strength: 11,000 psi (138,200 #)</p> <p>Date of Cast: October 30, 1991</p> <p>Date Tested: 1991</p> <p>Confinement: NONE</p> <p>Experiment Date: September 28, 1992</p>

EXPERIMENT #7	
 <p>$\sigma=9,350 \text{ psi (64.5 MPa)}$</p> <p>$\sigma=9,350 \text{ psi (64.5 MPa)}$</p>	<p>Loading Condition: UNIAXIAL</p> <p>Applied Stresses: 9,350 psi</p> <p>Concrete Type: HIGH STRENGTH</p> <p>Specimen Size: 4"Øx8" High</p> <p>Ultimate Strength: 11,000 psi (138,200 #)</p> <p>Date of Cast: October 30, 1991</p> <p>Date Tested: 1991</p> <p>Confinement: NONE</p> <p>Experiment Date: March 4, 1993</p>
EXPERIMENT #8	
 <p>$\sigma=10,800 \text{ psi (74.5 MPa)}$</p> <p>$\sigma=10,800 \text{ psi (74.5 MPa)}$</p>	<p>Loading Condition: TRIAXIAL</p> <p>Applied Stresses: 10,800 psi</p> <p>Concrete Type: HIGH STRENGTH</p> <p>Specimen Size: 4"Øx8" High</p> <p>Ultimate Strength: 11,000 psi (138,200 #)</p> <p>Date of Cast: October 30, 1991</p> <p>Date Tested: 1991</p> <p>Confinement: CONFINED 1/3 FROM EACH END</p> <p>Experiment Date: March 5, 1993</p> <p>(Pitch of Winding: 20 Threads/Inch, Pre-Tension: 150 lbs)</p>

APPENDIX B: IMAGE ANALYZER COMPUTER PROGRAMS

Macro to calculate the number of intercepts with cracks in an image by reference to intercept lines at various angles to the vertical (lines in increments of 15 degrees). Also, macro will find both #3 way and 4 way intersections in a binary thinned image.

```

loadlut "grey"
setframe "F512"
alpha
clearallio 0
Xclrmess
resetvec "aspA"
resetvec "aspB"
resetpar
setimpath "c:/images"
getim "flin0",21
getim "flin15",22
getim "flin30",23
getim "flin45",24
getim "flin60",25
getim "flin75",26
getim "flin90",27
getim "flin105",28
getim "flin120",29
getim "flin135",30
getim "flin150",31
getim "flin165",32
scalgeom 1,"x60",_OFF,_OFF
global TAREA
global CK0,CK15,CK30,CK45,CK60,CK75,CK90,CK105,CK120,CK135,CK150,CK165,TCK
global
SCK0,SCK15,SCK30,SCK45,SCK60,SCK75,SCK90,SCK105,SCK120,SCK135,SCK150,SCK165,
STCK
global SURFA,SURFASM
global NODES,SNODES
SURFA=SURFASM=TAREA=0.0
CK0=CK15=CK30=CK45=CK60=CK75=CK90=CK105=CK120=CK135=CK150=CK165=
TCK=0
SCK0=SCK15=SCK30=SCK45=SCK60=SCK75=SCK90=SCK105=SCK120=SCK135=SCK150=
SCK165=STCK=0
NODES=SNODES=0
dbA="kamran"
dbB="kamran"
rt="kamran"
m=20

```

```

InitField AREAP,TOTALAREA,IELDFCOUNT
aspA[]=TAREA,AREAP,CK0,CK15,CK30,CK45,CK60,CK75,CK90,CK105,CK120,CK135,
CK150,CK165,TCK,SURFA,NODES
aspB[]=SCK0,SCK15,SCK30,SCK45,SCK60,SCK75,SCK90,SCK105,SCK120,SCK135,SCK150,
SCK165,STCK,SURFASM,SNODES
read "Enter root name:",rt
read "Enter database name:",dbA
read "Enter database name (straightened cracks):",dbB
read "Enter number of images:",m
setimpath "f:/" + string(rt)
DBerase dbA
DBerase dbB
DBcreate dbA,"aspA"
DBcreate dbB,"aspB"

```

```

for n=1,n<=m,n=n+1
getim n,1
write "IMAGE ",n
dis2lev 1,2,170,255,_ON,_OFF,1
scrap 2,12,_OFF,0,10,_ON,_ON
scrap 2,3,_OFF,0,2,_ON,_ON
close 3,4,7,255,1
open 4,5,7,255,1
scrap 5,6,_OFF,0,200,_ON,_ON
andim 6,12,7
xorim 7,12,8
scrap 8,9,_OFF,0,10,_ON,_ON
thinbin 9,10,0,0,_OFF,_ON
dilate 10,11,7,255,2
thinbin 11,11,0,0,_OFF,_ON

```

```

morpho3x3 10,14,"nodes","nodes",1,0,1
morpho3x3 11,15,"nodes","nodes",1,0,1
dilate 14,14,5,255,1
dilate 15,15,5,255,1
identify 14,14,_OFF,_ON
identify 15,15,_OFF,_ON
Measf 14
NODES=IELDFCOUNT
Measf 15
SNODES=IELDFCOUNT

```

```

andim 10,21,14
andim 11,21,15
dilate 14,14,5,255,1
dilate 15,15,5,255,1
identify 14,14,_OFF,_ON
identify 15,15,_OFF,_ON
Measf 14
CK0=IELDFCOUNT

```

Measf 15
SCK0=FIELD COUNT
andim 10,22,14
andim 11,22,15
dilate 14,14,5,255,1
dilate 15,15,5,255,1
identify 14,14,_OFF,_ON
identify 15,15,_OFF,_ON
Measf 14
CK15=FIELD COUNT
Measf 15
SCK15=FIELD COUNT
andim 10,23,14
andim 11,23,15
dilate 14,14,5,255,1
dilate 15,15,5,255,1
identify 14,14,_OFF,_ON
identify 15,15,_OFF,_ON
Measf 14
CK30=FIELD COUNT
Measf 15
SCK30=FIELD COUNT
andim 10,24,14
andim 11,24,15
dilate 14,14,5,255,1
dilate 15,15,5,255,1
identify 14,14,_OFF,_ON
identify 15,15,_OFF,_ON
Measf 14
CK45=FIELD COUNT
Measf 15
SCK45=FIELD COUNT
andim 10,25,14
andim 11,25,15
dilate 14,14,5,255,1
dilate 15,15,5,255,1
identify 14,14,_OFF,_ON
identify 15,15,_OFF,_ON
Measf 14
CK60=FIELD COUNT
Measf 15
SCK60=FIELD COUNT
andim 10,26,14
andim 11,26,15
dilate 14,14,5,255,1
dilate 15,15,5,255,1
identify 14,14,_OFF,_ON
identify 15,15,_OFF,_ON
Measf 14
CK75=FIELD COUNT

Measf 15
SCK75=FIELD COUNT
andim 10,27,14
andim 11,27,15
dilate 14,14,5,255,1
dilate 15,15,5,255,1
identify 14,14,_OFF,_ON
identify 15,15,_OFF,_ON
Measf 14
CK90=FIELD COUNT
Measf 15
SCK90=FIELD COUNT
andim 10,28,14
andim 10,28,15
dilate 14,14,5,255,1
dilate 15,15,5,255,1
identify 14,14,_OFF,_ON
identify 15,15,_OFF,_ON
Measf 14
CK105=FIELD COUNT
Measf 15
SCK105=FIELD COUNT
andim 10,29,14
andim 11,29,15
dilate 14,14,5,255,1
dilate 15,15,5,255,1
identify 14,14,_OFF,_ON
identify 15,15,_OFF,_ON
Measf 14
CK120=FIELD COUNT
Measf 15
SCK120=FIELD COUNT
andim 10,30,14
andim 11,30,15
dilate 14,14,5,255,1
dilate 15,15,5,255,1
identify 14,14,_OFF,_ON
identify 15,15,_OFF,_ON
Measf 14
CK135=FIELD COUNT
Measf 15
SCK135=FIELD COUNT
andim 10,31,14
andim 11,31,15
dilate 14,14,5,255,1
dilate 15,15,5,255,1
identify 14,14,_OFF,_ON
identify 15,15,_OFF,_ON
Measf 14
CK150=FIELD COUNT

```
Measf 15
SCK150=FIELDCOUNT
andim 10,32,14
andim 11,32,15
dilate 14,14,5,255,1
dilate 15,15,5,255,1
identify 14,14,_OFF,_ON
identify 15,15,_OFF,_ON
Measf 14
CK165=FIELDCOUNT
Measf 15
SCK165=FIELDCOUNT
Measf 10
TAREA=TOTALAREA
TCK=CK0+CK15+CK30+CK45+CK60+CK75+CK90+CK105+CK120+CK135+CK150+CK165
STCK=SCK0+SCK15+SCK30+SCK45+SCK60+SCK75+SCK90+SCK105+SCK120+SCK135+
SCK150+SCK165
SURFA=3.0929E-6*TCK
SURFASM=3.0929E-6*STCK
Measf 9

DBopen dbA,"aspA"
DBappend dbA
DBclose dbA
DBopen dbB,"aspB"
DBappend dbB
DBclose dbB
endfor
outlist dbA,0
outlist dbB,0
graphic
```

Macro to calculate the number and length of cracks in an image

```

loadlut "grey"
setframe "F512"
alpha
clearallio 0
Xclrmess
resetvec "aspA"
resetvec "aspB"
resetpar
scalgeom 1,"x60",_OFF,_OFF
global NCRK,SNCRK,LCRK,SLCRK,ACRK,SACRK
NCRK=SNCRK=0
LCRK=SLCRK=ACRK=SACRK=0.0
dbA="kamran"
dbB="kamran"
rt="kamran"
m=20
InitField FIELDCOUNT
InitObj ANGLEDMAX,PERIM
aspA[]=NCRK,LCRK,ACRK
aspB[]=SNCRK,SLCRK,SACRK
read "Enter root name:",rt
read "Enter database name:",dbA
read "Enter database name (smoothed):",dbB
read "Enter number of images:",m
setimpath "f:/" + string(rt)
DBerase dbA
DBcreate dbA,"aspA"
DBclose dbA
DBerase dbB
DBcreate dbB,"aspB"
DBclose dbB

for n=1,n<=m,n=n+1
getim n,1
write "IMAGE ",n
dis2lev 1,2,170,255,_ON,_OFF,1
scrap 2,12,_OFF,0,10,_ON,_ON
scrap 2,3,_OFF,0,2,_ON,_ON
close 3,4,7,255,1
open 4,5,7,255,1
scrap 5,6,_OFF,0,200,_ON,_ON
andim 6,12,7
xorim 7,12,8
scrap 8,9,_OFF,0,10,_ON,_ON
thinbin 9,10,0,0,_OFF,_ON
dilata 10,11,7,255,2

```

```
thinbin 11,11,0,0,_OFF,_ON
```

```
identify 10,10,_ON,_OFF
```

```
Measf 10
```

```
NCRK=FIELDCOUNT
```

```
f=FIELDCOUNT
```

```
identify 10,10,1,0
```

```
for c=1,c<=f,c=c+1
```

```
Measo 10
```

```
LCRK=PERIM/2
```

```
ACRK=ANGLEDMAX
```

```
DBopen dbA,"aspA"
```

```
DBappend dbA
```

```
DBclose dbA
```

```
endfor
```

```
identify 11,11,_ON,_OFF
```

```
Measf 11
```

```
SNCRK=FIELDCOUNT
```

```
g=FIELDCOUNT
```

```
identify 11,11,1,0
```

```
for d=1,d<=g,d=d+1
```

```
Measo 11
```

```
SLCRK=PERIM/2
```

```
SACRK=ANGLEDMAX
```

```
DBopen dbB,"aspB"
```

```
DBappend dbB
```

```
DBclose dbB
```

```
endfor
```

```
endfor
```

```
outlist dbA,0
```

```
outlist dbB,0
```

```
graphic
```

Macro to measure interfacial cracks in an image
--

```

clearallo 0
Xclrmess
resetvec "asp"
resetpar
scalgeom 1,"x60",_OFF,0
global area,area2
area=area2=0.0
global INTAREA,INTA2
INTAREA=INTA2=0.0
global FINT,FINT2
FINT=FINT2=0.0
db="kamran"
rt="kamran"
m=20
InitField TOTALAREA
asp[]=area,INTAREA,FINT,area2,INTA2,FINT2
read "Enter root name:",rt
read "Enter database name:",db
read "Enter number of images:",m
setimpath "f:/" + string(rt)
DBerase db
DBcreate db,"asp"

for n=1,n<=m,n=n+1
getim n,1
write "IMAGE ",n
scalim 1,9,0,255,1,255,0,255,1
eraseinside 9,10,0
ans="y"
_STATUS=1
while 1
Xclrmess
read "Edit OK (type n to edit again, <Esc> if OK :",ans
if _STATUS==27:break
if ans=="n" : eraseinside 9,10,0
endwhile
dis2lev 10,10,0,1,_ON,_OFF,1
scrap 10,10,_OFF,0,30,_ON,_ON
dilate 10,11,7,255,2
xorim 11,10,12
dilate 12,12,7,255,1
dis2lev 1,2,170,255,_ON,0,1
scrap 2,3,_OFF,0,2,_ON,_ON
scrap 2,14,_OFF,0,10,_ON,_ON
close 3,4,7,255,1

```

```
open 4,5,7,255,1
scrap 5,6,_OFF,0,200,_ON,_ON
andim 6,14,7
xorim 7,14,8
scrap 8,9,_OFF,0,10,_ON,_ON
thinbin 9,15,0,0,_OFF,_ON
thinbin 14,4,0,0,_OFF,_ON
andim 4,12,5
Measf 4
area=TOTALAREA
if area==0 : area=10000000000
Measf 5
INTAREA=TOTALAREA
FINT=INTAREA/area
andim 15,12,6
Measf 15
area2=TOTALAREA
if area2==0 : area2=10000000000
Measf 6
INTA2=TOTALAREA
FINT2=INTA2/area2

DBopen db,"asp"
DBappend db
DBclose db
endfor

outlist db,0
```

KONTRON CODES

alpha

Sets the graphic display to alpha-numeric mode.

Parameters:

none

andim (input1, input2, output)

Andim correlates every pixel which is both in image 1 and image 2 and the result outputted to image 3. *Input1* and *Input2* are the two binary images to be correlated.

clearallio (greyvalue)

Clears the overall and contents of the entire image memory. The image memory is set to a level **GrayValue**.

Parameters:

GrayValue image to be processed

close (input, output, shape, phase, count)

Objects in a binary or grey image are first dilated using a structuring element defined by *shape_?*, and then eroded, using the same structuring element. This procedure merges closely adjacent objects. The closing procedure can be iterated.

Parameters:

Input	image to be processed
Output	the processed image
Shape_?	structuring element for the operation:
	=1 horizontal vector
	=2 vertical vector
	=3 diagonal vector, 45 degrees
	=4 diagonal vector, 135 degrees
	=5 cross
	=6 square
	=7 octagon
	=8 alternate squares/crosses
Phase	selects the grey level for closing
Count	number of operations

condition is a logical expression. *Start value* and *icrement* are arithmetic or logical expressions. Example: *for i=1, i<15, i=i+1 : write.*

DBappend (fname)

Appends the currend record to the end of the file. There is no need to position the file to the last record for this operation.

Parameters:

Fname file name

DBclose (fname)

Closes a file that has been opened with *DBopen*.

Parameters:

Fname file name

DBcreate (fname,,fvect)

Creates a new data file. The extension .d00 will automatically be added to the specific name.

Parameters:

Fname file name
Fvect feature vector as specified in the introduction

DBerase (fname,,fvect)

Erases a data file (equivalent to the MS-DOS del command).

Parameters:

Fname file name

DBopen (fname,,fvect)

Opens an existind data file. Any access to a data file (read, write) must be preceded by this opening step (or by *DBcreate*).

Parameters:

Fname data file name. A string of up to 8 characters, that constitutes a valid file name under MS-DOS.
Fvect a return parameter, describing the feature vector used to create the file.

dilate (input, output, shape, phase, count)

Dilates objects with the grey level *phase* in binary or grey images, using various structuring element *shape*. The dilation process can be iterated.

Parameters:

Input image to be dilated
Output the dilated image
Shape_? structuring element for the operation:
 =1 horizontal vector
 =2 vertical vector
 =3 diagonal vector, 45 degrees
 =4 diagonal vector, 135 degrees
 =5 cross
 =6 square
 =7 octagon
 =8 alternate squares/crosses
Phase selects the grey level for dilation
Count number of dilations

dis2lev (Input, Output, LevelLow, LevelHigh, <I>Binary, <I>Inter, mode)

This function is used for segmentation of binary or multiphase images from grey images. 2 threshold levels discriminates objects from the background by setting two thresholds. Either the grey levels inside or those outside the selected limits will be set to grey value 0 (black, background). Depending on the variable **Binary**, the remaining pixels either keep their original grey levels or are set to white (255). The thresholds can be selected numerically or set interactively, depending on the **Mode**. The interactive setting is performed in relation to the X- and Y- position of the cursor on the tablet. Thresholds in histogram is interactive thresholding via a gray level histogram copied into the input image.

Parameters:

Input	image to be segmented
Output	the segmented image
LevelLow	lower grey level threshold
LevelHigh	upper grey level threshold
	These variables will carry return values, if the thresholds are defined interactively.
Binary	_ON the discriminated pixels are set to 255 (white), all other pixels are
<logical>	set to 0 (background)
	_OFF the discriminated pixels keep their original grey levels
Inter	_ON the threshold levels are defined interactively, by moving the cursor in horizontal (LevelLow) and vertical direction (LevelHigh). A grey scale is temporarily inserted on top of the Input image, to facilitate threshold setting. The values defined interactively for LevelLow and LevelHigh are returned to the parameters after execution of the function.
	_OFF the threshold levels are taken as defined by LevelLow and LevelHigh .
Mode_?	to select the threshold definition, if Inter is _ON
	=1 to modify LevelLow and LevelHigh Interactively
	=2 to choose LevelHigh according to the value given to the parameters and change LevelLow interactively
	=3 to choose LevelLow according to the value given to the parameters and change LevelHigh interactively

disdyn (input, output, size, threshold, <I>binary, <I>darkbackgr, <I>inter)

Dynamic threshold generates a binary image by computing a single adaptive threshold. The function is particularly useful for the discrimination of small objects and narrow linear structures on varying backgrounds.

Parameters:

Input	image to be segmented
Output	the segmented image
Size (1-255)	matrix size for the lowpass filter used for the reference image
Threshold	threshold level, for numerical input.
	This variable will carry a return value if the threshold is defined interactively
Binary	_ON the discriminated pixels are set to 255 (white)

<logical>	_OFF	the discriminated pixels keep their original grey levels
DarkBackgr	_ON	if the object pixels are lighter than the background
<logical>	_OFF	if the object pixels are darker than the background
Inter	_ON	threshold level is defined interactively, by moving the cursor horizontally. A grey scale scale is temporarily inserted on top of the Input image to simplify threshold setting.
<logical>	_OFF	the threshold level is defined by Threshold

eraseinside (input, output, auxiliary, phase)

This function copies *Input* to *Output* and sets the pixels of an image inside a closed contour into a predefined grey value.

Parameters:

Input	image input
Output	output image
Auxiliary	auxiliary image memory
Phase	grey value to fill the inside of the contour

for loop

This loop is used to repeat the commands in the loop a number of times.

Syntax: *for (start value, condition, increment)*

.

.

endfor

Or: *for (start value, condition, increment) : command*

getim (file, image)

Get image loads an image stored on a disk medium into the image memory.

Parameters:

File	file name of the image to be loaded
Image	image memory into which the image is to be loaded

graphic

sets the alphanumeric display to graphic display mode.

Parameters:

none

identify (input, output, <l>conn_8, <l>refarea)

Identify connects pixels in a binary image, that are part of the same object, into one entity and creates a list of the objects defined by this connectivity test. Every object is assigned its own object label in the form of a grey level common to all its pixels. The identification is a prerequisite for any object-specific or densitometric measurements. The logical parameter *RefArea* is set to _ON, the reference area named FAREA in the system feature vector "scaling" is set to the complete image area.

Parameters:

Input	image to be identified	
Output	the identified image	
Conn_8	_ON	to select 8-connected objects
<logical>	_OFF	to select 4-connected objects
RefArea	_ON	sets reference area to the total area
<logical>	_OFF	the reference area is not changed

InitField (parname)

This function is used to declare individual or multiple field specific parameters for measurement. *ParName* selects the parameter. Multiple parameter names must be separated by a comma. The parameters declared with *InitField* are inserted into the *Field* feature vector. For system-declared features one uses the *Init* commands. For user-defined elements of feature vectors the command

global <parameter>

has to be used, to allow the system global access to the variable. It is suggested that upper-case letters are used for parameter names, to indicate they are treated differently from ordinary local variables.

Parameters:

ParName name(s) of the parameter(s) to be initialized. i.e. AREAP, TOTALAREA, FIELDcount, etc.

InitObj ANGLEDMAX,PERIM

This command defines the features to be measured. By executing the above command, it will ensure that the measurement commands will provide the requested parameters.

Parameters:

ANGLEDMAX angle between the positive X-axis and the DMAX orientation of the object. DMAX is the longest diameter of an object obtained by selecting the largest of the Feret diameters measured in 32 different directions, i.e. at an angular resolution of 5.7 degrees

PERIM the perimeter of an object in an image, calculated as:

$$\text{PERIM} = \text{PERIMX} + \text{PERIMY} + \text{PERIMXY} \cdot \sqrt{2}$$

PERIMX, PERIMY length of perimeter having x (PERMX) and in y (PERIMY) direction.

PERIMXY Length of perimeter having direction of 45 and 135 degrees to x axis.

loadlut (file)

Loads a look-up table stored in subdirectory. *File* refers to the look-up table file to be loaded.

Macros

Macros are command sequences. The concept of macros is helpful to efficiently structure complex programs.

Measf (image)

Measf measures field-specific parameters of the image. The image to be measured has to be binary. If the parameter COUNT is to be measured, the input image has to be identified. Parameters measured are members of the *Field* feature vector.

Parameters:

Image the input image

Measo (image)

Measo measures the previously defined object-specific parameters of the next object in the identified image.

Parameters:

Image the input image

morpho 3x3 (input, output, file, operator, threshold, mode, iteration)

This function executes "hit-or-miss" transformations in binary images, according to the theory of mathematical morphology [*].

Structural elements of size 3x3 can be arbitrarily defined, large matrix sizes can be described by sequential execution of 3x3 transformations.

Parameters:

Input	Name of the input image. The image can be an arbitrary 8 bit grey image.
Output	Name of the output file. This is an 8 bit image in which only two grey values are present: 0 (logical 0) and 255 (logical 1)
File	Name of the MDL text file, without its file type .mdl.
Operator	Name of an <element>, <parallel> or <sequence> object, which is defined in MDL text file.
Threshold	Threshold for internally converting the input image into a binary image. Grey value < threshold means logical 0 Grey value > = threshold means logical 1
Mode_?	Margin definitions: = 0 The input image is embedded in a logical 0 environment. = 1 All margin pixels in the input image are internally set to 1 before morpho-operations are carried out. = 2 The input image is embedded in a logical 1 environment. = 3 Combination of Mode 1 and 2.
Iteration	Number of iterations A value of 0 is an exception.

open (input, output, shape, phase, count)

Objects in a binary or grey image are first eroded using a structuring element defined by *shape_?*, and then dilated using the same structuring element. This procedure eliminates small objects without strongly affecting the larger objects. The opening can be iterated.

Parameters:

Input image to be processed
Output the processed image

Shape_?	structuring element for the operation:
	=1 horizontal vector
	=2 vertical vector
	=3 diagonal vector, 45 degrees
	=4 diagonal vector, 135 degrees
	=5 cross
	=6 square
	=7 octagon
	=8 alternate squares/crosses
Phase	selects the grey level for opening
Count	number of operations to be performed

outlist (database,<I>print)

A list of data measured and stored in the file **Database** is displayed on the monitor or printed out.

Parameters:

DataBase	name of the data file to be listed
Print	_ON print the data list of the whole database
<logical>	(it will not appear on the monitor)
	_OFF display the data on the monitor

resetpar

Erases **all** feature vectors defined.

resetvec (vector)

Erases a selected feature vector. This function can also be used to set all scale factors to the default unity values.

Parameters:

Vector	string variable to specify the feature vector to be deallocated.
---------------	--

scrap (input, output, <I>select, arealow, areahigh, <I>binaryinp, <I>binaryout)

Scrap eliminates objects on the basis of their area, in pixel units. The input and the output image can be of type "binary" or "identified". Objects in the size range [**AreaLow...AreaHigh**] are selected or rejected. The maximum value for **AreaHigh** is 65535 pixels.

Parameters:

Input	image to be processed. if it is a binary image, the variable BinaryInp must be set to _ON .
Output	the processed image. If an identified image is required, the value BinaryOut must be set to _ON .
Select	_ON objects with area in the range
<logical>	[AreaLow...AreaHigh] are retained
AreaLow	lower limit for the area range (in pixels)
AreaHigh	upper limit for the area range (in pixels)
BinaryInp	_ON if the Input image is binary
<logical>	_OFF if the Input image is identified

BinaryOut _ON if the **Output** image will be a binary image
 <logical> _OFF if the **Output** image will be an identified image

setframe (frame)

Selects the format of the images to be processed.

Parameters:

Frame 512 * 480 pixels, image directory name "F512"

setimpath (imagepath)

Selects the path to the subdirectory for the storage and retrieval of images on disk media.

Parameters:

ImagePath DOS directory path for the storage or retrieval of images

scalgeom (image, scale, <I>inter, <I>list)

To determine the scaling factors at a given magnification, a reference image, containing structures of known dimensions (e.g. a ruler), must be available.

Parameters:

Image reference image or scaling
Scale name of the scale (only active when **List** is _OFF)
Inter _ON interactive definition of the scaling factors
 <logical> _OFF scaling factors are determined by scaling 2 points.
 The image is displayed.
List _ON a list of scaling parameters which have been selected
 or are to be edited will be displayed
 _OFF the scaling factors in the "scale" in the file
 geom.def will be used.

scalim (input, output, lowin, highin, lowout, highout, phaselow, phasehigh, mode)

Scale grey value performs a linear grey level scaling of the image defined by **Input** and **Output** grey level range. The grey level ranges in the **Input** and **Output** images are defined via the various **LowIn** / **HighIn** and **LowOut** / **HighOut**, respectively. Grey levels which lie below or above the selected limits (**LowIn** and **HighIn**) can be treated in different ways, depending on the variable **Mode**.

Parameters:

Input image to be scaled
Output the scaled image
LowIn lower grey level in the input range
HighIn upper grey level for the input range
LowOut lower grey level for the output range
HighOut upper grey level for the output range
PhaseLow grey level, in the output image, for those pixels in the input
 which are darker than **LowIn**, (depends on **Mode**).
PhaseHigh grey level, in the output image, for those pixels in the input
 image which are brighter than **HighIn**, (depends on **Mode**).
Mode_? defines the treatment for the grey levels outside the range
LowIn-HighIn:

- = 1 grey levels outside **LowIn** and **HighIn** are not changed
- = 2 grey levels outside **LowIn** and **HighIn** are mapped to the values **LowOut** or **HighOut**, respectively.
- = 3 grey levels outside **LowIn** and **HighIn** are mapped to the grey levels **PhaseLow** and **PhaseHigh**

read (arg1, arg2, arg3,...)

Read is used to read in values interactively.

Parameters:

arg1, 2, represents constants, variables or expressions, with or without brackets.

thinbin (input, output, steps, mode, <I>invert, <I>endpoints)

Binary thinning, thins white linear structures in binary images (skeletonization). For every thinning step, pixels that are not relevant for the connectivity of an object are removed from the object margins, i.e., converted into background pixels. The connectivity of objects is thus maintained. This procedure can be continued until all objects are reduced to one-pixel-wide that approximate the skeletons. Convex objects are thinned to very short skeleton lines, or even to single pixels. Line ends generated in the thinning process are not essential for connectivity but are often necessary for the required skeleton. If **Endpoints** is switched on, pixels at those line ends are not removed by further thinning steps. **Steps** determines the number of thinning steps to be performed. Thinning stops automatically as soon as no more object pixels can be removed, regardless of the current value of **Steps**. If **Steps = 0**, thinning will be continued until the automatic stop is reached.

Parameters:

Input	image to be processed
Output	the thinned image
Steps	number of thinning steps
	= 0 terminates the execution automatically when all structures have been reduced to the width of one pixel
Mode_?	controls the effects of the function at the borders of the image:
	= 0 pixels outside the image borders are regarded as background (grey level 0), single pixels will be erased
	= 1 a one-pixel wide line of grey level 255 is inserted on the image borders, single pixels will be erased
	= 2 pixels outside the the image borders are regarded as objects (grey level = 255). Therefore structures touching the frame will be connected to this visual object, single pixels will be erased.
	= 3 skeleton for fibres

	= 4	same as Mode 0 , but: single pixels will be preserved
	= 5	same as Mode 1 , but: single pixels will be preserved
	= 6	same as Mode 2 , but: single pixels will be preserved
Invert <logical>	_ON	the image is inverted before processing
EndPoints <logical>	_ON	line ends are not shortened

while loop

This loop is used to repeat the commands in the loop as long as the condition is valid.

Syntax: ***while (condition)***
 .
 .
 endwhile

write (arg)

Write is used to output text and variables.

Parameters:

arg represents constants, variables or expressions, with or without brackets.

xorim (input1, input2, output)

Xorim (exclusive or) correlates every pixel that is either in image 1 or image 2 but not common to image 1 and image 2 and the result outputted to image 3. ***Input1*** and ***Input2*** are the two binary images to be correlated.

Program Running Procedures for the Du Model

MCPD is written in FORTRAN 77, compiled using the Microsoft FORTRAN compiler and executed with McFortran/020. The executable code is *MCPD.apl*. MCPD can be executed by clicking on *MCPD.apl*. The program loads the input files and displays the used input parameter integer numbers.

1. *nch*- If $nch=1$, MCPD deals with at least one boundary, if $nch =$ any other integer numbers, MCPD deals with no boundary.
2. *number*- is a boundary type integer. If $number = 1, 2, \text{ or } 3$, MCPD deals with rectangular, circular, or roller cutter boundary, respectively. If the boundary type is rectangular, the user needs to input 1.
3. *nb1*- is total boundary element number.
4. *nboun*- is the number of straight sides of a rectangle, for example, $nboun = 4$ for a rectangle or square.
5. *itpt*- *itpt* is a user controlled program iteration number. Iteration (*Itr*) starts from 1 and increases by 1 only after crack(s) grows (grow) by an incremental length. The program will stop when *Itr* reaches the user input number. For example, if $itpt = 5$, program will check whether there is a growing crack; if there is, the growing crack(s) will increase incrementally by one length, and the *Itr* increase by 1 until *Itr* reaches 5. If there is no growing crack(s) during iteration, *Itr* will keep its prior value and program will either load to check the growing crack(s) again, or terminate running the program.
6. *E*- is user input Young's modulus.
7. *gcc*- is user input critical fracture toughness.
8. *pxx, pyy, pxy*- are user input far field x-direction normal stress, y-direction normal stress, and shear stress, respectively.

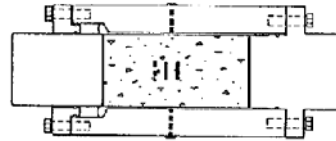
9. *delpxx*, *delpyy*, *delpxy*- are user input far field x-direction incremental normal stress, y-direction normal stress, and shear stress, respectively.
10. *delbxx*, *delbyy*, *delbxy*- are user input boundary x-direction incremental normal stress, y-direction incremental normal stress, and incremental shear stress, respectively.
11. *rdl*- is the ratio of the incremental length of a growing crack to the length of a crack tip element.
12. *numos*- If *numos* = 0, program does not calculate the stress, strain, and displacement within the body; if *numos* = any other number, it does.
13. *ncboun*-If *ncboun* = 0, program does not calculate the stress, strain, and displacement on the boundary; if *ncboun* = any other number, it does.

The propagation of multiple cracks can be illustrated by a graphic executable code- *graphic.apl*, and the user only needs to input the total boundary element number after double clicking on *graphic.apl*.

APPENDIX C: TEST CELL DESIGN

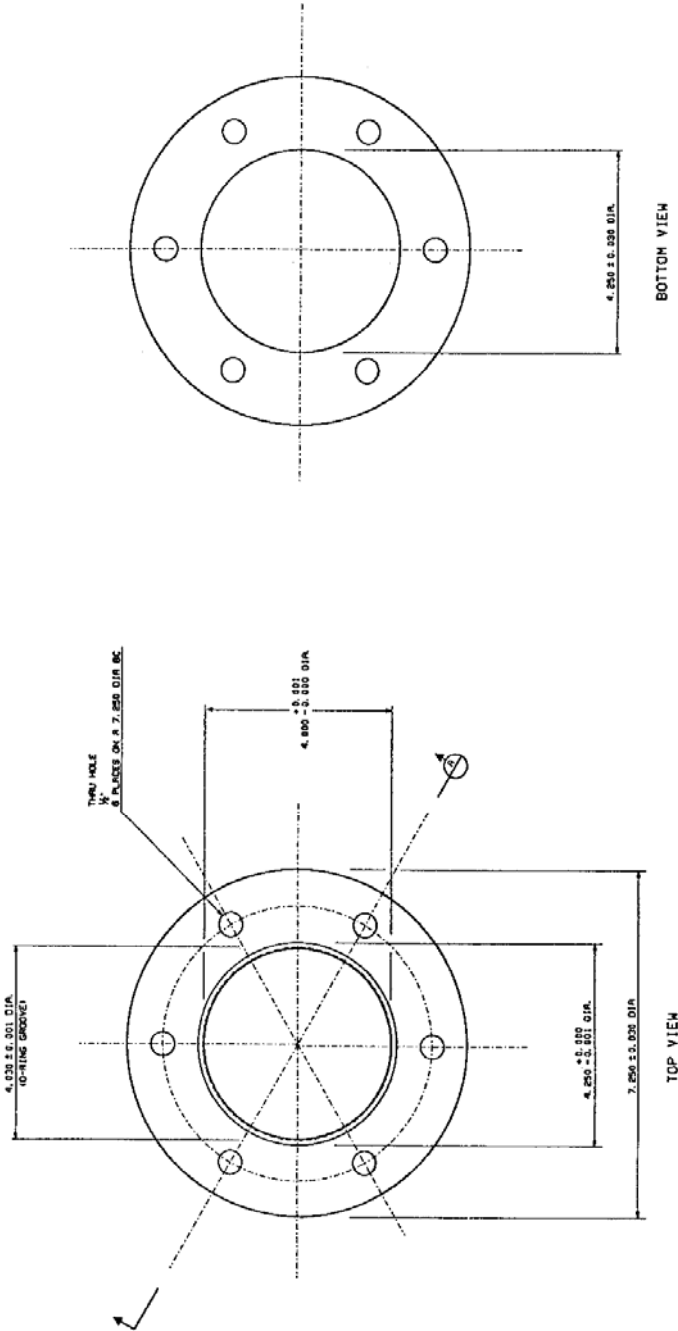
UNIVERSITY OF CALIFORNIA, BERKELEY

INJECTION TEST APPARATUS DESIGN FOR MOLTEN METAL ALLOY PENETRATION IN CONCRETE SPECIMENS

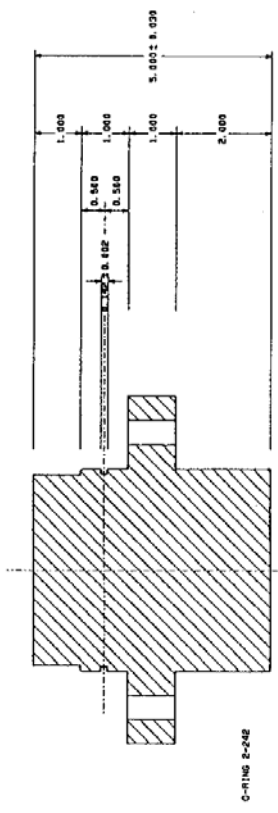


COLLEGE OF ENGINEERING
DEPARTMENTS OF CIVIL & MINING ENGINEERING
KAMRAN M. NEMATI
PROF. PAULLO J. MONTORO
PROF. NEVILLE G. W. COOK
DR. LARRY AYERS

FEBRUARY, 1990

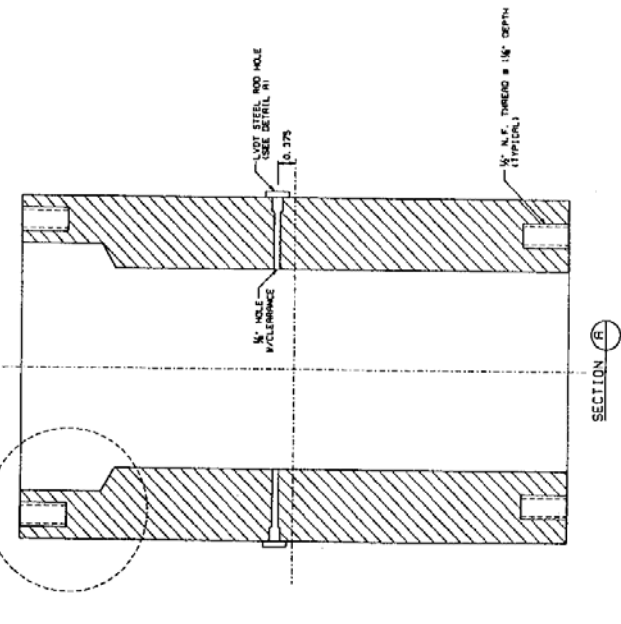
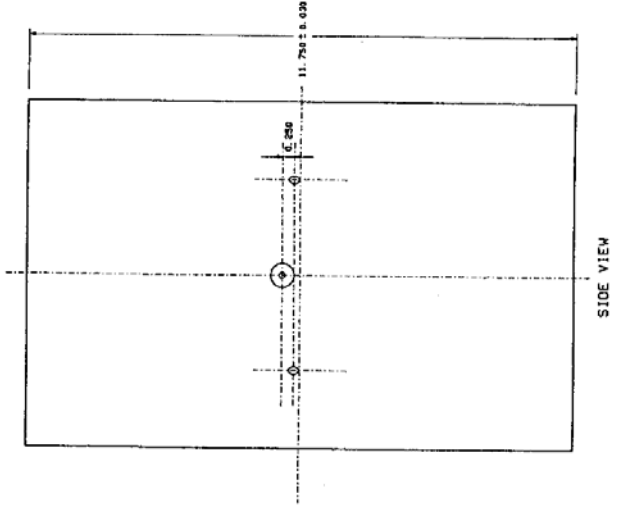
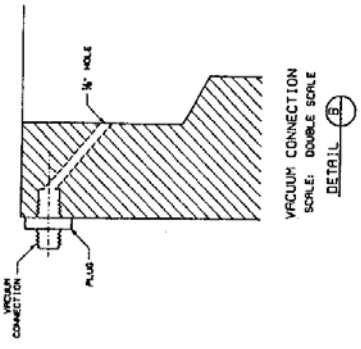
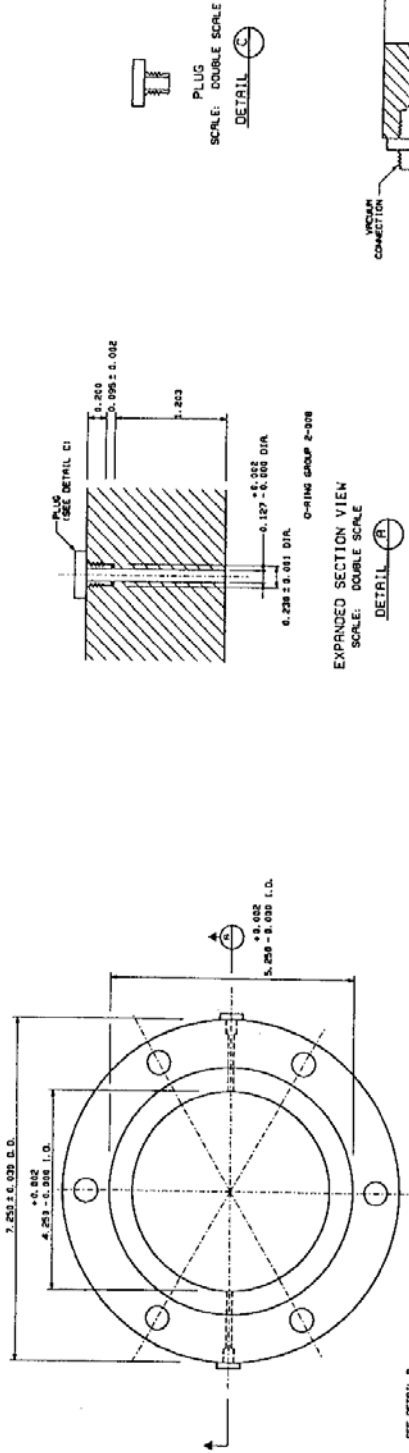


PEDESTAL
 MATERIAL: GRAPHITIZED STEEL
 SCALE: FULL SCALE
 QUANTITY: 1



DATE	BY	REV.	DESCRIPTION
1970	W. J. WILSON	1	DESIGN
1970	W. J. WILSON	2	REVISED
1970	W. J. WILSON	3	REVISED
1970	W. J. WILSON	4	REVISED
1970	W. J. WILSON	5	REVISED
1970	W. J. WILSON	6	REVISED
1970	W. J. WILSON	7	REVISED
1970	W. J. WILSON	8	REVISED
1970	W. J. WILSON	9	REVISED
1970	W. J. WILSON	10	REVISED
1970	W. J. WILSON	11	REVISED
1970	W. J. WILSON	12	REVISED
1970	W. J. WILSON	13	REVISED
1970	W. J. WILSON	14	REVISED
1970	W. J. WILSON	15	REVISED
1970	W. J. WILSON	16	REVISED
1970	W. J. WILSON	17	REVISED
1970	W. J. WILSON	18	REVISED
1970	W. J. WILSON	19	REVISED
1970	W. J. WILSON	20	REVISED
1970	W. J. WILSON	21	REVISED
1970	W. J. WILSON	22	REVISED
1970	W. J. WILSON	23	REVISED
1970	W. J. WILSON	24	REVISED
1970	W. J. WILSON	25	REVISED
1970	W. J. WILSON	26	REVISED
1970	W. J. WILSON	27	REVISED
1970	W. J. WILSON	28	REVISED
1970	W. J. WILSON	29	REVISED
1970	W. J. WILSON	30	REVISED
1970	W. J. WILSON	31	REVISED
1970	W. J. WILSON	32	REVISED
1970	W. J. WILSON	33	REVISED
1970	W. J. WILSON	34	REVISED
1970	W. J. WILSON	35	REVISED
1970	W. J. WILSON	36	REVISED
1970	W. J. WILSON	37	REVISED
1970	W. J. WILSON	38	REVISED
1970	W. J. WILSON	39	REVISED
1970	W. J. WILSON	40	REVISED
1970	W. J. WILSON	41	REVISED
1970	W. J. WILSON	42	REVISED
1970	W. J. WILSON	43	REVISED
1970	W. J. WILSON	44	REVISED
1970	W. J. WILSON	45	REVISED
1970	W. J. WILSON	46	REVISED
1970	W. J. WILSON	47	REVISED
1970	W. J. WILSON	48	REVISED
1970	W. J. WILSON	49	REVISED
1970	W. J. WILSON	50	REVISED
1970	W. J. WILSON	51	REVISED
1970	W. J. WILSON	52	REVISED
1970	W. J. WILSON	53	REVISED
1970	W. J. WILSON	54	REVISED
1970	W. J. WILSON	55	REVISED
1970	W. J. WILSON	56	REVISED
1970	W. J. WILSON	57	REVISED
1970	W. J. WILSON	58	REVISED
1970	W. J. WILSON	59	REVISED
1970	W. J. WILSON	60	REVISED
1970	W. J. WILSON	61	REVISED
1970	W. J. WILSON	62	REVISED
1970	W. J. WILSON	63	REVISED
1970	W. J. WILSON	64	REVISED
1970	W. J. WILSON	65	REVISED
1970	W. J. WILSON	66	REVISED
1970	W. J. WILSON	67	REVISED
1970	W. J. WILSON	68	REVISED
1970	W. J. WILSON	69	REVISED
1970	W. J. WILSON	70	REVISED
1970	W. J. WILSON	71	REVISED
1970	W. J. WILSON	72	REVISED
1970	W. J. WILSON	73	REVISED
1970	W. J. WILSON	74	REVISED
1970	W. J. WILSON	75	REVISED
1970	W. J. WILSON	76	REVISED
1970	W. J. WILSON	77	REVISED
1970	W. J. WILSON	78	REVISED
1970	W. J. WILSON	79	REVISED
1970	W. J. WILSON	80	REVISED
1970	W. J. WILSON	81	REVISED
1970	W. J. WILSON	82	REVISED
1970	W. J. WILSON	83	REVISED
1970	W. J. WILSON	84	REVISED
1970	W. J. WILSON	85	REVISED
1970	W. J. WILSON	86	REVISED
1970	W. J. WILSON	87	REVISED
1970	W. J. WILSON	88	REVISED
1970	W. J. WILSON	89	REVISED
1970	W. J. WILSON	90	REVISED
1970	W. J. WILSON	91	REVISED
1970	W. J. WILSON	92	REVISED
1970	W. J. WILSON	93	REVISED
1970	W. J. WILSON	94	REVISED
1970	W. J. WILSON	95	REVISED
1970	W. J. WILSON	96	REVISED
1970	W. J. WILSON	97	REVISED
1970	W. J. WILSON	98	REVISED
1970	W. J. WILSON	99	REVISED
1970	W. J. WILSON	100	REVISED

UNIVERSITY OF CALIFORNIA, BERKELEY			
INJECTION TEST APPARATUS DESIGN FOR			
MOLTEN METAL ALLOY PENETRATION			
IN CONCRETE SPECIMENS			
COURSE NO.	CE 279	DATE	NOV. 2, 1970
SECTION	2	OF	2
SCALE	AS SHOWN	BY	W. J. WILSON
PROJECT	SPRING SEMESTER, 1970	GROUP NO.	2
DATE	NOV. 2, 1970	BY	W. J. WILSON



VESSEL
MATERIAL: HIGH STRENGTH
SCALE: FULL SCALE
QUANTITY: 1

SCALE (INCHES): 1" = 1"

UNIVERSITY OF CALIFORNIA, BERKELEY
PROJECT: INJECTION TEST APPARATUS DESIGN FOR
ROLLING MILL FLOOR REPAIR
IN CONCRETE SPECIMENS
DATE: 10/15/68
DRAWN BY: J. J. COOK
CHECKED BY: J. J. COOK
SCALE: 1" = 1"
COURSE NO. CE 299
DATE: 10/15/68
FIG. NO. 1
PAGE NO. 4
TOTAL PAGES 4

